

AD-A164 061

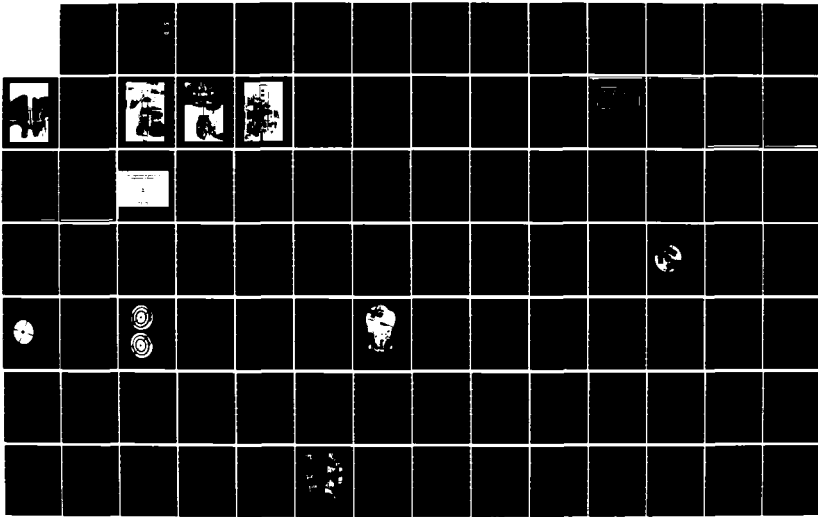
DEVELOPMENT OF A SENSITIVE SUPERCONDUCTING  
ACCELEROMETER AND GRAVITY GRADIOMETER(U) STANFORD UNIV  
CA DEPT OF PHYSICS W M FAIRBANK ET AL. SEP 84  
AFOSR-TR-85-1126 AFOSR-80-0067

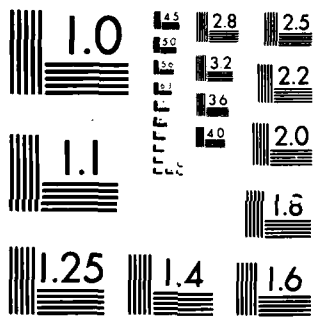
1/2

UNCLASSIFIED

F/G 8/5

NL





MICROCOPY RESOLUTION TEST CHART  
NATIONAL BUREAU OF STANDARDS 1963-A

AD-A164061

2

UNCLASSIFIED

SECURITY CLASSIFICATION OF THIS PAGE

REPORT DOCUMENTATION PAGE

AD-A164 061

1a. REPORT SECURITY CLASSIFICATION UNCLASSIFIED		1b. RESTRICTIVE MARKINGS	
2a. SECURITY CLASSIFICATION AUTHORITY DECLASSIFICATION/DOWNGRADING SCHEDULE		3. DISTRIBUTION/AVAILABILITY OF REPORT APPROVED FOR PUBLIC RELEASE; DISTRIBUTION UNLIMITED	
PERFORMING ORGANIZATION REPORT NUMBER(S)		5. MONITORING ORGANIZATION REPORT NUMBER(S) AFOSR-TR-85-1126	
1. NAME OF PERFORMING ORGANIZATION Dept. of Physics	5b. OFFICE SYMBOL (If applicable)	7a. NAME OF MONITORING ORGANIZATION Air Force Office of Scientific Research	
c. ADDRESS (City, State and ZIP Code) Stanford University Stanford, CA 94305		7b. ADDRESS (City, State and ZIP Code) Building 410 Bolling AFB, DC 20332-6448	
3a. NAME OF FUNDING/SPONSORING ORGANIZATION AFOSR	5b. OFFICE SYMBOL (If applicable) NP	9. PROCUREMENT INSTRUMENT IDENTIFICATION NUMBER AFOSR-80-0067	
8c. ADDRESS (City, State and ZIP Code) Building 410 Bolling AFB, DC 20332		10. SOURCE OF FUNDING NOS.	
		PROGRAM ELEMENT NO. 61102F	PROJECT NO. 2309
		TASK NO. A1	
11. TITLE (Include Security Classification) Development of a Sensitive Superconducting Accelerometer and Gravity Gradiometer			
12. PERSONAL AUTHOR(S) William M. Fairbank, Daniel DeBra			
13a. TYPE OF REPORT FINAL	13b. TIME COVERED FROM Oct 79 TO 30 Sep 84	14. DATE OF REPORT (Yr. Mo., Day) 84 Sep 84	15. PAGE COUNT 120
16. SUPPLEMENTARY NOTATION			
17. COSATI CODES		18. SUBJECT TERMS (Continue on reverse if necessary and identify by block number)	
FIELD	GROUP	SUB. GR.	
19. ABSTRACT (Continue on reverse if necessary and identify by block number) The inverse square law of gravitation is known to agree with astronomical data to very high accuracy, but recent theoretical and experimental work indicate that the inverse square law may be violated at distances less than 1000 km. Such a violation would signal the existence of a new force. In order to check the inverse square law we are preparing to search for a non-newtonian force in a cylindrical shell. The cylindrical shell has the property that the newtonian effects nearly cancel, so that we are doing a nearly null experiment. We have developed a superconducting gradiometer to measure the gravitational force gradients at the center of this cylindrical shell. By measuring both the vertical and horizontal gradients we can eliminate effects due to imperfections in the cylinder. This report describes the instrument and its performance as well as calculations of the sensitivity of the inverse square law test.			
20. DISTRIBUTION/AVAILABILITY OF ABSTRACT UNCLASSIFIED/UNLIMITED <input checked="" type="checkbox"/> SAME AS RPT. <input type="checkbox"/> DTIC USERS <input type="checkbox"/>		21. ABSTRACT SECURITY CLASSIFICATION	
22a. NAME OF RESPONSIBLE INDIVIDUAL HUGO WEICHEL, Col. USAF		22b. TELEPHONE NUMBER (Include Area Code) (202) 767-4904	22c. OFFICE SYMBOL NP

DTIC ELECTRIC FEB 2 1986

DTIC FILE COPY

AFCO 1000



Department of Physics  
Stanford University  
Stanford, CA 94305

FINAL SCIENTIFIC REPORT  
to the  
AIR FORCE OFFICE OF SCIENTIFIC RESEARCH  
for  
DEVELOPMENT OF A SENSITIVE SUPERCONDUCTING ACCELEROMETER  
AND GRAVITY GRADIOMETER

Air Force Contract # AFOSR 80-0067  
For the Period 1 October 1979 - 30 September 1984

Co-Principal Investigators:

William M. Fairbank  
Professor of Physics

and

Daniel DeBra  
Professor of Aeronautics  
& Astronautics

Accession For	
NTIS CRA&I	<input checked="" type="checkbox"/>
DTIC TAB	<input type="checkbox"/>
Unannounced	<input type="checkbox"/>
Justification	
By	
Distribution/	
Availability Codes	
Dist	Avail and/or Special
A-1	

During this report period, the following people have been involved in the experiment:

William Fairbank - Co-Principal Investigator

Daniel DeBra - Co-Principal Investigator

Michael McAshan - Senior Research Associate

Evan Mapoles - Graduate Student and then Research Associate. His Ph.D. thesis entitled "Development of a Superconducting Gravity Gradiometer for Test of the Inverse Square Law," is included as Appendix 1. His publication, "A Superconducting Gravity Gradiometer" is included as Appendix 2.

#### RESEARCH OBJECTIVES

This research has had two objectives: (1) to study the application of cryogenic technology to the problem of gravity gradient measurements, and (2) to use such a gradiometer to make more accurate measurements of the inverse square law of gravity to test the recent experimental and theoretical suggestions that the inverse square law of gravity might be violated at laboratory distances.

Since room temperature gradiometers are ultimately limited by room temperature Brownian motion, we have been experimenting with a laboratory cryogenic gradiometer which could lead to the development of a more sensitive moving baseline gradiometer for field use. Such gradiometers could have applications to problems in navigation and modeling of the earth's gravitational field.

Recently the inverse square law of gravity at laboratory distances has become a subject of great interest to physicists. This has come about for two reasons. First, Long<sup>(1)</sup> and more recently, Tuck<sup>(2)</sup> have found an apparent violation to the inverse square law of gravity at laboratory distances. If this were

found to be correct, it would be one of the most important experiments in the history of physics. Secondly, theorists have begun to speculate on the possible existence of new fundamental particles which could affect the inverse square law of gravity at laboratory distances. For example, axions with mass  $10^{-5}$  eV have been postulated to explain the dark matter of our galaxy and the reason for the lack of parity in time-reversal violation and strong interactions. Such particles could contribute to a violation of the inverse square law.<sup>(3)</sup> By making use of a superconducting gradiometer it appears possible to check the inverse square law at distances of the order of one meter to an accuracy of 2 parts in  $10^5$ .

Operation of a gravity gradiometer at 4 K offers a reduction of thermal noise power by a factor of 75 over that in room temperature environments, and this is the principle motivation for the development of cryogenic instruments. However, there are many other potential advantages which help to offset the additional effort required to maintain the instrument at 4 K. Below 10 K several metals lose all low frequency electrical resistance (superconductivity) and become nearly perfect magnetic shields. These materials are used in our gravity gradiometers to make magnetic readouts which are free of thermal noise. Although careful construction is required to allow for the thermal contraction of the instrument as it is cooled from room temperature to 4K, once the device is cold the coefficient of thermal expansion is far below the room temperature value. The liquid helium bath commonly used to maintain low temperature also provides a stable thermal environment. In addition, low frequency amplifiers of unequaled sensitivity based on the Josephson effect (SQUIDs) are commercially available.

## SUMMARY OF RESEARCH EFFORT

During the early part of our work we constructed and tested two prototype gradiometers. These devices both incorporated superconducting coils and proof masses, were built with similar techniques, and both measured a single diagonal component of the gravity gradient tensor. They differed in the method used to obtain common mode balancing. One of our prototypes used four superconducting coils, one on each side of two superconducting diaphragms. Each pair of coils and diaphragm produced a current in response to an applied acceleration, and these two currents were subtracted at the input of a SQUID. We referred to this gradiometer as "current differencing". Our second prototype used a single coil located between two superconducting proof masses so that its inductance was modulated only by relative motion of these two proof masses. We called this gradiometer "displacement differencing". Because the four coils in the current differencing gradiometers are not perfectly matched, the overall balancing problem in this gradiometer is more complicated. Consequently, we choose the displacement differencing design to an improved version.

We have completed construction of this improved gradiometer and operated it at 4.2 K with sensitivity approaching  $1\text{E}/\sqrt{\text{Hz}}$  at frequencies between 2 and 10 Hz. The operation of this gradiometer is described in Appendices 1 and 2. In order to achieve this level of sensitivity at lower frequencies, a new cryostat probe was built to provide a 1.3 K environment for the gradiometer. The purpose of this was to reduce the thermal sensitivity of the instrument. In addition, the new probe was designed to provide a high degree of seismic and magnetic isolation. This probe is being used to gather data from the gradiometer in the inverse square law experiment.

## DESCRIPTION OF THE GRADIOMETER

Our primary goal in the design and fabrication of our gravity gradiometer was to minimize the instrument's sensitivity to linear accelerations both along the proof mass direction and perpendicular to it. Linear accelerations in the laboratory exert forces on the proof masses which are very large compared to the gravitational forces we would like to measure, so careful balancing of the gradiometer is needed to eliminate them as a noise source,

In addition, we decided to build an on-line gradiometer which measures one of the diagonal components of  $\Gamma$ . It is highly desirable to be able to measure all three components of  $\nabla^2\phi$  so we chose a method for suspending the proof masses which allows us to operate the gradiometer with its sensitive axis vertical as well as horizontal.

In order to make the balancing problem manageable we chose a mechanical design which enabled us to use only one coil in the readout system described later. Experiments have been done with readouts using several coils, but in these gradiometers careful matching of the coils as well as the proof masses is necessary to reject linear accelerations.

Basically the gradiometer consists of two superconducting proof masses adjacent to each other. A single niobium coil is mounted in the gap between the proof masses so that the coil inductance is proportional to their spacing. This readout system is analyzed in detail below. Since the sensitive axes of the proof masses are parallel, the gradiometer detects changes in one of the diagonal components of the gravity gradient tensor,  $\Gamma_{jj}$ .

Each of the two proof masses is supported with two mechanical springs. The mechanical springs are folded cantilevers cut into circular disks of niobium. A folded cantilever with two-fold symmetry is shown in figure 1.



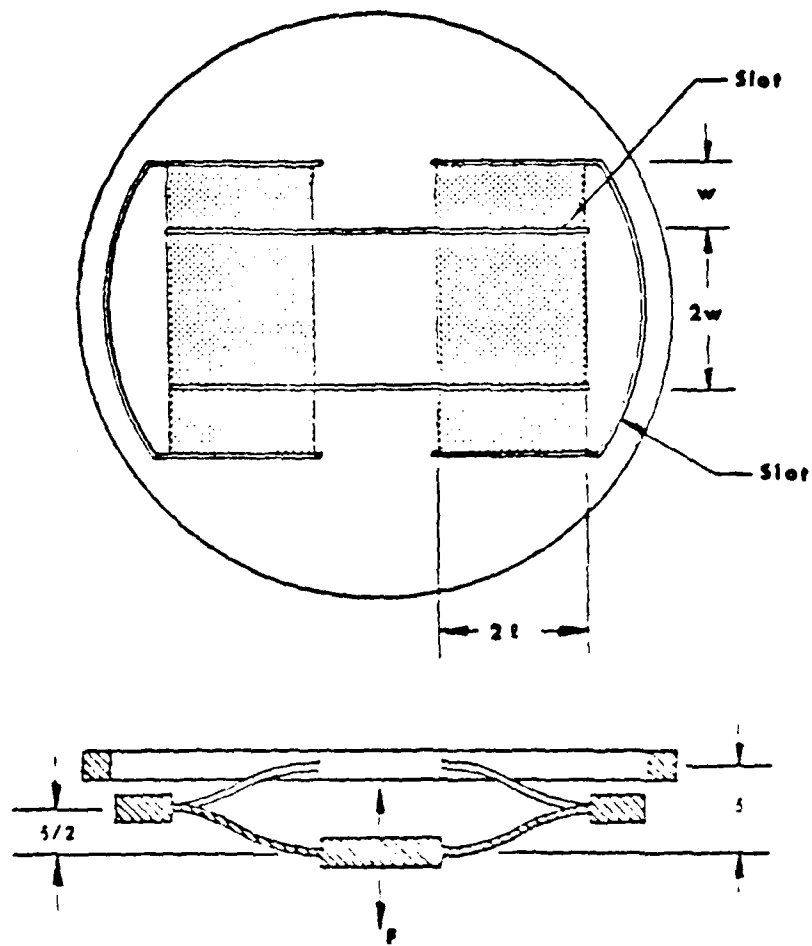


Figure 1. Folded Cantilever Spring

In this case the thickness of the plate is reduced in the two rectangular areas hatched in the figure in order to restrict the bending to those areas. Slots are then cut in the indicated locations. These slots allow the center to move perpendicular to the plane of the plates as shown in the lower part of the figure. Since the center of the spring is free to move in the plane of the plate, the total length of the spring remains constant and the restoring force is provided by pure bending without stretching of the spring material.

The proof mass subassembly consists of two springs, two cover pieces, an annular mass, and a ring used to hold the edges of the springs apart. The cover pieces are circular disks of niobium 8.51 cm in diameter which are flat on one side and have a threaded stud on the opposite side. The flat sides are designed to modulate the inductance of the readout coil or tuning coils described later. The flats were polished to ensure flatness and isotropy so that close spacing to the coils could be obtained, and so that the inductance of the coils is modulated only by linear motion of the surfaces. The threaded studs screw into an annular disk of niobium which provides the bulk of the mass for each proof mass. A spring is captured between each cover piece and proof mass. An exploded view of one of the two proof mass subassemblies is shown in Figure 2. The ring which is used to maintain the spacing of the edges of the springs is thicker than the proof mass so that each spring is biased away from its equilibrium position and never passes through its zero point. This eliminates certain forms of nonlinear behavior. Since the springs have opposite biases, the first order nonlinear terms also cancel. The ring was grounded to its final thickness to keep its two sides parallel to one part in  $10^5$ .

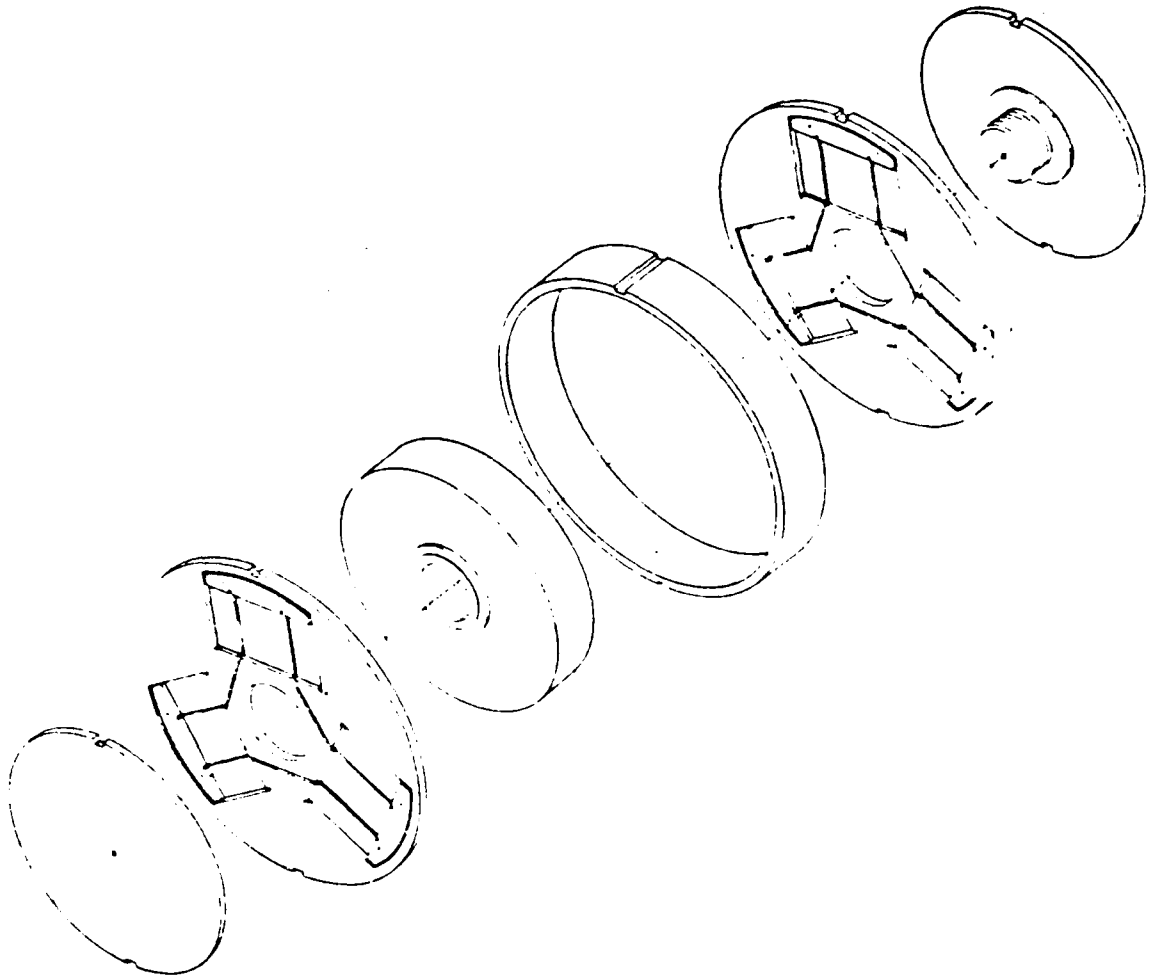


Figure 2. Exploded View of a Proof Mass Subassembly

Once the two proof mass subassemblies were constructed, they were stacked on top of each other with a ring holding them apart. The thickness of the ring was chosen so that the readout coil is about 0.013 cm from the opposite proof mass. This structure was mounted on an aluminum fixture which maintained the angular orientation of the parts. A niobium housing tube 9.3 cm long with a 10.5 cm inside diameter was placed over the parts (Figure 3). A more detailed description of this gradiometer is given in Appendix 1, including details of experimental measurements on the gradiometer.

The assembled gradiometer was first tested at 4.2 K and has performed as expected in the frequency range from 2 Hz to 10 Hz (see Appendix 1). It has since been incorporated in a new cryostat probe capable of cooling the instrument to 1.3 K and is being used on the inverse square law experiment.

#### INVERSE SQUARE LAW EXPERIMENT

The theory and background for this experiment is given in Chapters 4 and 5 of Appendix 1. We have completed construction of all major components of the inverse square law experiment (Figure 4) and have commenced work on the experiment. These components include a 1.3 K cryogenic probe and a pedestal which is used to mount the cryostat in a ten foot hole in the floor. A pumping line is incorporated into the pedestal which allows us to continuously pump on the cryostat to maintain the temperature of the gradiometer at 1.3 K while the cylindrical source is moved up and down over the cryostats. The final major piece of the apparatus is the system for moving the cylinder up and down.

## FIGURE CAPTIONS

- Figure 3 Assembled gradiometer in mounting fixture. Mounting fixture includes flex hinges on both sides of the gradiometer so that the instrument may be tilted slightly by PZT bender plates (upper center).
- Figure 4 Major components of the inverse square law experiment. The cylindrical test mass is shown in the upper and central portion of the picture and the dewar on its pedestal is barely visible at the bottom.
- Figure 5 Upper and mid-portion of the new cryostat probe. Cold plate and the upper part of the 1.3 K radiation shield are at the very bottom. The isolation stack (which would be at the very top) is not included at this level of assembly.
- Figure 6 Lower detail of the 1.3 K cryostat probe including the gradiometer and its fixture in the lower portion of the picture. The plate in the central portion is a 1.3 K continuous cold plate refrigerator. During operation the gradiometer is completely enclosed by copper radiation shield attached to the cold plate. In turn the entire lower portion of the probe is isolated from the 4 K helium bath by a vacuum can sealed onto the top plate seen in the upper part of the picture.
- Figure 7 Mechanical isolation stack. This assembly sits on top of the cryostat and provides the sole mechanical support for the gradiometer. During operation, the stack is enclosed in a vacuum can.

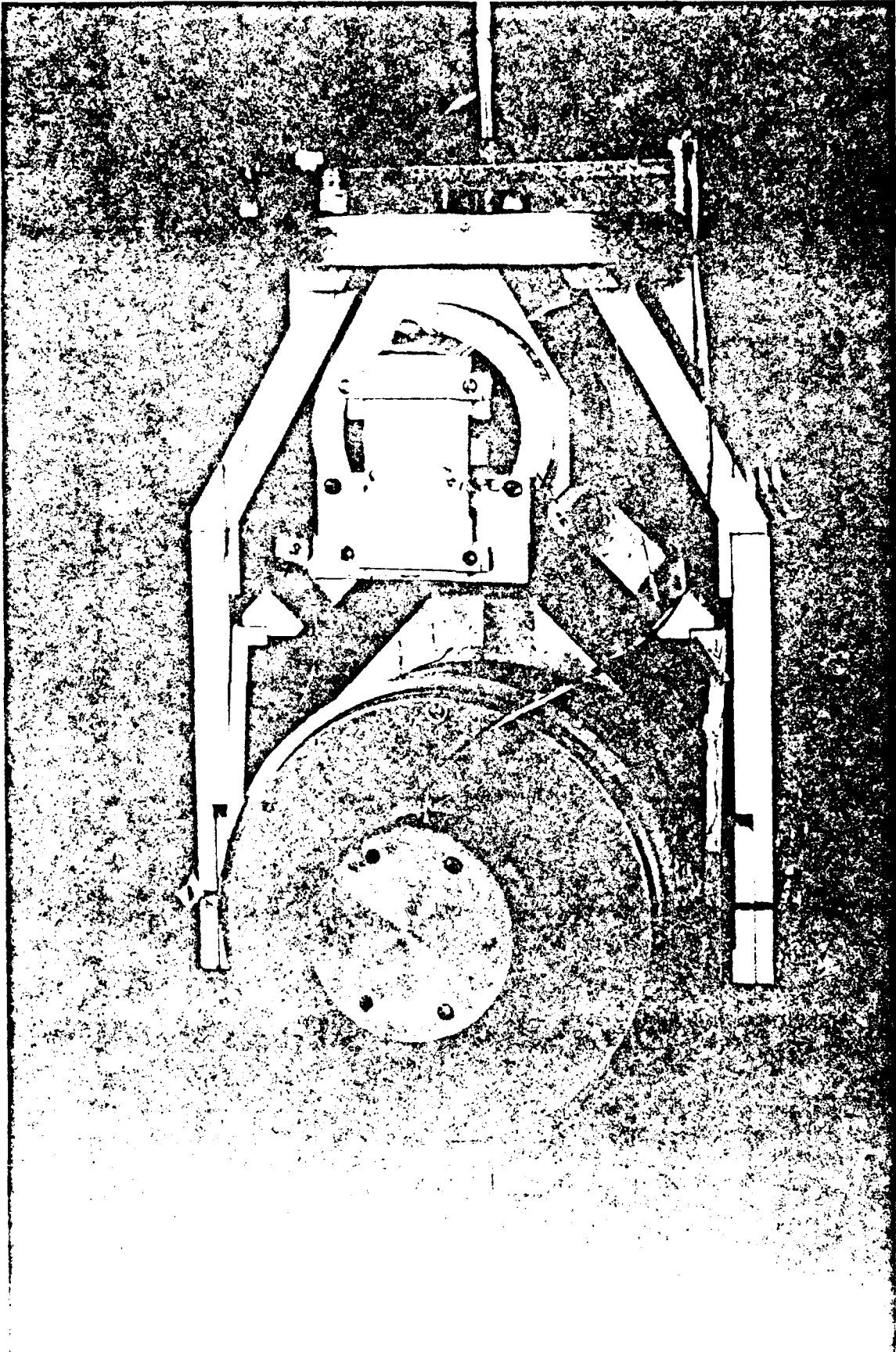


Figure 3

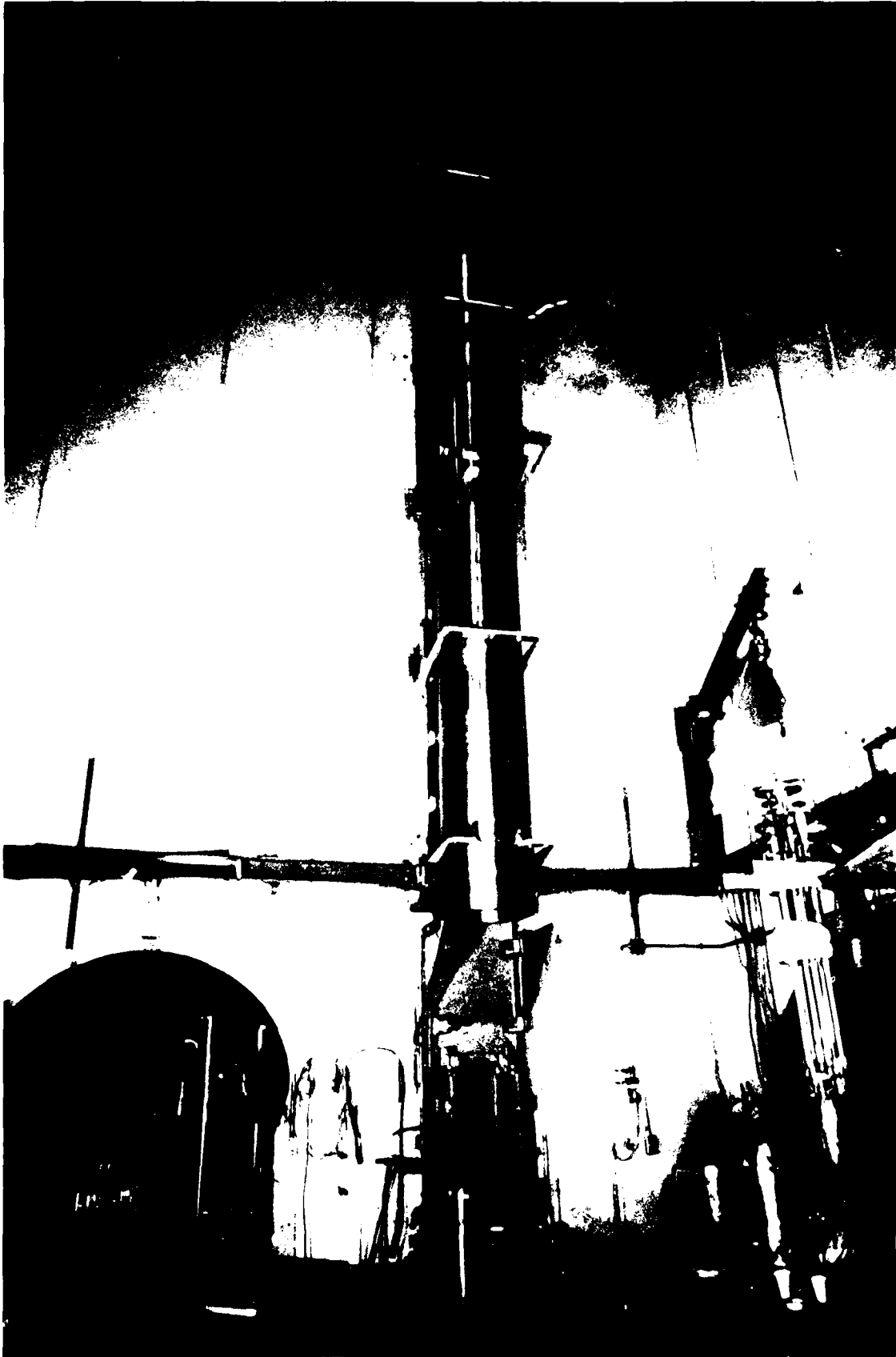


Figure 4

In order to maintain the gradiometer at 1.3 K, the new probe has a copper plate inside of the vacuum can which serves as a refrigerator (Figure 5). The probe vacuum can is immersed in a liquid helium bath at 4.2 K. The copper plate inside the can is thermally isolated from the can and contains a small reservoir which is connected to the 4.2 K bath through a flow impedance (Figure 6). This reservoir is continuously pumped to maintain the plate at 1.3 K. The flow impedance is adjusted at room temperature to adjust the temperature of the plate. The gradiometer is thermally grounded to this plate to operate it at 1.3 K. The cold plate has been tested successfully. It has the major advantage that liquid helium can be added to the bath in the usual way without disturbing the 1.3 K space. This means that the 1.3 K space can be maintained for long periods.

A second major improvement in the new probe is the addition of a mechanical transmission line which will isolate the gradiometer from vibrations at frequencies above 10 Hz (Figure 7). This line consists of four brass disks which hang from each other with small latex springs. The soft springs cut off vibrations above a frequency of about 10 Hz. The gradiometer hangs from the bottom of this stack by a stainless steel tube which allows the gradiometer to be at 1.3 K while the stack is at room temperature. The entire assembly is in vacuum to isolate from acoustic noise.

In order to measure the gradient at the center of the cylindrical gravitational source, the dewar containing the probe and the gradiometer has been mounted on a pedestal which will fit inside of the cylinder. The pedestal is mounted at the bottom of a ten foot deep hole which the cylinder is lowered into during the measurement. This leaves the dewar near floor level to facilitate adjustments. A pumping line is built in so that the cold plate can be pumped continuously as the cylinder goes up and down. The 7,160 pound cylinder rolls along



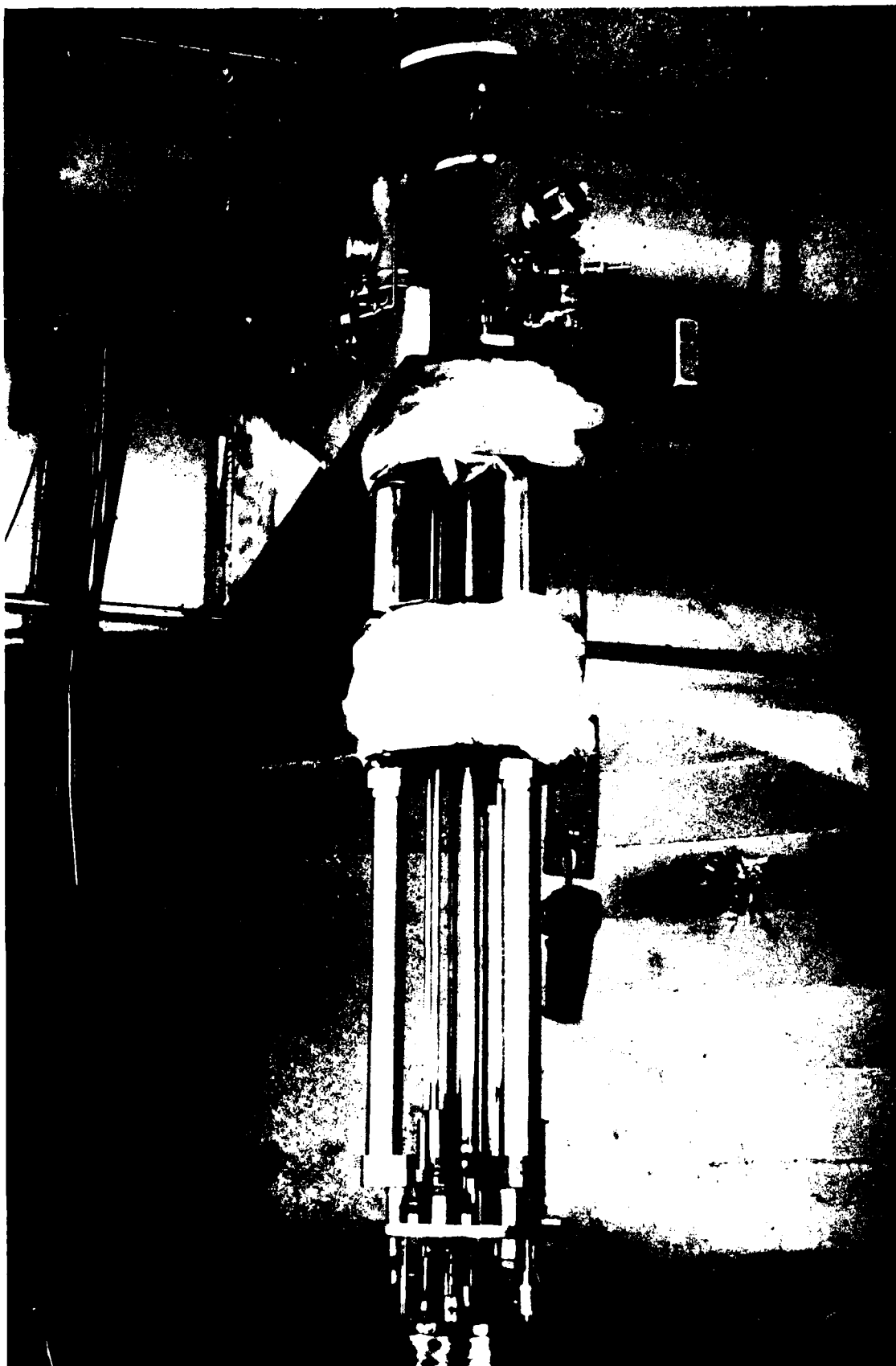


Figure 5

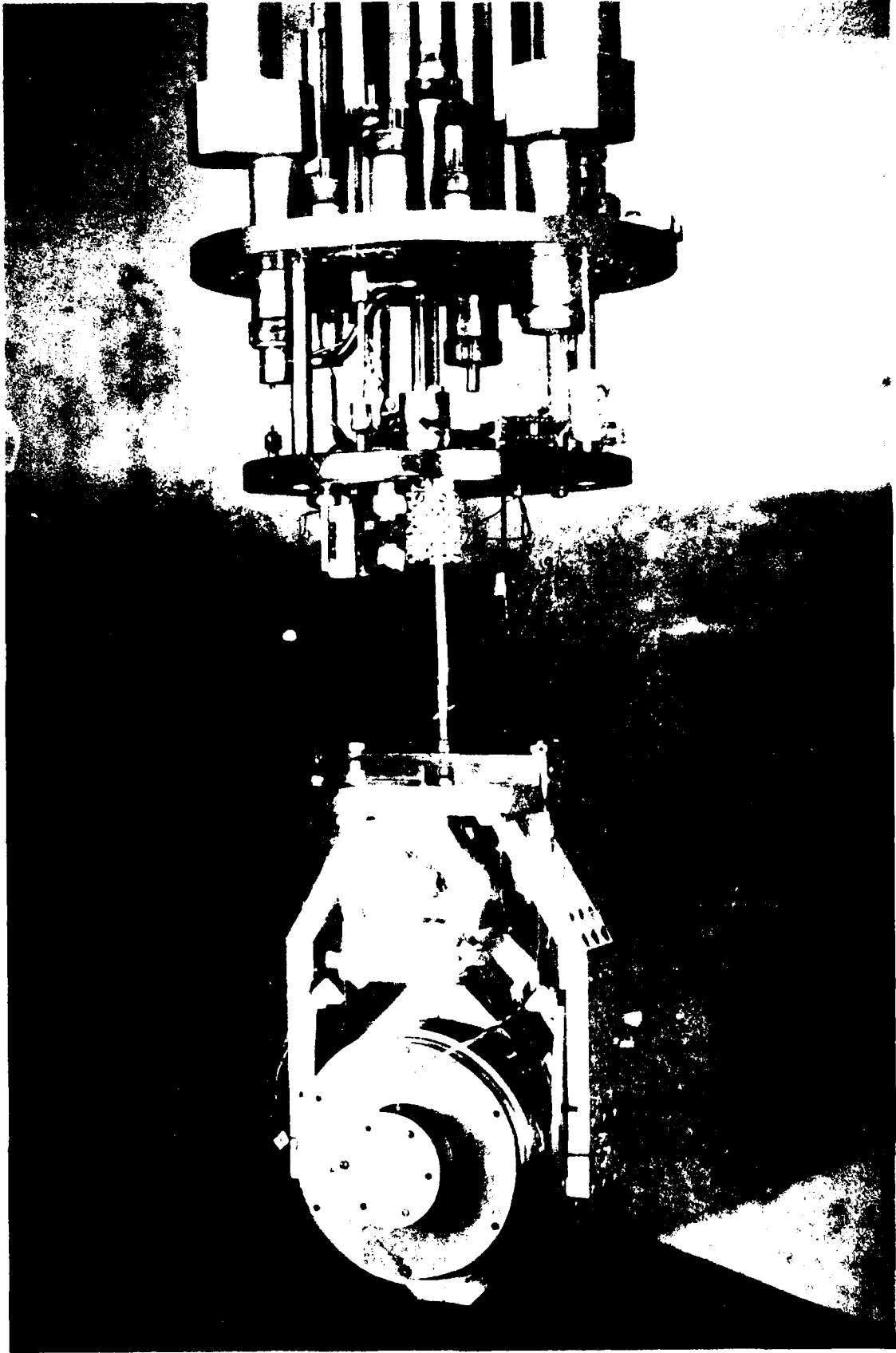


Figure 6  
13

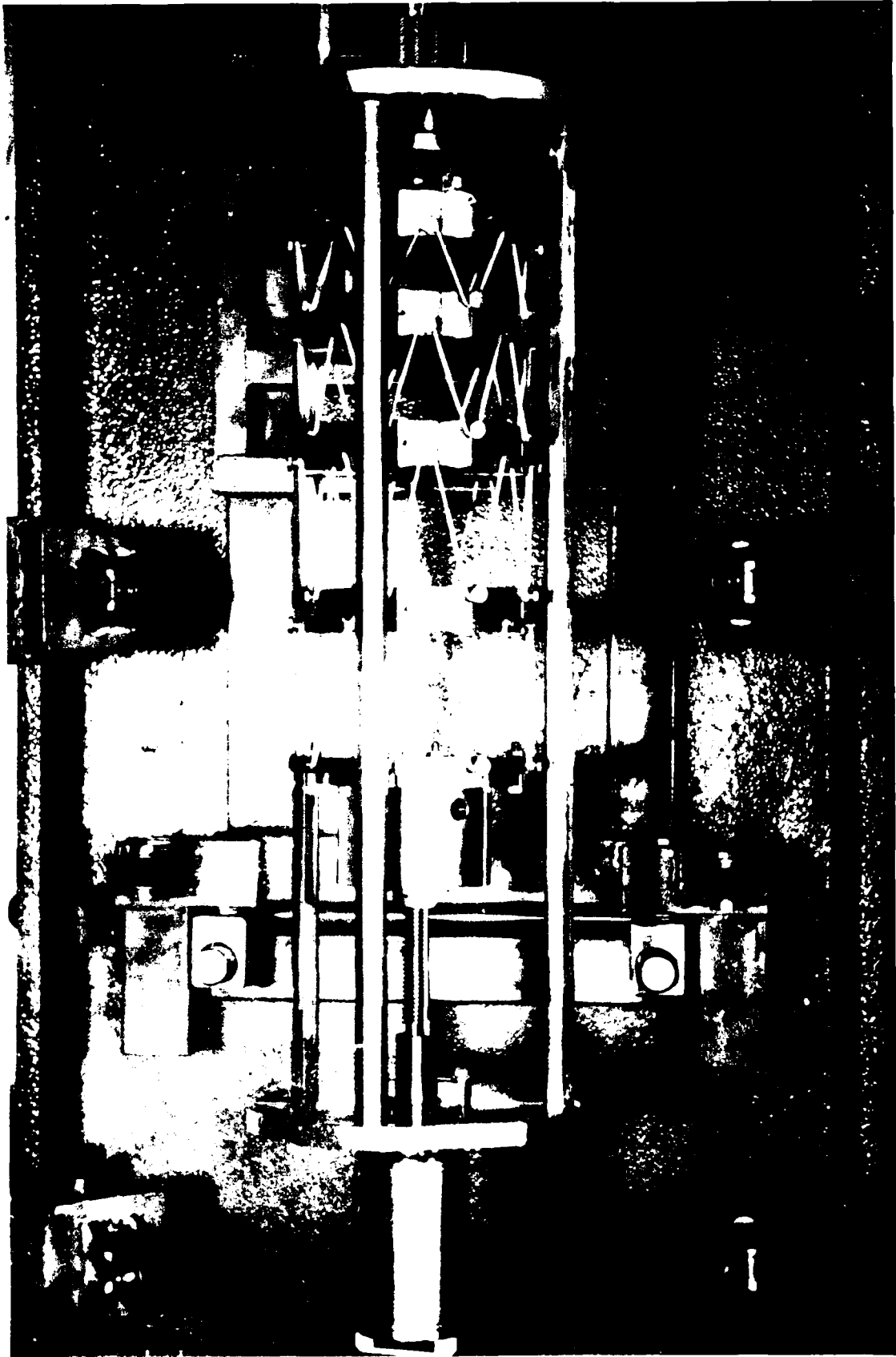


Figure 7

to steel I-beam up and down the wall of the end station in which the experiment takes place. A hoist has been installed to raise and lower it. Considerable care has been taken to ensure smooth motion of this large mass, and to minimize the vibration which the gradiometer must tolerate during the experiment.

During the past year the completed gradiometer and 1.3 K cryostat assembly has been subjected to initial tests. During these tests gradiometer output power spectra were obtained with the gradiometer in unbalanced operation. (Balanced operation was not possible due to inability to store sufficient current in the balancing circuit. This problem is presumed to be due to ohmic heating in the current supply leads which have been subsequently improved.) The output power spectrum obtained at 1.3 K was observed to have two distinct regions. Above about 0.2 Hz the spectrum was dominated by externally driven mechanical motion of the gradiometer, most notably the pendulum modes of the suspension system. Previous experience with the gradiometer has indicated that this response is reduced by a factor of  $\sim 1000$  when the gradiometer is properly balanced. Below  $\sim 0.1$  Hz the power spectrum was dominated by low-frequency-divergent behavior arising from the temperature coefficient of the gradiometer together with temperature fluctuations of the device. In the frequency range of interest for the inverse square law experiment ( $\sim 0.15$  Hz) the noise power is estimated to  $30-40 E/\sqrt{\text{Hz}}$  where a calibration factor obtained from operation at 4 K is used. Proper balancing of the gradiometer should drop this to a SQUID noise limited value of  $1 E/\sqrt{\text{Hz}}$ . Further reduction of this value by an order of magnitude seems possible by the use of a dc SQUID which is now commercially available.

Although the maximum frequency at which temperature fluctuations dominate the noise power spectrum has been shifted downward from 1 Hz at 4 K to 0.1 Hz at 1.3 K, the temperature coefficient at the lower temperature is higher than expected. In addition, temperature fluctuations at the gradiometer are on the order of 10 mK, much larger than what is possible to obtain. We have tentatively identified a free-floating radiation baffle located on the gradiometer suspension rod between the cold plate and the top of the vacuum can as a possible source of this problem. We are in the process of mounting a heater and thermometer on this baffle in order to be able to check this hypothesis and will be able to do so as soon as a leaking low-temperature feedthrough seal is replaced.

#### FUTURE DEVELOPMENTS

In the following year this research will be continued with the aid of a fourth-year graduate student, Joel Parke, who will be visiting with Professor Ho Jun, Paik from the University of Maryland. Our goal is to check the inverse square law to the highest possible accuracy and to understand and control the temperature coefficient which remains at  $1.3^{\circ}$  K.

#### REFERENCES

1. D. R. Long, *Nature* 260, 417 (1976).
2. F. D. Stacy and G. J. Tuck, *Nature* 292, 230 (1981);  
S. C. Holding and G. J. Tuck, *Nature* 307, 714 (1984).
3. J. E. Moody and F. Wilczek, Preprint (1983) (Publication status unknown).

✓

APPENDIX 1



APPENDIX 2



# **SQUID APPLICATIONS TO GEOPHYSICS**

**Proceedings Of The Workshop Held 2-4 June 1980**

**At The**

**Los Alamos Scientific Laboratory**

**Los Alamos, New Mexico**

**Edited by**

**HAROLD WEINSTOCK**

**Office of Naval Research and  
Illinois Institute of Technology  
Chicago, Illinois**

**WILLIAM C. OVERTON, Jr.**

**Los Alamos Scientific Laboratory  
Los Alamos, New Mexico**

**Sponsored by  
the Office of Naval Research and  
the Los Alamos Scientific Laboratory**

**THE SOCIETY OF EXPLORATION GEOPHYSICISTS  
TULSA, OKLAHOMA  
1981**

## A SUPERCONDUCTING GRAVITY GRADIOMETER\*

Evan Mapoles<sup>†</sup>

### ABSTRACT

A gravity gradiometer has been developed which uses two superconducting proof masses to measure a single in line component of the gravity gradient tensor. A niobium coil positioned between the proof masses carries a persistent current which is modulated by the relative motion of the masses. This current signal is detected by a SQUID. We expect to achieve a sensitivity of  $10^{-9}/s^{-2} Hz^{-1/2}$ . Initial experiments indicate that the detector is working properly. An experiment to test the inverse square law of gravity at laboratory distances is planned.

### I. INTRODUCTION

During the past ten years a cryogenic transducer was developed at Stanford to convert a mechanical signal in an aluminum bar to an electrical signal for amplification (Paik, 1976). This transducer is currently used in the Stanford gravitational radiation experiment. The transducer is basically an accelerometer whose sensitivity is optimized for detection of the fundamental longitudinal mode of the bar.

Since 1975 we have been investigating the possibility of using this technology for gravity gradient measurement. Potential advantages include reduced thermal noise due to low temperature and higher mechanical Q's of materials, increased mechanical stability, and the use of SQUID's as very low noise amplifiers. Two prototype gradiometers using different methods of common mode rejection were assembled with components of gravity wave transducers (Paik, 1978). The operating principles of both systems

were confirmed experimentally, and one of the methods of common mode rejection was chosen for an advanced version.

In the past eighteen months we have designed and built this new gradiometer. It is a mechanically improved system designed for higher common mode rejection. Testing began in April, 1980. The mechanical and electrical design of this gradiometer, as well as some preliminary test results are discussed here.

### II. MECHANICAL CONSTRUCTION

The gradiometer consists of two proof masses held adjacent to each other with their sensitive axes along a line. The device measures a single diagonal component of the gravity gradient tensor. These two proof masses are carefully matched and aligned to minimize sensitivity to common acceleration. The sensor package is a cylinder 9.5 cm long and 11.5 cm in diameter. Each proof mass weighs 1.07 kg.

In order to achieve careful alignment of the proof mass sensitive axes, the components of the gradiometer are designed to stack up on each other. The faces of the parts are made as parallel as possible. This stack slides into a niobium housing tube, where it is locked together with two end rings which thread into the housing tube. With this method we expect the axes to be aligned to a few tens of microradians. Accelerations perpendicular to the gradiometer axis cause an error which is proportional to this angular misalignment. Consequently we expect to reject these cross accelerations to a few parts in  $10^5$ .

Each proof mass consists of an annular disc with a threaded central hole, two flat springs and

\* Work performed under the auspices of AFOSR

<sup>†</sup> Stanford University, Stanford, CA 94305

two ground plane pieces which screw into either side of the annular disc. The center of each spring is locked between the center disc and a ground plane. The entire assembly is niobium so that each proof mass has two superconducting surfaces which can be used to modulate readout coils. The rims of the two springs are held apart with a niobium ring which is fixed to the housing tube.

The flat springs are made from solid discs of niobium .318 cm thick and 10.48 cm in diameter. A rectangular depression is cut into the disc in three places  $120^\circ$  apart so that it is .071 cm thick in an area 3.8 cm by 2.2 cm. This area was cut out with an electron discharge machine. After the depressions were cut, a series of very narrow (.024 cm) slots were cut with a wire EDM machine. With these slots each rectangular depression becomes a folded cantilever spring. The center of the disc is thus weakly held with respect to the rim. The center is attached to the proof mass and the rim is fixed to the case.

The two proof mass subassemblies are held apart inside the housing tube with a third niobium ring. In the gap between the two adjacent superconducting ground planes a superconducting pickup coil is mounted. This coil is used to detect differential motion of the proof masses. Two additional coils are mounted facing the outer surfaces of the proof masses for detection of common motion. These also serve as magnetic springs which can be used to tune out any sensitivity to common acceleration along the gradiometer axis. Figure 1 shows a cross section of the gradiometer.

Except for the thin dielectric forms on which the coils are mounted the entire assembly is pure niobium. Since niobium undergoes a strain of  $1.43 \times 10^{-3}$  when cooled from room temperature to  $4.2^\circ \text{K}$ , all parts must be of the same material to prevent differential contraction from altering the geometry.

In order to calibrate the system, the gradiometer package is mounted on a fixture which allows it to be tilted by applying currents to two superconducting coils mounted in speaker magnets. The gradiometer is held by two cross-flex pivots perpendicular to its sensitive axes. The speaker coils apply a torque about this axis. If a tilt

$$\theta = \theta_0 \sin \omega_0 t$$

is applied to the gradiometer, an acceleration gradient

$$\Delta a = \frac{\omega_0^2 \theta_0^2}{2} \cos 2\omega_0 t$$

results. By measuring the amplitude of the second harmonic of the drive signal the instrument scale factor can be determined.

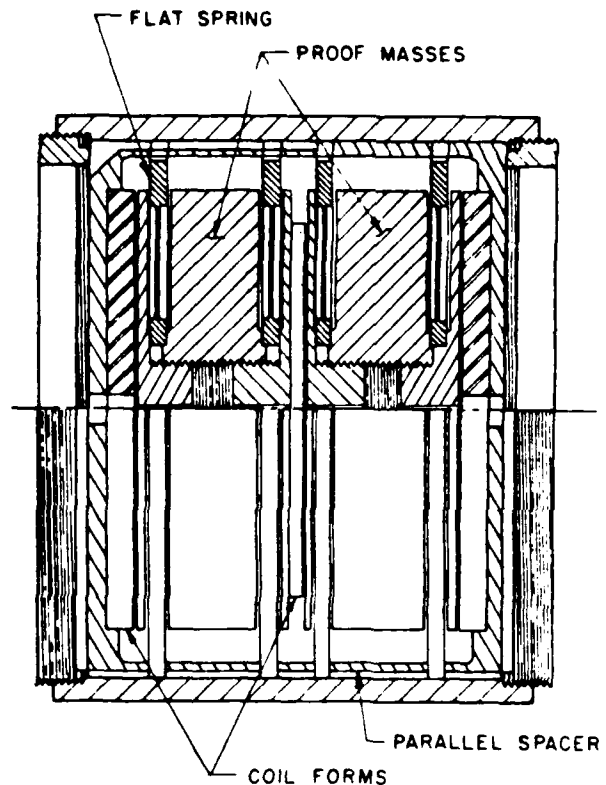


Figure 1. Gradiometer Cross Section

### III. ELECTRICAL CIRCUITS

The gradiometer contains two electrical circuits; one for detection of differential proof mass motion and one for common motion. Each is readout with a SQUID.

The differential circuit is shown in Figure 2. The coil mounted between the proof masses is a single layer of .0089 cm niobium wire wound in a spiral on a .254 cm wafer of machinable glass ceramic. This wafer is glued to one of the proof masses such that the surface of the wire is very close (.013 cm) to the other proof mass. Since magnetic field is excluded from the superconducting proof mass, the inductance of the pickup coil is controlled by the separation of the proof masses which changes in response

to gradients. A persistent current  $I$  is stored in a superconducting loop containing the pickup coil inductance  $L_p$  and is coupled to a SQUID via a superconducting transformer. Since the flux in this loop is fixed, as the proof mass separation changes a current  $i$  is generated in the SQUID input coil.

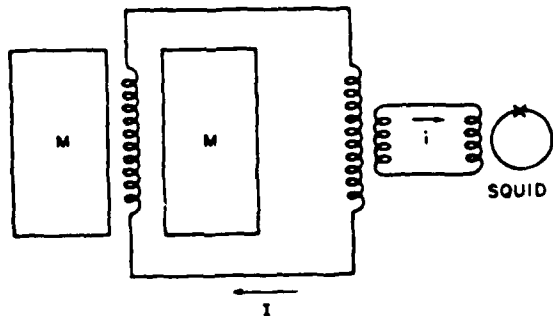


Figure 2. Differential Mode Detection Circuit

For an ideal transformer the detection sensitivity can be calculated from

$$i = \sqrt{\frac{L_p}{L_s}} \frac{GbI}{\omega^2 d}$$

where  $i$  is the signal current produced in the SQUID by an acceleration gradient  $G$ ,  $b$  is the proof mass separation,  $d$  is the spacing of the pickup coil from the other proof mass,  $\omega$  is the resonant frequency of the differential mode, and  $L_p$  and  $L_s$  are the pickup coil and SQUID input coil inductances. In order to optimize the sensitivity the gap  $d$  is made as small as practical, and the resonant frequency is minimized. Because it is difficult to make stable low frequency suspensions, we chose 60 Hz for  $\omega$ . This allowed us to use a practical thickness for our folded cantilever springs. With  $I = 8A$ , the SQUID noise gives a gradient noise of  $1E/\sqrt{Hz}$  ( $1E = 10^{-9} S^{-2}$ ).

This type of readout is sensitive to temperature changes because the penetration depth of the superconducting proof masses varies with temperature. As flux moves into the superconductor the coil inductance varies as if the surface were moving physically. The dependence of penetration depth  $\lambda$  on temperature is given by

$$\lambda(T) = \lambda_0 \left[ 1 - \left( \frac{T}{T_C} \right)^4 \right]^{-1/2}$$

(Tinkham, 1975) where  $\lambda_0 = 440 \text{ \AA}$  and  $T_C = 9.2^\circ \text{ K}$  for niobium. Taking the derivative with respect to temperature we find that at  $4.2^\circ \text{ K}$

$$\frac{d\lambda}{dT} = 9.7 \text{ A/K}$$

The differential displacement caused by a  $1 \text{ E}$  gradient is about  $2 \times 10^{-16} \text{ m}$ . Thus we must control the temperature to  $10^{-6} \text{ }^\circ \text{ K}$  to stabilize the gap. This requirement can be relaxed somewhat by operating the gradiometer at a lower temperature.

The circuit shown in figure 3 is used both to detect common motion of the proof masses and to fine tune the stiffness of the proof mass suspensions. The principle of detection is the same as that used in the differential circuit. Each proof mass modulates a persistent current in a flat coil facing its outer surface. The error signals generated by this motion are summed in a toroidal transformer and coupled to the input of a SQUID.

The field generated by the persistent currents provide a restoring force between the proof mass and the case when the mass is displaced from equilibrium. Hence, each pickup coil acts as a magnetic spring in parallel with the mechanical support springs. By varying the relative magnitudes of the persistent currents the stiffness of the two proof mass suspensions can be adjusted to be identical. In this case if the two experience a common acceleration along their sensitive axes they move the same distance and there is no change in the inductance of the differential pickup coil. A fourth coil on

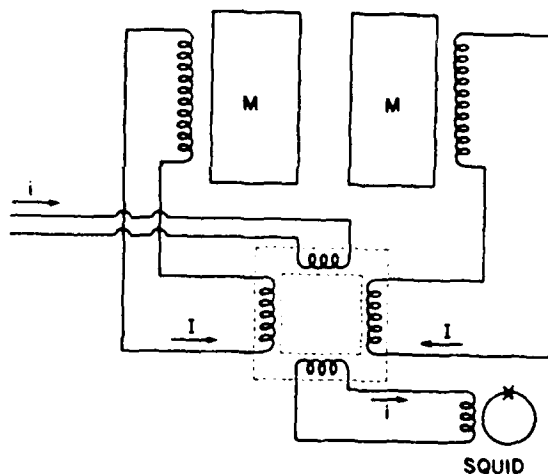


Figure 3. Common Mode Detection Circuit

the toroidal transformer is provided to vary the difference in the two persistent currents. A current in this coil couples flux in opposite directions into the two pickup loops. The currents vary to maintain the net flux constant.

#### IV. TEST RESULTS

Initial tests have been performed to check the basic properties of the instrument. The frequency of the differential mode is 62.7 Hz, and it has a Q of 400. This Q is limited by the construction of the gradiometer rather than the intrinsic Q of the material. The Q of 400 is sufficient to reduce thermal noise below  $1\text{E}/\sqrt{\text{Hz}}$ .

The scale factor of the instrument was measured using the internal tilting system with 2.0A stored in the differential pickup loop. An experimental value of 0.30  $\mu\text{V}/\text{E}$  was measured. This compares well with the theoretical value of 0.39  $\mu\text{V}/\text{E}$ . The reduction is probably due to flux leakage in the coupling transformer.

Common mode rejection was studied by tilting the cryostat by  $10^{-3}$  radians and observing the response of the differential readout. It was found that the response could be driven through zero by adjustment of the currents in the common mode pickup circuit as expected. The best matching obtained corresponded to a mismatch in the spring constants of  $5 \times 10^{-4}$ .

The noise power spectrum of the instrument was examined under several circumstances. During most experiments the cryostat was hung on latex tubing to form a low pass mechanical filter with a resonant frequency of 1.3 Hz. With this filter the noise level between 2 Hz and 10 Hz was below  $20\text{E}/\sqrt{\text{Hz}}$ . Below 1 Hz the noise level rises to  $550\text{E}/\sqrt{\text{Hz}}$ . The sources of noise have not been fully identified; however, we expect that the large increase in noise at low frequencies is due to thermal fluctuations. We expect this to improve with better temperature control. We also expect to improve the instrument's rejection of seismic noise by cooling the system in low magnetic field. This will eliminate pick-up from signal leads moving with respect to trapped flux in the instrument.

#### V. INVERSE SQUARE LAW TEST

Recently it has been suggested that the inverse square law of gravity may be violated at laboratory distances (Long, 1976). We are planning to use our gradiometer in a nearly null experiment to search for such a deviation. Since the gradiometer only measures gradients relative to an arbitrary zero, we must devise a test mass geometry which produces a nearly zero gravity gradient and compare the output of the instrument with and without the test mass present.

The test mass geometry we have chosen is a cylindrical shell large enough to fit over our cryostat. The gravity gradient at the center of this shell in the plane perpendicular to the cylinder axis is given by

$$g = \frac{GM}{R^2 L} \frac{(2R/L)^2}{[1+(2R/L)^2]^{3/2}}$$

where M, R, and L are the cylinder mass, radius and length. If  $L \gg R$  this gradient is nearly zero. Our cylinder will have a mass of  $3.2 \times 10^3$  kg, a length of 5.1 m and a radius of 25 cm so that  $L = 20 R$ . The central gradient is 6.7 E. We hope to measure this to an accuracy of 1%. This would allow us to see a deviation of 1 part in  $10^4$  from the inverse square law.

#### ACKNOWLEDGMENT

It is a pleasure to thank Professor William Fairbank and Professor Daniel Debra for their enthusiastic support.

#### REFERENCES

- Long, D. R., 1976, Experimental Examination of the Gravitational Inverse Square Law, *Nature*, V. 206, p. 417-418.
- Paik, H. J., 1976, Superconducting Tunable-Diaphragm Transducer for Sensitive Acceleration Measurement, *Journal of Applied Physics*, V. 47, no. 3, p. 1168-1178.
- Paik, H. J., 1978, Superconducting Gravity Gradiometers, *Future Trends in Superconductive Electronics* (Charlottesville, 1978), p. 166-170.
- Tinkham, M., 1975, *Introduction to Superconductivity* McGraw-Hill, p.80.

DISCUSSION

BROLLEY--Based on your experiment, what limit can you place on the rest mass of the graviton?

MAPOLES--It depends on the range in which we do the experiment. We can't really place (either an upper or lower) a limit on the rest mass. With this type of experiment, we can find the range of the violation to be outside of the range between 10 cm and 1 m. This corresponds to a range of rest masses for some particle other than the graviton. The graviton is well known to be massless.

PAIK--There are some indications that another type of graviton exists.

MAPOLES--The only reasonable way to interpret a violation is to say that there is another particle which has a rest mass.

PAIK--There is a theory which says there are scalar gravitons with mass.

BROLLEY--Can you separate spin differences?

MAPOLES--We can infer something about the spin from the sign of the force. By measuring the sign of the violation, one can discover something about the spin.

VERTON--When you cool the system down initially, unless you cool it down in a Helmholtz coil or in a magnetic shield, you will have frozen-in flux within the superconducting system. Does this affect the pickup from your coil? Does the trapped flux move?

MAPOLES--Yes. That is the leading problem in the pickup. In fact, it is even worse because I have actuators which are magnets. They have superconducting shields of their own, but a little more than the earth's field gets trapped in the superconducting structure. As the superconducting structure rotates with respect to those magnets, we do get a spurious effect. I think we can easily eliminate that problem.



DEVELOPMENT OF A SUPERCONDUCTING GRAVITY  
GRADIOMETER FOR A TEST OF THE INVERSE SQUARE LAW

by

Evan R. Mapoles

**Low Temperature Physics Group  
Department of Physics**



**STANFORD UNIVERSITY  
STANFORD, CALIFORNIA**

Supported by  
the Air Force Office of Scientific Research  
under Contract 80-0067

DEVELOPMENT OF A SUPERCONDUCTING GRAVITY GRADIOMETER  
FOR A TEST OF THE INVERSE SQUARE LAW

A DISSERTATION  
SUBMITTED TO THE DEPARTMENT OF PHYSICS  
AND THE COMMITTEE ON GRADUATE STUDIES  
OF STANFORD UNIVERSITY  
IN PARTIAL FULFILLMENT OF THE REQUIREMENTS  
FOR THE DEGREE OF  
DOCTOR OF PHILOSOPHY

By  
Evan R. Mapoles  
July 1981



## ABSTRACT

The inverse square law of gravitation is known to agree with astronomical data to very high accuracy, but recent theoretical and experimental work indicate that the inverse square law may be violated at distances less than 1000 km. Such a violation would signal the existence of a new force.

In order to check the inverse square law we are preparing to search for a non-newtonian force in a cylindrical shell. The cylindrical shell has the property that the newtonian effects nearly cancel, so that we are doing a nearly null experiment.

We have developed a superconducting gradiometer to measure the gravitational force gradients at the center of this cylindrical shell. By measuring both the vertical and horizontal gradients we can eliminate effects due to imperfections in the cylinder. This thesis describes the instrument and its performance as well as calculations of the sensitivity of the inverse square law test.

## ACKNOWLEDGEMENTS

It is a pleasure to thank the many people who have contributed to this work and helped me at various times.

First, I wish to express my gratitude to my advisor, William Fairbank, for his enormous enthusiasm and constant interest in this work.

It was a pleasure to work with Daniel DeBra and Russell Hacker of the Aeronautics and Astronautics department who have provided many ideas used in the design of the gradiometer.

I was fortunate to be able to work with Ho Jung Paik and Kai Wang in the early stages of this work, and Kristin Ralls in the later stages. I must also thank the various members of the Stanford Gravity Wave Group for many helpful discussions. These people include Bob Taber, Mike McAshan, Peter Michelson, Jim Hollenhorst, Robin Giffard and Massimo Bassan.

Wolfgang Jung and the physics department machine shop are responsible for the excellent machining of the gradiometer and Norman Rebok has been tremendously helpful in machining many parts on short notice.

I would also like to thank Jenifer Horrobin for her careful typing of this thesis.

TABLE OF CONTENTS

	<u>PAGE</u>
ABSTRACT . . . . .	i
ACKNOWLEDGEMENTS . . . . .	ii
INTRODUCTION . . . . .	1
Ch. 1 The Superconducting Gravity Gradiometer . . . . .	5
1.1 The Gravity Gradient Tensor . . . . .	5
1.2 The Superconducting Readout . . . . .	8
1.3 Mechanical Design of the Gradiometer . . . . .	15
1.4 Support Structure . . . . .	25
1.5 Magnetic Balancing and Common Mode Detection . . . . .	28
1.6 Feedback Damping . . . . .	34
Ch. 2 Experimental Evaluation of the Superconducting Gravity Gradiometer . . . . .	43
2.1 Balancing and Normal Modes . . . . .	43
2.2 Scale Factor Calibration and Noise . . . . .	48
2.3 Feedback . . . . .	59
2.4 Thermal Sensitivity . . . . .	63
2.5 Flux Creep . . . . .	68
2.6 Magnetic Sensitivity . . . . .	71
Ch. 3 Evidence for the Inverse Square Law . . . . .	73
3.1 Celestial Mechanics . . . . .	73
3.2 G Measurements . . . . .	76
3.3 Recent Experiments . . . . .	79
Ch. 4 Analysis of the Inverse Square Law Experiment . . . . .	81
4.1 Newtonian Field of a Cylindrical Shell . . . . .	81
4.2 Gradients Produced by the Yukawa Potential and the Logarithmic Potential . . . . .	94

	<u>PAGE</u>
4.3 Errors from Distortions of the Cylinder . . . . .	103
4.4 Errors from the Finite Size of the Gradiometer . . . . .	109
4.5 Experimental Procedure. . . . .	114
Ch. 5 Conclusions . . . . .	117
References. . . . .	118

## INTRODUCTION

Newton's inverse square law of gravitation is known to agree with astronomical data to very high accuracy and has been widely accepted as the correct force law in the static limit at all mass separations. However, it has recently been pointed out that existing experimental data allows large violations of the inverse square law at distances less than  $10^3$  km [Mikkelson 1977], [Long 1974], and several authors have proposed that the gravitational potential  $\phi(r)$  at a distance  $r$  from a point source of mass  $M$  has the form

$$\phi(r) = -\frac{GM}{r} [1 + \alpha e^{-\beta r}] , \quad [I.1]$$

where  $\alpha$  is a constant greater than  $-1$  and  $\beta$  and  $G$  are constants [Wagoner 1970], [Fujii 1971], [O'Hanlon 1972]. This potential has the property that if  $\beta r \gg 1$  the effect of the additional term is negligible and the inverse square law is recovered even if  $\alpha$  is of the order of unity. The gravitational force on a test mass  $m$  in this potential is given by

$$F = -\frac{G(r)Mm}{r^2} , \quad [I.2]$$

where

$$G(r) = G[1 + \alpha(1 + \beta r)e^{-\beta r}] . \quad [I.3]$$

Thus, if one measures the force between two particles as a function of separation in the presence of the potential [I.1] one would find that the gravitational constant  $G$ , as it is usually defined assuming an inverse square force law, is actually a function of mass separation. Long [Long 1976] claims to have observed such a variation in the gravitational constant. The expression

for  $G(r)$  in [I.3] has the interesting feature that for  $\beta r \gg 1$ ,  $G(r) = G$ , but if  $\beta r \ll 1$ ,  $G(r) = G(1 + \alpha)$ . Values of the gravitational constant are obtained from laboratory measurements with mass separations much less than 100 m, so if  $100 \text{ m} < \beta^{-1} < 10^6 \text{ m}$ ; then the value of  $G$  to be used in astronomical calculations is not the value measured in the laboratory. Evidence for and against a violation is reviewed in Chapter 3.

The possibility of a violation of the inverse square law, and the need for more accurate laboratory tests has motivated the work of this thesis. Using techniques of low temperature physics, we have developed an instrument for measuring gravitational gradients. The design and construction of this instrument are described in Chapter 1. The results of initial testing are described in Chapter 2.

This instrument is intended for use in an experimental test of the inverse square law. This test consists of measuring the three components of  $\nabla^2 \phi$  at the center of a cylindrical shell and verifying that  $\nabla^2 \phi$  is zero. Room temperature gravity gradiometers have been developed, [Forward 1973], [Bell 1977], [Trageser 1975], but these instruments are not able to check that  $\nabla^2 \phi$  is zero because they measure sheer gradients or linear combinations of sheer and in-line gradients. The gravitational gradients produced by an inverse square force law as well as those produced by the Yukawa potential of equation [I.1] in a cylindrical shell are calculated in Chapter 4. Various error sources are also considered in Chapter 4. These include positioning errors, errors due to the finite size of the instrument, and errors due to imperfections of the cylinder. By verifying that  $\nabla^2 \phi$  is zero one can eliminate all errors due to imperfections of the cylinder. In fact one could use any source geometry to check the inverse square law if one checks that  $\nabla^2 \phi = 0$  [Paik 1979]. However, the cylinder geometry offers

several large advantages because the gradients at the center of the cylinder produced by an inverse square force law are attenuated by the ratio of the diameter to the length squared. For our cylinder this factor is 0.01. Because of this the accuracy with which the instrument must be calibrated is also reduced by 100. Another advantage of the cylinder is the uniformity of the gradients inside. Because the gradients are so uniform near the center, the accuracy with which the gradiometer needs to be positioned is very low, and the effects of the finite size of the gradiometer are also much smaller than they are with other source geometries.

The size of the gradients in the cylinder, and the desire to measure vertical as well as horizontal gradients have influenced the design of the gradiometer. The gradiometer consists of two accelerometers whose sensitive axes lie along the same line. Relative motion of these masses is sensed so that a differential force over the separation of the masses is measured. This differential force or acceleration is an approximation of the true gradient. The proof masses are mechanically suspended with pairs of springs which provide very low compliance in all directions except along the sensitive axis of the gradiometer. However, there is a limit to how large a compliance can be allowed along the sensitive axis if the gradiometer is to be operated vertically and horizontally, because the proof masses will sag when the gradiometer is turned from horizontal to vertical. The need to keep the support springs relatively stiff puts a burden on the readout, since the displacements produced by gradients are reduced by stiff springs. For this reason we make use of an extremely sensitive superconducting readout described in section 1.2.

To get some idea of the displacement sensitivity required, let us calculate the displacement produced by an acceleration gradient of 1 E, where 1 E is a change in acceleration of  $10^{-9} \text{ m/s}^2$  over a distance of 1 m, or  $10^{-9}/\text{s}^2$ . The resonant frequencies of the spring-mass systems which make up the accelerometers are 60 Hz, and their separation is 3.2 cm, so a gradient of 1E produces a differential motion

$$\Delta x = \frac{(3.2 \text{ cm})(10^{-9} \text{ s}^{-2})}{(2\pi)^2 (60)^2 \text{ s}^{-2}} = 2.3 \times 10^{-14} \text{ cm.}$$

This is an extremely small displacement, but it is detectable with the inductance modulated readout and the SQUID magnetometer.

With a 60 Hz resonant frequency, the sag of an accelerometer under one g is

$$\Delta x = \frac{981 \text{ cm/s}^2}{(2\pi)^2 (60)^2 \text{ s}^{-2}} = 6.9 \times 10^{-3} \text{ cm.}$$

This number is small enough to allow the gradiometer to be oriented vertically or horizontally without changing internal components of the instrument.



## CHAPTER 1

### The Superconducting Gravity Gradiometer

#### 1.1 The Gravity Gradient Tensor

According to the classical theory of gravitation, the gravitational field in vacuum is described by a scalar potential  $\phi(\vec{r})$  which satisfies Poisson's equation. The force on a test particle of mass  $m$  is

$$\vec{F} = -m \vec{\nabla} \phi(\vec{r}). \quad [1.1]$$

The tidal forces generated by  $\phi$  are described by the gravity gradient tensor  $\Gamma$ , given by

$$\Gamma_{ij} = - \partial / \partial x_i [ \partial / \partial x_j \phi ] , \quad [1.2]$$

or

$$\Gamma = - \begin{bmatrix} \frac{\partial^2 \phi}{\partial x^2} & \frac{\partial^2 \phi}{\partial y \partial x} & \frac{\partial^2 \phi}{\partial z \partial x} \\ \frac{\partial^2 \phi}{\partial x \partial y} & \frac{\partial^2 \phi}{\partial y^2} & \frac{\partial^2 \phi}{\partial z \partial y} \\ \frac{\partial^2 \phi}{\partial x \partial z} & \frac{\partial^2 \phi}{\partial y \partial z} & \frac{\partial^2 \phi}{\partial z^2} \end{bmatrix} . \quad [1.3]$$

The elements of  $\Gamma$  are subject to four constraints since

$$\Gamma_{ij} = \Gamma_{ji} , \quad [1.4]$$

and

$$\sum_j \Gamma_{jj} = 0 , \quad [1.5]$$

since  $\phi$  satisfies Poisson's equation. This leaves five independent components. In addition to gradients due to the gravitational field, there are other gradients present if the sensor is not operated in an inertial reference frame. These affects basically arise from the centripetal forces on the proof masses when the sensor rotates with respect to inertial space. Suppose that the gradiometer is fixed in some noninertial frame  $O'$  as shown in figure 1.1. If  $\vec{r}$  is the gradiometer position in the inertial frame  $O$  and  $\vec{r}'$  is its position in the  $O'$  frame, and the  $O'$  frame has an angular velocity  $\vec{\omega}$ , then

$$d^2\vec{r}/dt^2 = \ddot{\vec{r}}' + 2\vec{\omega} \times \dot{\vec{r}}' + \dot{\vec{\omega}} \times \vec{r}' + \vec{\omega} \times (\vec{\omega} \times \vec{r}'). \quad [1.6]$$

If the gradiometer is at rest in  $O'$  the first two terms are zero, then

$$d^2\vec{r}/dt^2 = \dot{\vec{\omega}} \times \vec{r}' + \vec{\omega} \times (\vec{\omega} \times \vec{r}'). \quad [1.7]$$

To calculate the acceleration gradients we need to calculate

$$\Gamma'_{ij} = -\frac{\partial}{\partial r'_i} \left[ \frac{d^2\vec{r}}{dt^2} \cdot \hat{j}' \right]. \quad [1.8]$$

The vector  $\vec{\omega}$  is fixed in the primed frame so

$$\begin{aligned} \dot{\vec{\omega}} \times \vec{r}' &= \hat{i}'(\dot{\omega}_y z' - \dot{\omega}_z y') - \hat{j}'(\dot{\omega}_x z' - \dot{\omega}_z x') \\ &\quad + \hat{k}'(\dot{\omega}_x y' - \dot{\omega}_y x'), \end{aligned} \quad [1.9]$$

and

$$\begin{aligned} \vec{\omega} \times (\vec{\omega} \times \vec{r}') &= \hat{i}' \left[ -(\omega_y^2 + \omega_z^2)x' + \omega_y \omega_x y' + \omega_x \omega_z z' \right] \\ &\quad + \hat{j}' \left[ \omega_y \omega_x x' - (\omega_x^2 + \omega_z^2)y' + \omega_y \omega_z z' \right] \\ &\quad + \hat{k}' \left[ \omega_z \omega_x x' + \omega_z \omega_y y' - (\omega_x^2 + \omega_y^2)z' \right]. \end{aligned} \quad [1.10]$$

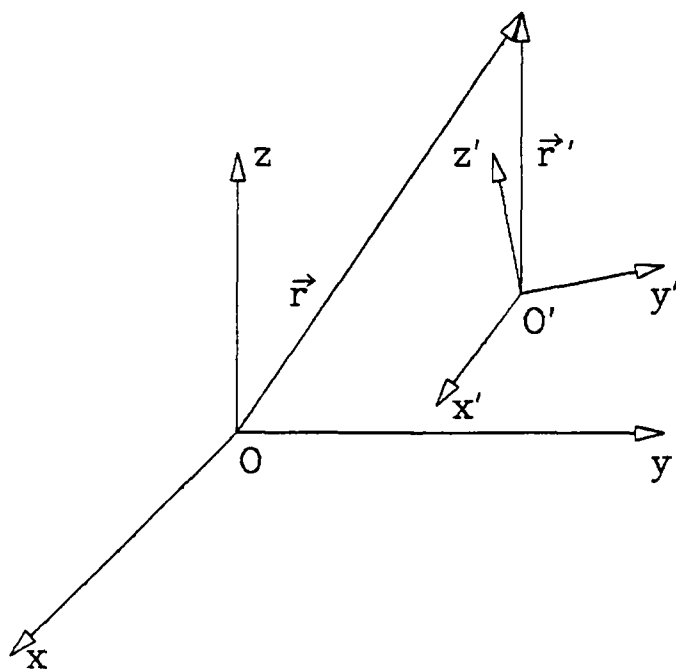


Figure 1.1 Rotating Coordinates

Taking the partials we have

$$\Gamma' = \begin{bmatrix} \dot{\omega}_y^2 + \dot{\omega}_z^2 & -\dot{\omega}_z - \omega_y \omega_x & \dot{\omega}_y - \omega_x \omega_z \\ \dot{\omega}_z - \omega_y \omega_x & \dot{\omega}_x^2 + \dot{\omega}_z^2 & -\dot{\omega}_x - \omega_y \omega_z \\ -\dot{\omega}_y - \omega_z \omega_x & \dot{\omega}_x - \omega_z \omega_y & \dot{\omega}_x^2 + \dot{\omega}_y^2 \end{bmatrix} \quad [1.11]$$

The instrument which we will describe here measures a diagonal component of  $\Gamma$  or  $\Gamma'$ , hence we are interested in error terms of the form  $\omega_i^2 + \omega_j^2$ . Suppose that the sensitive axis is along the x direction and the instrument is given a tilt about the z axis

$$\theta = \theta_0 \cos \omega t \quad [1.12]$$

Then

$$\dot{\omega}_z = \dot{\theta} = \omega \theta_0 \sin \omega t, \quad [1.13]$$

and

$$\omega_z^2 = \frac{\theta_0^2 \omega^2}{2} (1 - \cos 2\omega t). \quad [1.14]$$

The gradient consists of a component at  $2\omega$  and a d.c. component  $\theta_0^2 \omega^2 / 2$ . This latter term represents a serious source of error since it increases as the square of the frequency. For instance, an angular velocity of  $3 \times 10^{-5}$  rad/sec or  $6^\circ$  per hour produces an equivalent gravity gradient  $1E = 10^{-9} / \text{sec}^2$ .

## 1.2 The Superconducting Readout

The superconducting readout circuit is shown in figure 1.2. It consists of an inductor  $L_1$  rigidly attached to one of the proof masses and coupled to a SQUID by a superconducting transformer.  $L_1$  is located as closely as

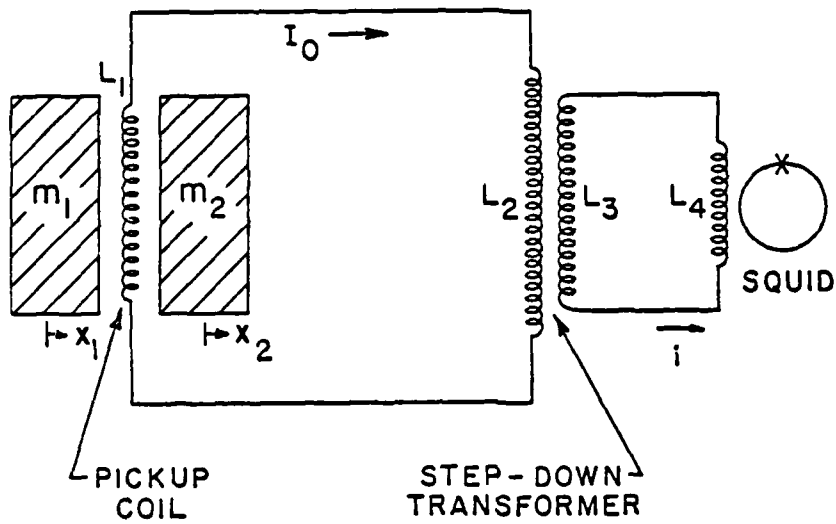


Figure 1.2 Differential Readout Circuit

possible to the surface of the other proof mass so that its inductance is strongly modulated by relative motion of the two proof masses. A persistent current is stored in the loop consisting of  $L_1$  and  $L_2$ . Since the total flux in this loop must remain constant, a change in the inductance of  $L_1$  causes a change in the current which is detected by the SQUID.

The inductor  $L_1$  is a spiral of niobium wire wound on a flat dielectric substrate. This flat circular coil is glued to one of the proof masses. A flat superconducting plane which is attached to the second proof mass is located about 5 mills from the coil. The readout coil is shown in figure 1.7. According to Ampere's law the field  $B$  produced by a current  $I$  in the coil is

$$B = n\mu_0 I, \quad [1.15]$$

where  $n$  is the number of turns per unit length in the coil. This field occupies a volume  $As$  where  $A$  is the area of the coil and  $s$  is coil proof mass spacing, so that

$$L_1 = \mu_0 n^2 As. \quad [1.16]$$

This can be rewritten as

$$L_1 = L_1^0 \left[ 1 + \frac{x_2 - x_1}{d} \right], \quad [1.17]$$

where

$$L_1^0 = \mu_0 n^2 Ad, \quad [1.18]$$

and  $d$  is the equilibrium spacing between the proof masses.

We can write the equations of motion of the two proof masses as

$$\begin{aligned} m\ddot{x}_1 + kx_1 &= -\alpha I^2/2 \\ m\ddot{x}_2 + kx_2 &= \alpha I^2/2, \end{aligned} \quad [1.19]$$

where  $\alpha = L_1^0/d = \mu_0 n^2 A$ . We have ignored any damping and any mechanical mismatch between the proof masses. If  $\zeta = x_2 - x_1$  we have

$$\ddot{\zeta} + \omega_0^2 \zeta = \frac{\alpha I^2}{m}, \quad [1.20]$$

where  $\omega_0^2 = k/m$ . As current is stored in  $L_1$  the magnetic field pushes the proof masses apart and  $d$  increases. If  $h$  is the spacing with zero current, then

$$d = h + \frac{\alpha I_0^2}{m\omega_0^2}, \quad [1.21]$$

where  $I_0$  is the mean value of the persistent current and  $d$  is the mean value of the coil proof mass spacing. Now if we define  $\xi = \zeta - \alpha I_0^2/m\omega_0^2$  the equation of motion becomes

$$\ddot{\xi} + \omega_0^2 \xi = \frac{\alpha}{m} [I^2 - I_0^2]. \quad [1.22]$$

Since flux in any superconducting loop is fixed, we have two constraints

$$\phi_1 = (L_1 + L_2)I - Mi = (L_1^0 + L_2)I_0 \quad [1.23a]$$

$$\phi_2 = (L_3 + L_4)i - MI = -MI_0, \quad [1.23b]$$

where  $M$  is the mutual inductance of the transformer in figure 1.2. The mean value of  $i$  is forced to be zero when current is stored with a heat switch which causes part of the loop to go normal. Solving for  $I$  and  $i$ , we find

$$I = I_0 \left[ \frac{(L_1^0 + L_2)(L_3 + L_4) - M^2}{(L_1 + L_2)(L_3 + L_4) - M^2} \right], \quad [1.24]$$

and

$$i = \frac{-I_0 M (L_1 - L_1^0)}{(L_1 + L_2)(L_3 + L_4) - M^2}. \quad [1.25]$$

If we let  $(L_1^0 + L_2)(L_3 + L_4) - M^2 = L^2$  and expand  $L_1 = L_1^0 \left[ 1 + \frac{\xi}{d} \right]$ , then to lowest order in  $\xi$

$$i = \frac{-ML_1^0 I_0 \xi}{L^2 d}. \quad [1.26]$$

Using [1.24] we can write the equation of motion [1.22] as

$$\ddot{\xi} + \omega_0^2 \xi = \frac{\alpha}{m} I_0^2 \left[ 1 + \frac{\alpha(L_3 + L_4)}{L^2} \xi \right]^{-2} - \frac{\alpha I_0^2}{m}. \quad [1.27]$$

Expanding the right side and keeping the lowest order in  $\xi$ , we have

$$\ddot{\xi} + \omega_0^2 \xi = \frac{-2\alpha^2 I_0^2 (L_3 + L_4) \xi}{mL^2}. \quad [1.28]$$

This expression gives the frequency shift of the differential mode with persistent current  $I_0$ , but  $L$  is not independent of  $I_0$ . So let us write

$$L_1^0 = \alpha \left[ h + \frac{\alpha I_0^2}{m\omega_0^2} \right], \quad [1.29]$$

and define

$$L_0^2 = (\alpha h + L_2)(L_3 + L_4) - M^2. \quad [1.30]$$

Then we can write [1.28] as

$$\ddot{\xi} + \omega_0^2 \xi = \frac{-2\alpha^2 I_0^2 (L_3 + L_4)}{mL_0^2} \left( 1 + \frac{\alpha^2 I_0^2 (L_3 + L_4)}{mL_0^2 \omega_0^2} \right)^{-1} \xi, \quad [1.31]$$



or we can write frequency of the differential mode  $f$  as

$$f^2 = f_o^2 + \frac{2\alpha^2 I_o^2 (L_3 + L_4)}{(2\pi)^2 m L_o^2} \left\{ 1 + \frac{\alpha^2 (L_3 + L_4) I_o^2}{m L_o^2 \omega_o^2} \right\}^{-1} \quad [1.32]$$

The behavior of  $f^2$  versus  $I_o^2$  is shown in figure 1.3.  $f^2$  increases rapidly initially with a slope of  $2\alpha^2 I_o^2 (L_3 + L_4) / (2\pi)^2 m L_o^2$  but quickly rolls off and approaches the asymptotic value of  $3f_o^2$ . To find an optimal value of  $I_o$ , note that a gravity gradient  $G$  produces a differential displacement of the proof masses  $Gb / (2\pi f)^2$  where  $b$  is the gradiometer baseline. So from [1.26]

$$i = \frac{-ML_1^o I_o Gb}{(2\pi)^2 L_o^2 d} \left\{ f_o^2 + \frac{2\alpha^2 I_o^2 (L_3 + L_4)}{(2\pi)^2 m L_o^2} \left[ 1 + \frac{\alpha^2 I_o^2 (L_3 + L_4)}{m L_o^2 \omega_o^2} \right]^{-1} \right\}^{-1} \left[ 1 + \frac{\alpha^2 (L_3 + L_4) I_o^2}{m L_o^2 \omega_o^2} \right]^{-1}$$

$$= \frac{-ML_1^o I_o Gb}{(2\pi)^2 L_o^2 d} \left\{ f_o^2 + \frac{3\alpha^2 I_o^2 (L_3 + L_4)}{(2\pi)^2 m L_o^2} \right\}^{-1} \quad [1.33]$$

From this it follows that  $i/G$  is maximized when

$$I_o^2 = I_{op}^2 = \frac{\omega_o^2 m L_o^2}{3\alpha^2 (L_3 + L_4)} \quad [1.34]$$

Substituting this into the brackets of [1.33] gives

$$\frac{i}{G} = \frac{-ML_c I_o b}{2\omega_o^2 L_o^2 h} \quad [1.35]$$

where  $L_c = \alpha h$ . To impedance match, we construct the transformer so that

$L_2/L_c = L_3/L_4 = \gamma$ , and we assume that  $M \approx \sqrt{L_2 L_3}$ . Then

$$\frac{i}{G} = \frac{-\gamma b I_o^2}{(1+2\gamma)h 2\omega_o^2} \sqrt{\frac{L_c}{L_4}} \quad [1.36]$$

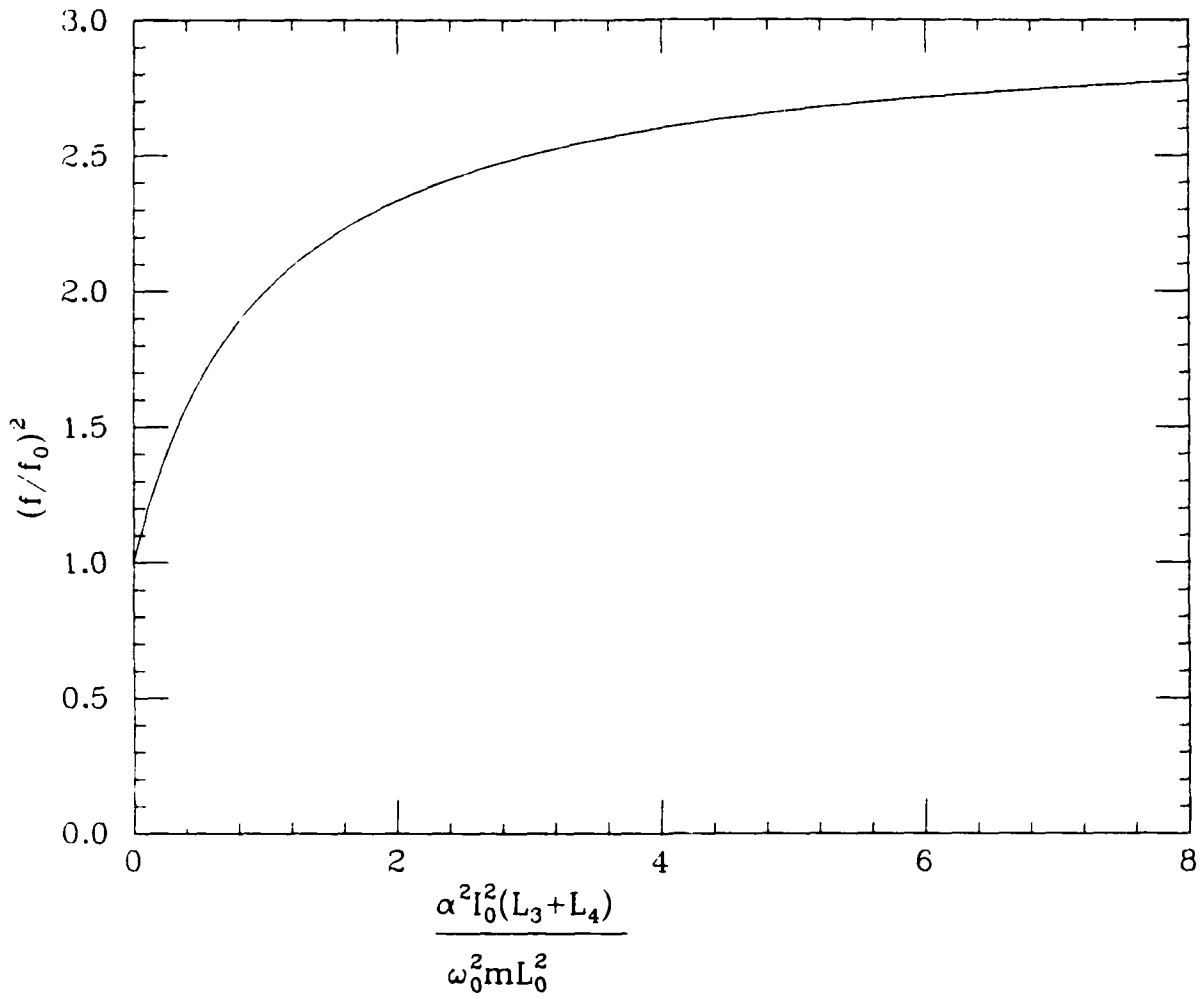


Figure 1.3 Frequency shift of the differential mode.

is the scale factor of the gradiometer. This is optimized for  $\gamma \gg 1$ , but any value greater than one gives a scale factor close to the optimal.

One consequence of [1.36] is that the scale factor increases as  $\omega_0^{-1}$  rather than  $\omega_0^{-2}$  if the resonant frequency of the gradiometer proof masses is reduced keeping their masses constant, since  $I_{op}$  is proportional to  $\omega_0$ . This is a consequence of the current causing the gap between the proof masses to increase as well as the increase of spring constant provided by the electrical spring. Another interesting consequence of [1.36] is that the scale factor increases only as  $1/\sqrt{h}$  since  $L_C$  is proportional to  $h$ .

### 1.3 Description of the New Gradiometer

Our primary goal in the design and fabrication of our gravity gradiometer was to minimize the instrument's sensitivity to linear accelerations both along the proof mass direction and perpendicular to it. Linear accelerations in the laboratory exert forces on the proof masses which are very large compared to the gravitational forces we would like to measure, so careful balancing of the gradiometer is needed to eliminate them as a noise source.

In addition, we decided to build an in-line gradiometer which measures one of the diagonal components of  $\Gamma$ . As we will show in Chapter 4, it is highly desirable to be able to measure all three components of  $\nabla^2\phi$  so we chose a method for suspending the proof masses which allows us to operate the gradiometer with its sensitive axis vertical as well as horizontal.

In order to make the balancing problem manageable we chose a mechanical design which enabled us to use only one coil in the readout system described in section 1.2. Experiments have been done with readouts using several

coils, [Paik 1978] but in these gradiometers careful matching of the coils as well as the proof masses is necessary to reject linear accelerations.

Basically the gradiometer consists of two superconducting proof masses adjacent to each other. A single niobium coil is mounted in the gap between the proof masses so that the coil inductance is proportional to their spacing. This readout system is analyzed in detail in the previous section. Since the sensitive axes of the proof masses are parallel, the gradiometer detects changes in one of the diagonal components of the gravity gradient tensor,  $\Gamma_{jj}$ .

Each of the two proof masses is supported with two mechanical springs. The mechanical springs are folded cantilevers cut into circular disks of niobium. A folded cantilever with two-fold symmetry is shown in figure 1.4. In this case the thickness of the plate is reduced in the two rectangular areas hatched in the figure in order to restrict the bending to those areas. Slots are then cut in the indicated locations. These slots allow the center to move perpendicular to the plane of the plate as shown in the lower part of the figure. Since the center of the spring is free to move in the plane of the plate, the total length of the spring remains constant and the restoring force is provided by pure bending without stretching of the spring material. The stiffness can be calculated using the cantilever equation [Landau 1959]. In the case shown the spring displacement  $\delta$  is

$$\delta = \frac{4f\ell^3}{wEh^3}, \quad [1.37]$$

where  $f$  is the force in the center,  $h$  is the cantilever thickness,  $E$  is the Young's modulus of the material and  $\ell$  and  $w$  are the lengths shown in figure 1.5. The spring constant  $k$  is

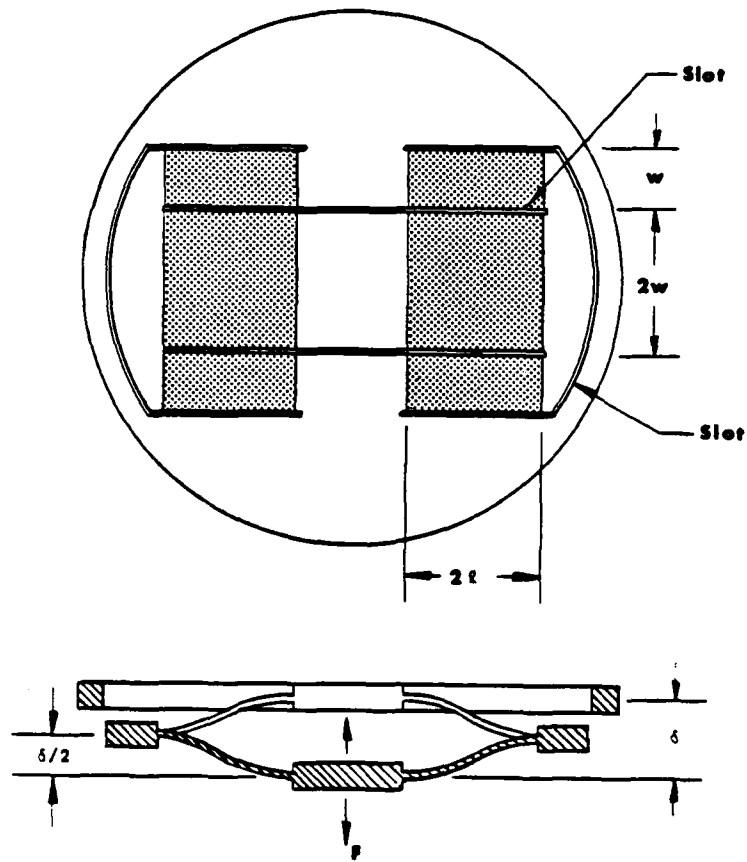
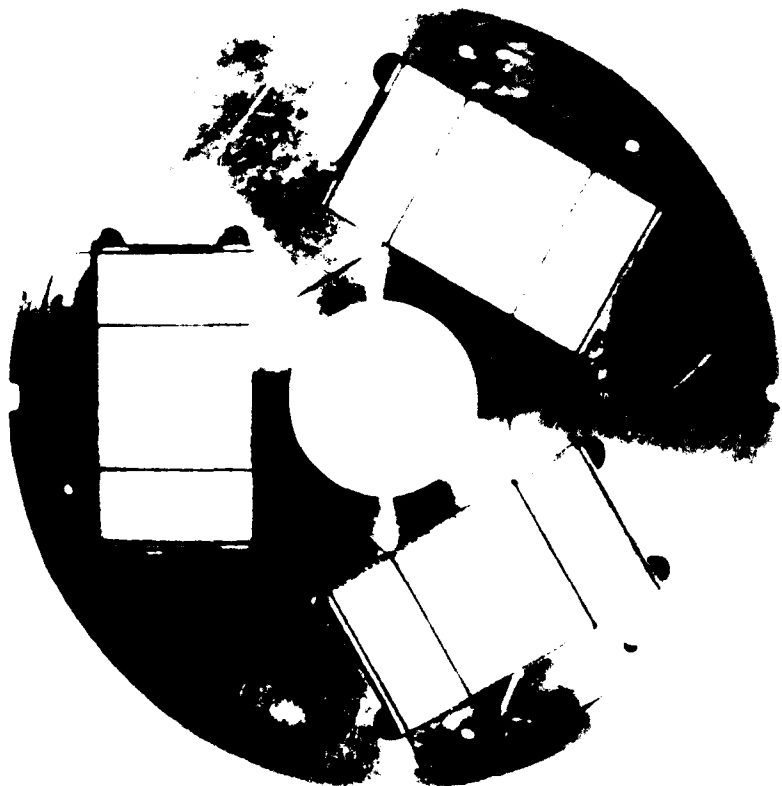


Figure 1.4 Folded Cantilever Spring



300 METERS

Figure 1.5 Gradiometer Spring

$$k = \frac{f}{\delta} = \frac{Ewh^3}{4\ell^3} . \quad [ 1.38]$$

The springs used in the gradiometer have three-fold symmetry rather than two and a picture of one of them is shown in figure 1.5. Since two such springs are used to support each proof mass, there are three pairs of cantilevers, and the net spring constant for each proof mass is

$$k = \frac{3}{4} \frac{Ewh^3}{\ell^3} . \quad [ 1.39]$$

These springs were fabricated from solid disks of niobium 10.5 cm in diameter and 0.32 cm thick. The faces were carefully machined to produce a final thickness uniformity of approximately 50 microns. The rectangular depressions were milled to within a few thousandths of an inch of their final thickness, and the part was then stress relieved. In the next machining stage, the rectangular depressions were cut to their final thickness of 0.071 cm using electron discharge machining (EDM) with a rectangular electrode of copper and graphite. EDM was used to achieve a careful match of all of the cantilevers, and thereby match the final proof mass frequencies. In the final stage of machining the narrow slots were cut using wire EDM. In this process wire is continuously circulated through the part and used as an electrode. The part is moved on a numerically controlled table as the slot is cut.

The proof mass subassembly consists of two springs, two cover pieces, an annular mass, and a ring used to hold the edges of the springs apart. The cover pieces are circular disks of niobium 8.51 cm in diameter which are flat on one side and have a threaded stud on the opposite side. The flat sides are designed to modulate the inductance of the readout coil or tuning coils described in section 1.2. The flats were polished to ensure

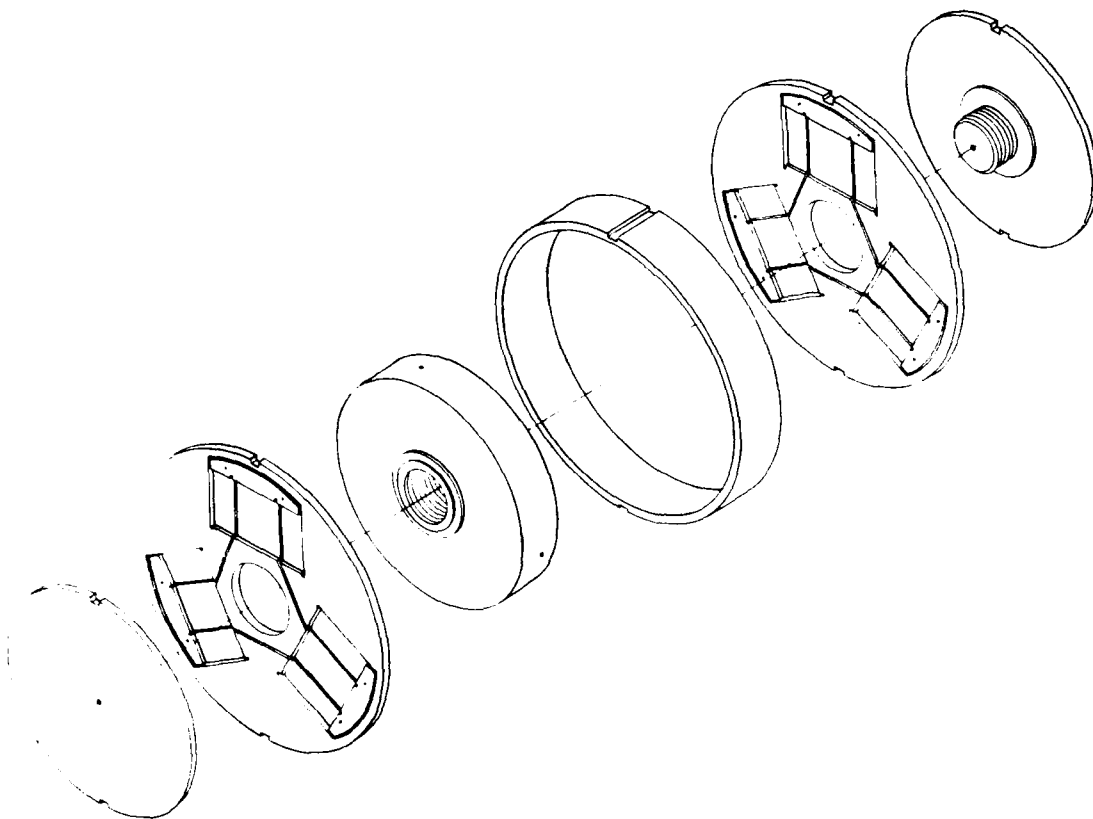


Figure 1.6 Exploded View of a Proof Mass Subassembly



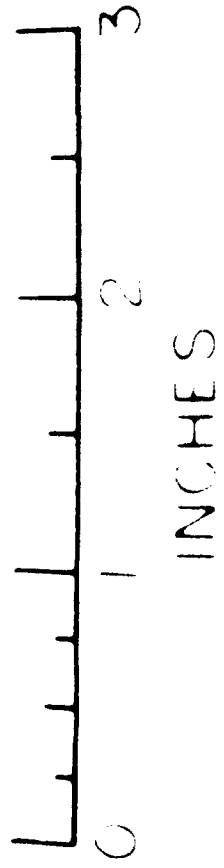
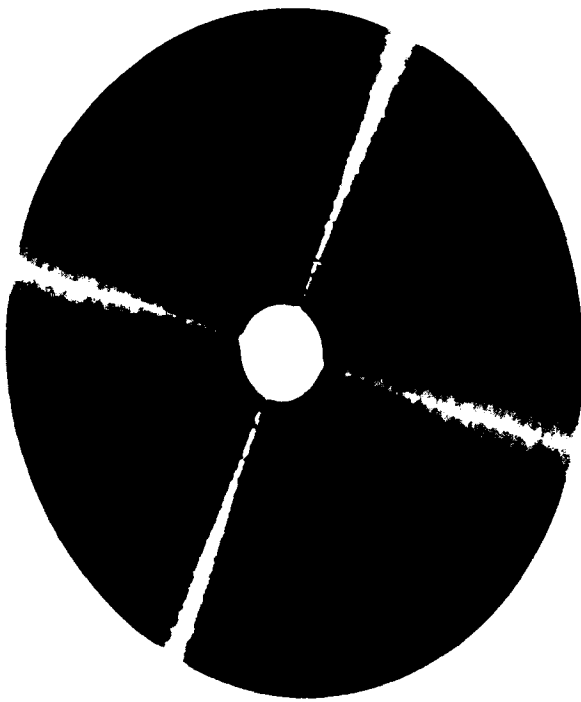


Figure 1.7 Differential Readout Coil

flatness and isotropy so that close spacing to the coils could be obtained, and so that the inductance of the coils is modulated only by linear motion of the surfaces. The threaded studs screw into an annular disk of niobium which provides the bulk of the mass for each proof mass. A spring is captured between each cover piece and proof mass. An exploded view of one of the two proof mass subassemblies is shown in figure 1.6. The ring which is used to maintain the spacing of the edges of the springs is thicker than the proof mass so that each spring is biased away from its equilibrium position and never passes through its zero point. This eliminates certain forms of nonlinear behavior. Since the springs have opposite biases, the first order nonlinear terms also cancel. The ring was ground to its final thickness to keep its two sides parallel to one part in  $10^5$ .

By using a design in which all of the parts stack up on each other, and all parts have highly parallel surfaces, we ensure that the sensitive axes of the two proof masses are also parallel. This parallelism is maintained in all the parts to a few parts in  $10^5$ .

The readout coil is shown in figure 1.7. It is a single layer of 0.0089 cm diameter niobium wire wound on a 0.25 cm thick disk of macor. The coil has 400 turns and a diameter of 6.9 cm. The lead to the center of the coil is glued into a slot in the macor substrate so that both leads come off the edge of the coils. The macor coil form is glued to one of the four cover pieces. This cover piece is 0.06 cm thinner than the other three to compensate for the coil form mass.

Once the two proof mass subassemblies were constructed, they were stacked on top of each other with a ring holding them apart. The thickness of the ring was chosen so that the readout coil is about 0.013 cm from the opposite proof mass. This structure was mounted on an aluminum fixture which

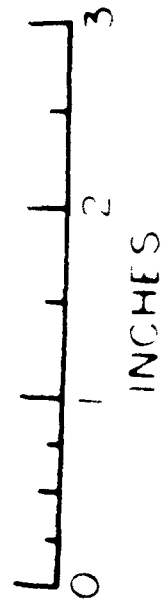


Figure 1.8 Tuning Coils

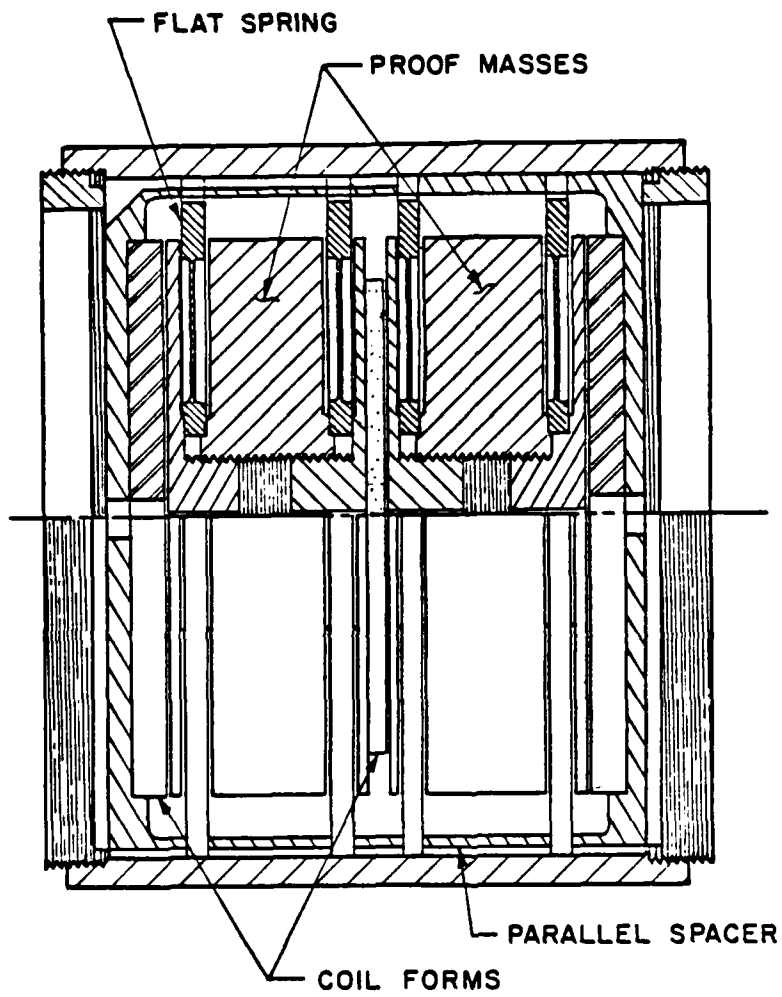


Figure 1.9 Gradiometer Cross Section

maintained the angular orientation of the parts. A niobium housing tube 9.3 cm long with a 10.5 cm inside diameter was placed over the parts.

The ends of the assembly are sealed with a pair of tuning and feedback coils shown in figure 1.8. The inner coil on each form is currently used to match the resonant frequencies of the proof mass subassemblies as described in section 1.5. The annular outer coil was included for future use as a feedback coil. Fixtures for making superconducting joints and heat switches are mounted on the opposite sides of these tuning coils. There is also a superconducting transformer mounted on each tuning coil; one for the differential readout circuit and one for the common mode readout circuit.

The entire assembly is locked together with a pair of rings which screw into either side of the housing tube. A cross section of the assembled gradiometer is shown in figure 1.9. The assembled gradiometer has a baseline of 3.2 cm.

All of the gradiometer components, except for the dielectric coil forms, are niobium. Since niobium undergoes a contraction of  $1.4 \times 10^{-3}$  when cooled to  $4.2^{\circ}\text{K}$ , all parts must be made of niobium to prevent differential contraction from altering the geometry.

#### 1.4 The Gradiometer Support Assembly

The gradiometer is supported on an aluminum and titanium fixture in the cryostat which allows the gradiometer axis to be positioned vertically or horizontally. This fixture holding the housing tube is shown in figure 1.10. The housing tube is clamped between two titanium pieces which bolt together above and below the gradiometer as in figure 1.11b. This part is

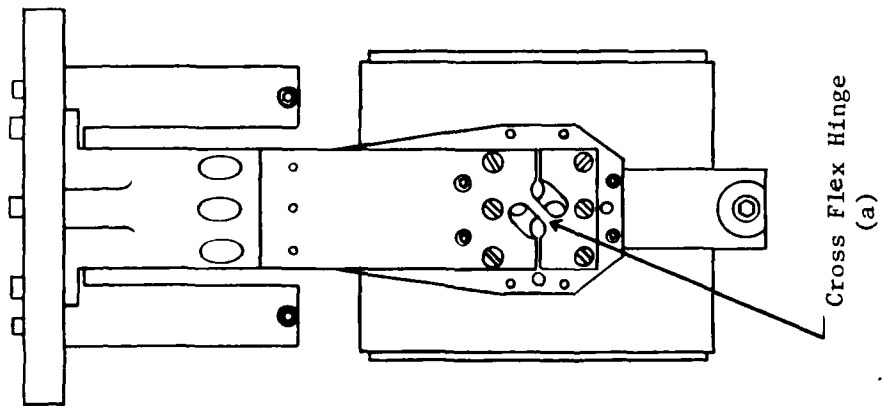
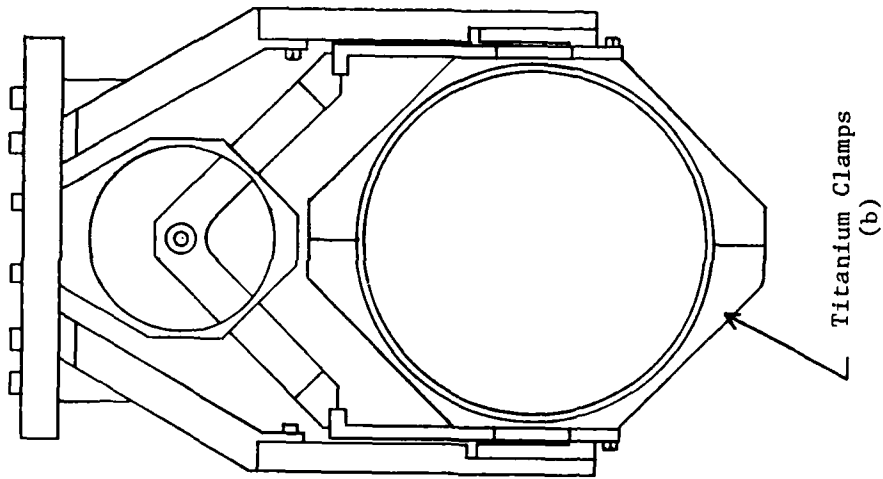


Figure 1.11 (a) Side View of Support Fixture  
(b) Front View of Support Fixture

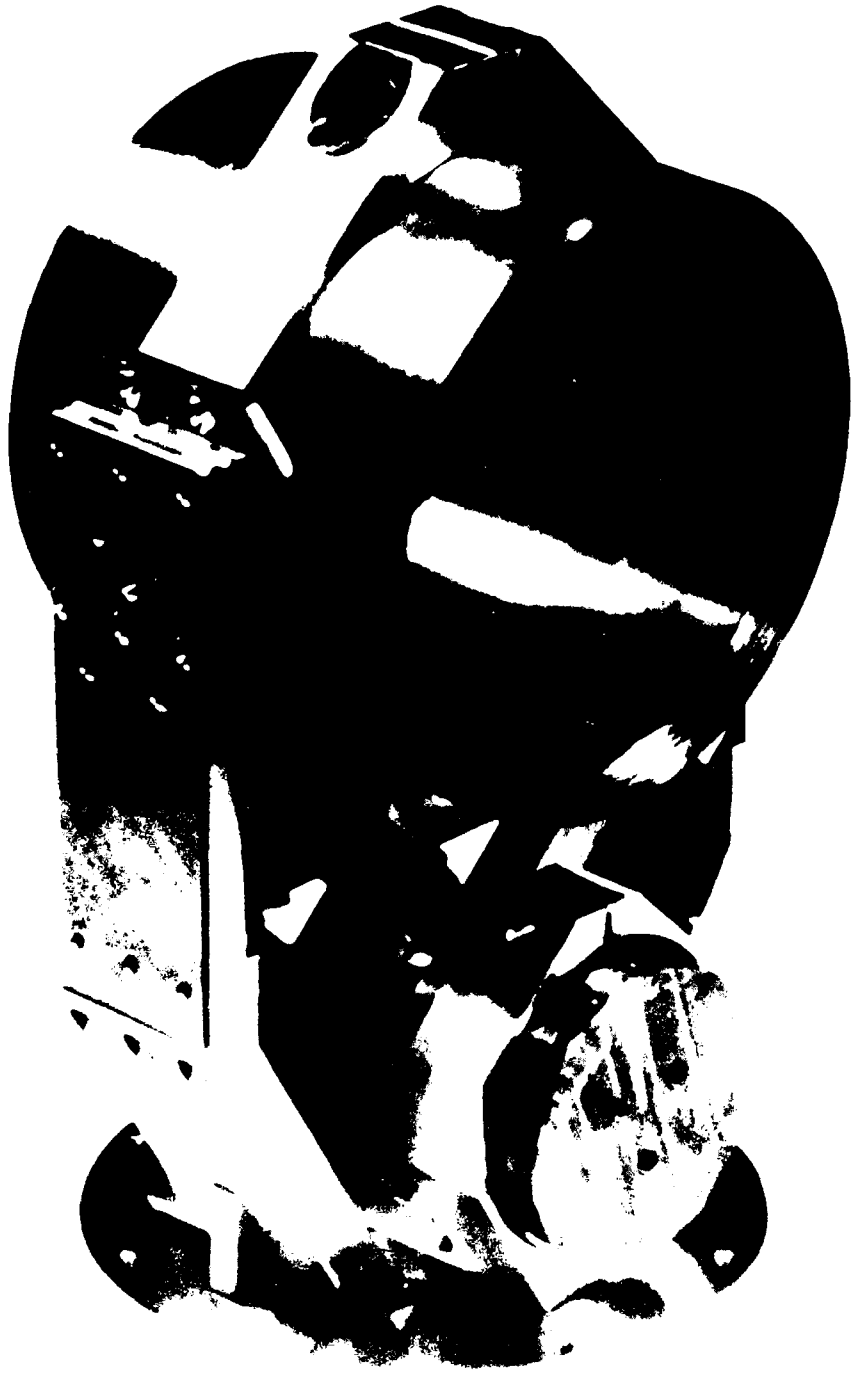


Figure 1.10. Grid Vector Support Fixture

clamped to the bottom of a pair of cross flex hinges shown in 1.11a. These hinges allow the gradiometer to be tilted inside the vacuum chamber of the cryostat to produce test signals. Titanium is used for the parts which make contact with the gradiometer because its thermal contraction is a good match to that of niobium.

Mechanical force is transmitted to these hinges by a pair of arms inside the aluminum support beams. These arms are rigidly attached to the gradiometer with an arm that a mechanical force is applied to in order to apply torque to the hinges.

Two methods of applying torque to the assembly have been used. In the first experiments with the gradiometer a pair of superconducting solenoids were attached to the torquer arm and inserted into the gaps of a pair of permanent magnets fixed to the top plate. Current with opposite polarity in the solenoids produces an angular deflection of the gradiometer. This arrangement was replaced with a pair of PZT bimorphs later because flux from the magnets was trapped in the gradiometer as it was cooled through its transition temperature, and this flux may have caused additional coupling of the readout to mechanical motion.

#### 1.5 Magnetic Tuning and Common Mode Detection

Even with excellent machining tolerances the mechanical springs can only be matched to a few percent. Since we have designed the system to reject cross accelerations to a few parts in  $10^5$  we would like to improve the frequency matching to this level also. In this case an equal force on both masses will produce the same displacement, and the inductance of the readout coil will be unchanged. To accomplish this, we have a magnetic



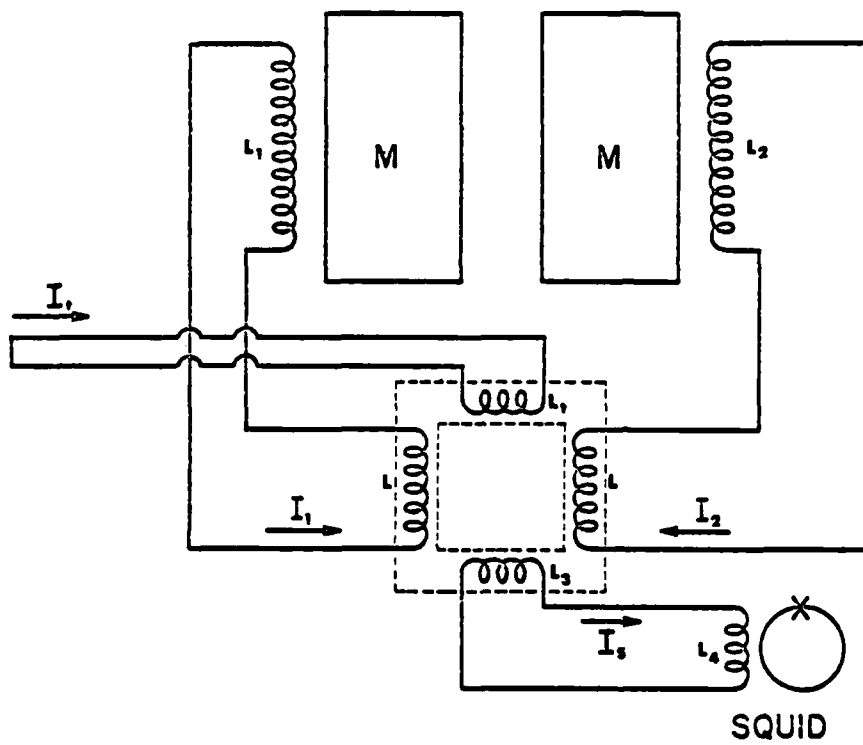


Figure 1.12 Tuning and Common Mode Detection Circuit

tuning circuit in the gradiometer which adjusts the relative stiffnesses of the proof mass suspensions with respect to the case.

The circuit is shown in figure 1.12. The two inner coils of figure 1.8 are attached to matched inductors of a toroidal core. A third winding on this core is used to adjust the currents in these loops. A fourth winding on this core couples to a SQUID which detects common mode motion of the proof masses. Its inductance is much smaller than the other three and will be ignored in calculating the frequency shifts caused by currents in the other three loops.

The inductances  $L_1$  and  $L_2$  are given by

$$L_1 = L_1^0 \left[ 1 + \frac{x_1}{d_1} \right] , \quad [1.40a]$$

and

$$L_2 = L_2^0 \left[ 1 + \frac{x_2}{d_2} \right] . \quad [1.40b]$$

where  $L_1^0 \approx L_2^0$  and  $d_1 \approx d_2$ . The flux equations for the three loops are

$$\phi_1 = (L_1 + L)I_1 - LI_2 - M_T I_T , \quad [1.41a]$$

$$\phi_2 = (L_2 + L)I_2 - LI_1 + M_T I_T , \quad [1.41b]$$

and

$$\phi_3 = L_T I_T + M_T (I_1 - I_2) . \quad [1.41c]$$

We have assumed that the mutual inductance between loops one and two is just  $L$ , and we will also assume that  $M_T = \sqrt{L_T L}$ . Solving for the currents, we find

$$I_1 = \frac{\begin{vmatrix} \phi_1 & -L & M_T \\ \phi_2 & L_2 + L & -M_T \\ \phi_3 & -M_T & L_T \end{vmatrix}}{\begin{vmatrix} L_1 + L & -L & M_T \\ -L & L_2 + L & -M_T \\ M_T & -M_T & L_T \end{vmatrix}} \quad [1.42]$$

$$= \frac{1}{L_1} \left( \phi_1 - \frac{M_T}{L_T} \phi_3 \right). \quad [1.43]$$

Similarly,

$$I_2 = \frac{1}{L_2} \left( \phi_2 + \frac{M_T}{L_T} \phi_3 \right), \quad [1.44]$$

and

$$I_T = \frac{1}{L_1 L_2 L_T} \left\{ \phi_3 \left[ L_1 L_2 + L(L_1 + L_2) \right] + M_T (\phi_2 L_1 - \phi_1 L_2) \right\}. \quad [1.45]$$

Using the currents  $I_1$  and  $I_2$  we can write the equations of motion for the proof masses,

$$m\ddot{x}_1 + k_1 x_1 = \frac{1}{2d_1 L_1} \left( \phi_1 - \frac{M_T}{L_T} \phi_3 \right)^2, \quad [1.46a]$$

and

$$m\ddot{x}_2 + k_2 x_2 = \frac{1}{2d_2 L_2} \left( \phi_2 + \frac{M_T}{L_T} \phi_3 \right)^2. \quad [1.46b]$$

If we expand  $\frac{1}{L_1}$  and  $\frac{1}{L_2}$  we then have

$$m\ddot{x}_1 + k_1 x = \frac{1}{2d_1 L_1^0} \left( \phi_1 - \frac{M_T}{L_T} \phi_3 \right)^2 \left[ 1 - \frac{x_1}{d_1} \right], \quad [1.47a]$$

and

$$m\ddot{x}_2 + k_2 x_2 = \frac{-1}{2d_2 L_2} \left( \phi_2 + \frac{M_T}{L_T} \phi_3 \right)^2 \left[ 1 + \frac{x_2}{d_2} \right]. \quad [1.47b]$$

Hence the proof mass resonant frequencies are given by

$$\omega_1^2 = \frac{k_1}{m} + \frac{\left( \phi_1 - \frac{M_T}{L_T} \phi_3 \right)^2}{2d_1 L_1} , \quad [1.48a]$$

and

$$\omega_2^2 = \frac{k_2}{m} + \frac{\left( \phi_2 + \frac{M_T}{L_T} \phi_3 \right)^2}{2d_2 L_2} . \quad [1.48b]$$

With current in the tuning loops, the electrical springs act in parallel with the mechanical springs. In order to tune the gradiometer the sum of these two spring constants must be equal for the two proof masses. There are two levels of adjustment available. By storing different  $\phi_1$  and  $\phi_2$  the two suspensions can be roughly matched, then  $\phi_3$  can be adjusted for a more accurate match. When current is stored in the readout loop the accelerometers are coupled and the normal modes of the system split into a mode which is primarily differential motion whose frequency increases with readout current as in figure 1.4, and a mode which is primarily equal motion of the masses. But the tuning problem remains the same. In order to make the gradiometer insensitive to common forces on the proof masses, each proof mass must have the same spring constant between itself and the case of the instrument, so tuning is accomplished in the same way.

Detection of the common mode is carried out with a circuit quite similar to the fine tuning loop. Let us consider the circuit consisting of the two tuning loops and the loop which couples to the SQUID, ignoring the fine tuning loop since currents stored in this loop are small. In this case the equations of motion are very similar to [1.41],

$$\phi_1 = (L_1 + L)I_1 - LI_2 - M_s I_s, \quad [1.49a]$$

$$\phi_2 = (L_2 + L)I_2 - LI_1 + M_s I_s, \quad [1.49b]$$

and

$$\phi_s = (L_3 + L_4)I_s + M_s (I_1 - I_2) \quad [1.49c]$$

where  $M_s = \sqrt{L_3 L}$ . The equilibrium value of  $I_s$  is kept at zero with a heat switch. Solving for  $I_s$  we find

$$I_s = \frac{1}{(L_3 + L_4)L_1 L_2} \left\{ \phi_s [L_1 L_2 + L(L_1 + L_2)] + M_s (\phi_2 L_1 - \phi_1 L_2) \right\}. \quad [1.50]$$

Now in ideal circumstances the balanced gradiometer would have  $\phi_s = 0$ ,  $\phi_1 = \phi_2$ ,  $L_1^0 = L_2^0$ , and  $d_1 = d_2$ . Then  $I_s$  is reduced to

$$I_s = \frac{M_s \phi_1}{(L_3 + L_4)L_1^0} \frac{(x_1 + x_2)}{d}, \quad [1.51]$$

to lowest order in  $x_1/d_1$  and  $x_2/d_2$ . In the ideal case  $I_s$  responds only to common mode motion of the proof masses. In practice  $\phi_1 \neq \phi_2$ ,  $d_1 \neq d_2$ , and  $L_1^0 \neq L_2^0$  so  $I_s$  does couple to differential motion. This is not really a problem because common mode motion is much larger than the differential motion, and the signal from the differential SQUID can be used to identify that part of the signal from the common mode SQUID corresponding to differential motion.

The common mode readout circuit was included in the instrument because in the future we will use its output in a feedback loop to stabilize the positions of the proof masses. The feedback signal will go to the outer

coils in figure 1.9. This feedback loop will reduce coupling of vibration to the differential readout due to nonlinearity of the support springs.

### 1.6 Feedback Damping of the Differential Mode

The high Q of the differential mode is a disadvantage for several reasons. It causes poor transient behavior since the system rings, and the large signal at resonance taxes the slew rate of the SQUID detector. When the slew rate of the SQUID is exceeded, it unlocks and information at low frequencies is lost. Consequently, it is important to be able to damp this mode. The most accessible point at which to insert damping is in the loop between the SQUID and the coupling transformer as shown in figure 1.13. First we analyze a circuit which uses a real resistance R in the SQUID input loop to cause loss and damp the differential mode. Then a simple feedback circuit which synthesizes this resistance is described.

The equations of motion for this system are

$$m \ddot{\xi} + k \xi = \frac{L_1^0}{d} [I^2 - I_0^2] \quad , \quad [1.52a]$$

$$\phi_1 = (L_1 + L_2)I - Mj = (L_1^0 + L_2)I_0 \quad , \quad [1.52b]$$

and

$$R_j = (L_3 + L_4) \frac{dj}{dt} - M \frac{dI}{dt} \quad . \quad [1.52c]$$

where the symbols are those used in section 1.1, and a resistance R has been included as shown in figure 1.13. To solve for the frequency we assume that  $\xi = \xi_0 e^{i\omega t}$ ,  $I = I_0 + I' e^{i\omega t}$ , and  $j = j' t^{i\omega t}$ . Then to first order in  $\xi_0$ ,  $I'$ , and  $j'$  we have

$$(-\omega^2 + \omega_0^2) \xi_0 = \frac{2L_1^0 I_0 I'}{dm} \quad , \quad [1.53a]$$

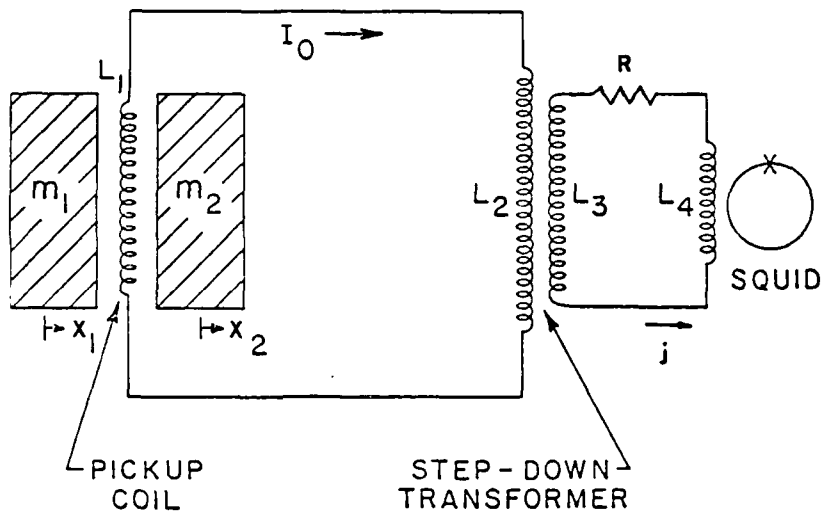


Figure 1.13 Readout Circuit with Resistive Damping

$$(L_1^o + L)I' + \frac{\xi_o L_1^o I_o}{d} - Mj' = 0, \quad [1.53b]$$

and

$$(L_3 + L_4)i\omega j' - i\omega MI' = Rj' \quad [1.53c]$$

Where  $\omega_o^2 = k/m$ .

Setting the determinant

$$\begin{vmatrix} \omega_o^2 - \omega^2 & \frac{-2L_1^o I_o}{md} & 0 \\ \frac{L_1^o I_o}{d} & L_1^o + L_2 & -M \\ 0 & i\omega M & R - i\omega(L_3 + L_4) \end{vmatrix} = 0, \quad [1.54]$$

gives the characteristic equation for  $\omega$ ,

$$i\omega^3 \frac{-\omega^2 R(L_1^o + L_2)}{D} - i\omega \left\{ \omega_o^2 + \frac{2L_1^o I_o^2 (L_3 + L_4)}{m d^2 D} \right\} + \frac{R}{D} \left[ (L_1^o + L_2) \omega_o^2 + 2L_1^o I_o^2 \right] = 0 \quad [1.55]$$

Where  $D = (L_1^o + L)(L_3 + L_4) - M^2$ . Now let

$$\omega_1^2 = \omega_o^2 + \frac{2L_1^o I_o^2}{md^2} \frac{L_1^o (L_3 + L_4)}{D}, \quad [1.56]$$

and

$$\omega_2^2 = \omega_o^2 + \frac{2L_1^o I_o^2}{md^2} \frac{L_1^o}{(L_1^o + L_2)}, \quad [1.57]$$



and

$$\omega_3 = \frac{R(L_1^0 + L_2)}{D} \quad [1.58]$$

Then

$$i\omega^3 - \omega^2\omega_3 - i\omega_1^2 + \omega_3\omega_2^2 = 0 \quad [1.59]$$

The characteristic equation is now a cubic since there is an additional real solution which represents current  $j$  decaying through  $R$  without oscillations in  $\xi$ . The equation is easily solved in two limits. If  $\omega_3 \rightarrow 0$  then  $\omega^2 = \omega_1^2$ , which is the result of section 1.2. If  $\omega_3 \rightarrow \infty$  we have  $\omega^2 = \omega_2^2$ . This is the frequency we would measure if the secondary loop of the transformer were removed. In both cases there is no damping. As  $R$  is varied between 0 and  $\infty$  the frequency moves between these two points, and the  $Q$  falls to some finite value and returns to infinity.

We can parameterize [1.59] if we let  $x = i\omega/\omega_1$ ,  $A = \omega_3/\omega_1$ , and  $B = \omega_2/\omega_1$ . Then

$$x^3 - x^2A + x - AB^2 = 0 \quad [1.60]$$

If  $x_0$  is a solution, the  $Q$  is then given by

$$Q = \frac{I_m(x_0)}{2\text{Re}(x_0)} \quad [1.61]$$

Equation [1.60] is a cubic and can therefore be solved exactly for the  $Q$  for any  $A$  and  $B$ . Figure 1.14 shows the variation of the  $Q$  with  $A$  for a given value of  $B$  (0.98). Figure 1.15 shows how the minimum  $Q$  varies with  $B$ . The result is approximately that

$$Q_{\min} = \left[1 - \omega_2/\omega_1\right]^{-1} \quad [1.62]$$

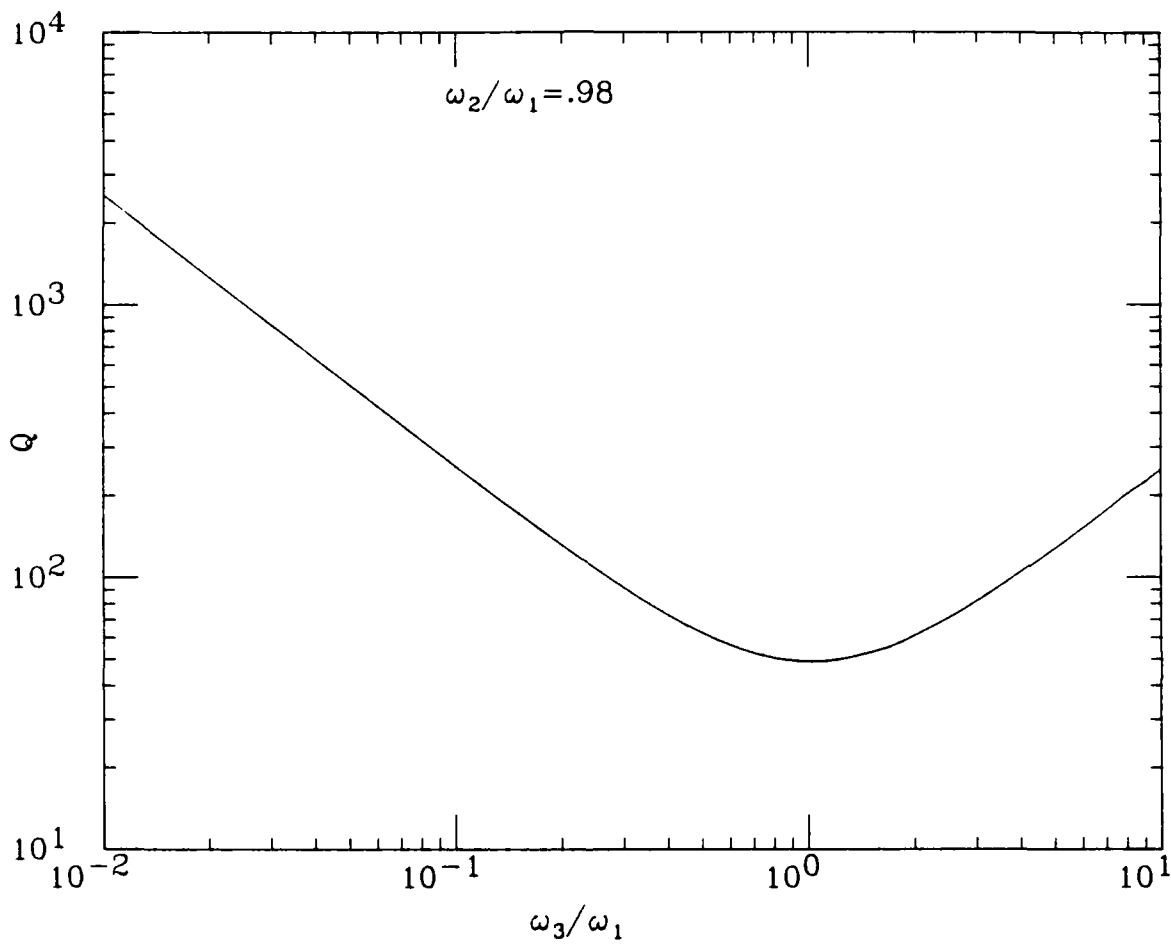


Figure 1.14 Q variation with resistance.

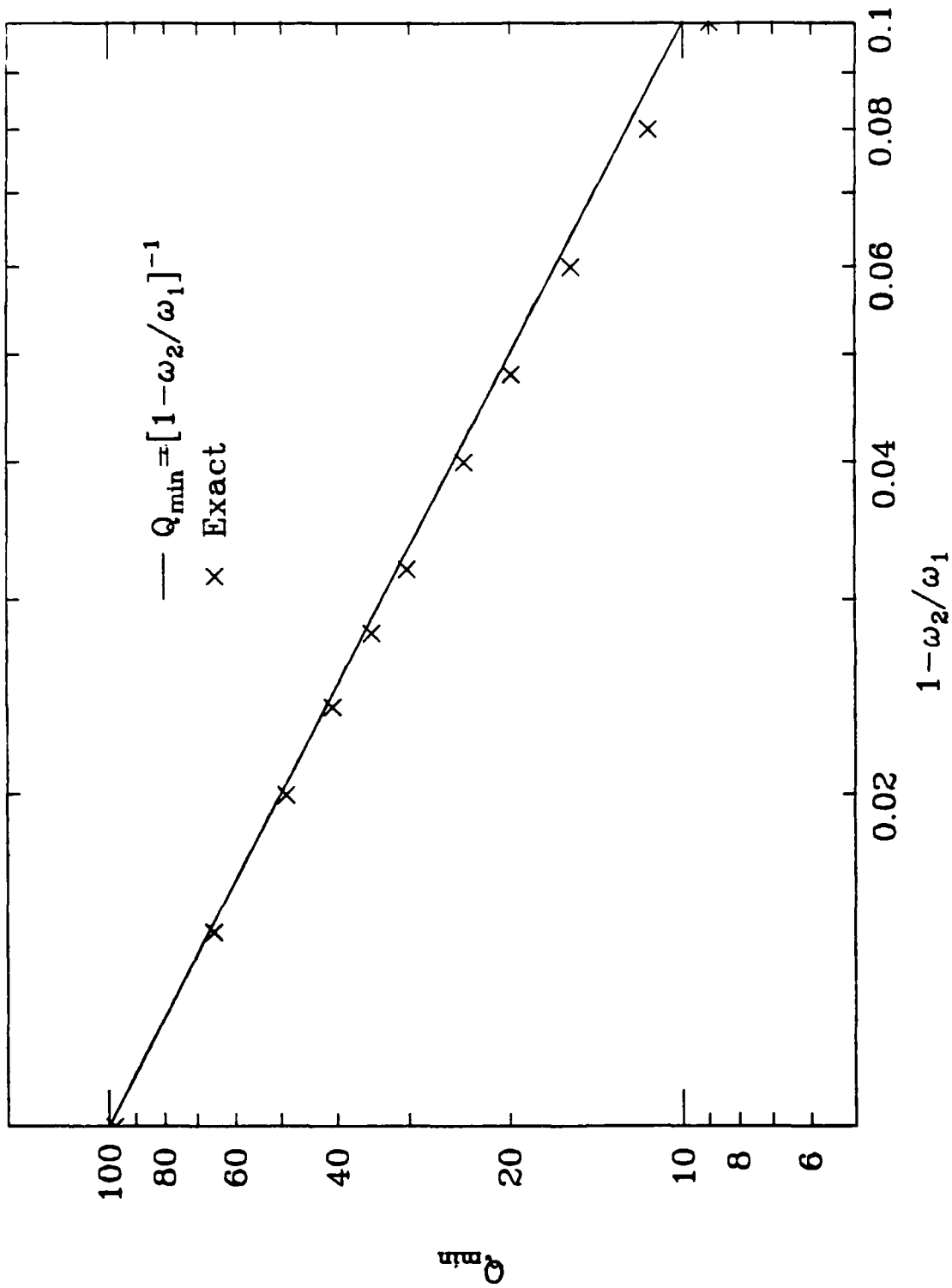


Figure 1.15 Minimum Q as a Function of  $\omega_2/\omega_1$

and

$$\frac{\omega_3}{\omega_1} = 1 + \frac{1}{2} \left( \frac{\omega_1 - \omega_2}{\omega_1} \right) \quad [1.63]$$

gives the minimum Q.

This circuit cannot be used in practice since the real solution implies that there is a low frequency cutoff in the circuit response, and the addition of a real resistor would increase the noise in the circuit. However, the equivalent of a resistor can be built using feedback techniques. This scheme is shown in figure 1.16. It consists of putting the output of the SQUID through a filtering and phase shifting network  $H(\omega)$ , and then feeding back a current proportional to the resulting signal to a transformer in front of the SQUID. This technique was demonstrated by Kai Wang [Wang 1979], who used this circuit to reduce the Q of a superconducting accelerometer.

The transfer function  $H(\omega)$  consists of a bandpass filter and phase shifter. The SQUID control unit converts the SQUID input current  $j$  to a voltage with a conversion factor  $G_s$ . This voltage is multiplied by  $H(\omega)$ , and converted to a feedback current  $i_f$  in the voltage to current converter with a scale factor  $G_v$ . So

$$i_f = G_v H(\omega) G_s j' e^{i\omega t} \quad [1.64]$$

The voltage across the feedback transformer is

$$\begin{aligned} v_f &= -M_f \frac{di_f}{dt} \\ &= -M_f G_v G_s i\omega H(\omega) j' \end{aligned} \quad [1.65]$$

So the effective resistance is just

$$R_{\text{eff}} = \frac{v_f}{j'} = -M_f G_v G_s i\omega H(\omega). \quad [1.66]$$

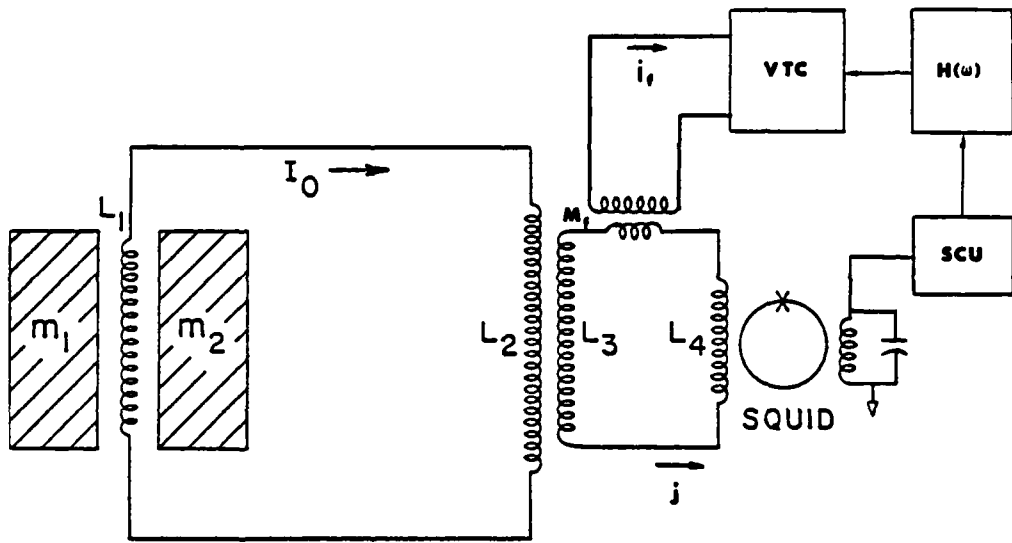


Figure 1.16 Readout Circuit with Feedback Damping

The bandpass filter in  $H(\omega)$  has zero phase shift at resonance so an additional phase shift of  $90^\circ$  is needed to make  $R_{\text{eff}}$  real and positive.

So if

$$H(\omega) = \frac{-\omega_f \omega}{\left[ \omega_f^2 + \frac{i\omega_f \omega}{Q_f} - \omega^2 \right]}, \quad [1.67]$$

then  $R_{\text{eff}}$  becomes

$$R_{\text{eff}} = \frac{M_f G_v G_s i \omega_f \omega^2}{\left[ \omega_f^2 + i\omega_f \omega / Q_f - \omega^2 \right]}. \quad [1.68]$$

In practice  $\omega_f$  is set at the resonant frequency of the mode to be damped and  $R_{\text{eff}}$  reduces to

$$R_{\text{eff}} = M_f G_v G_s Q_f \omega_f. \quad [1.69]$$

at the feedback frequency. By adjusting  $G_v$  and  $Q_f$ ,  $R_{\text{eff}}$  can be adjusted to reach a minimum  $Q$ .

## CHAPTER 2

### Experimental Evaluation of the Superconducting Gravity Gradiometer

#### 2.1 Balancing and Normal Modes

The first tests which will be described involve the tuning of the differential mode, and the balancing of the proof mass spring constants to reject linear accelerations.

Figure 2.1 shows the frequency of the differential modes as a function of current between 3.0 and 6.5 amperes. As the current was reduced to values below 3 amperes the differential mode disappeared. This seems to be due to an interference between the two proof masses which is eliminated as the proof masses are pushed apart. It might be some small piece of material which connects the two masses but loses contact with one of them as current is stored. As current is stored in the differential pickup coil, the common mode frequency remains fixed at 59.6 Hz.

The data of figure 2.1 can be fitted to equation [1.32] to give values for the frequency of the differential mode with  $I_0 = 0$  and a parameter in equation [1.32],

$$\gamma = \frac{L_1^2 (L_3 + L_4)}{(2\pi)^2 m L_0^2 d^2} \quad [2.1]$$

A fit of the data to equation [1.37] gives a frequency

$$f_0 \cong 59 \text{ Hz} ,$$

and

$$\gamma \cong 70 \text{ Hz}^2/\text{A}^2 .$$

As described in section 1.3, the design value for  $f_0$  is 60 Hz so the data are consistent with the theory for the folded cantilever springs. The

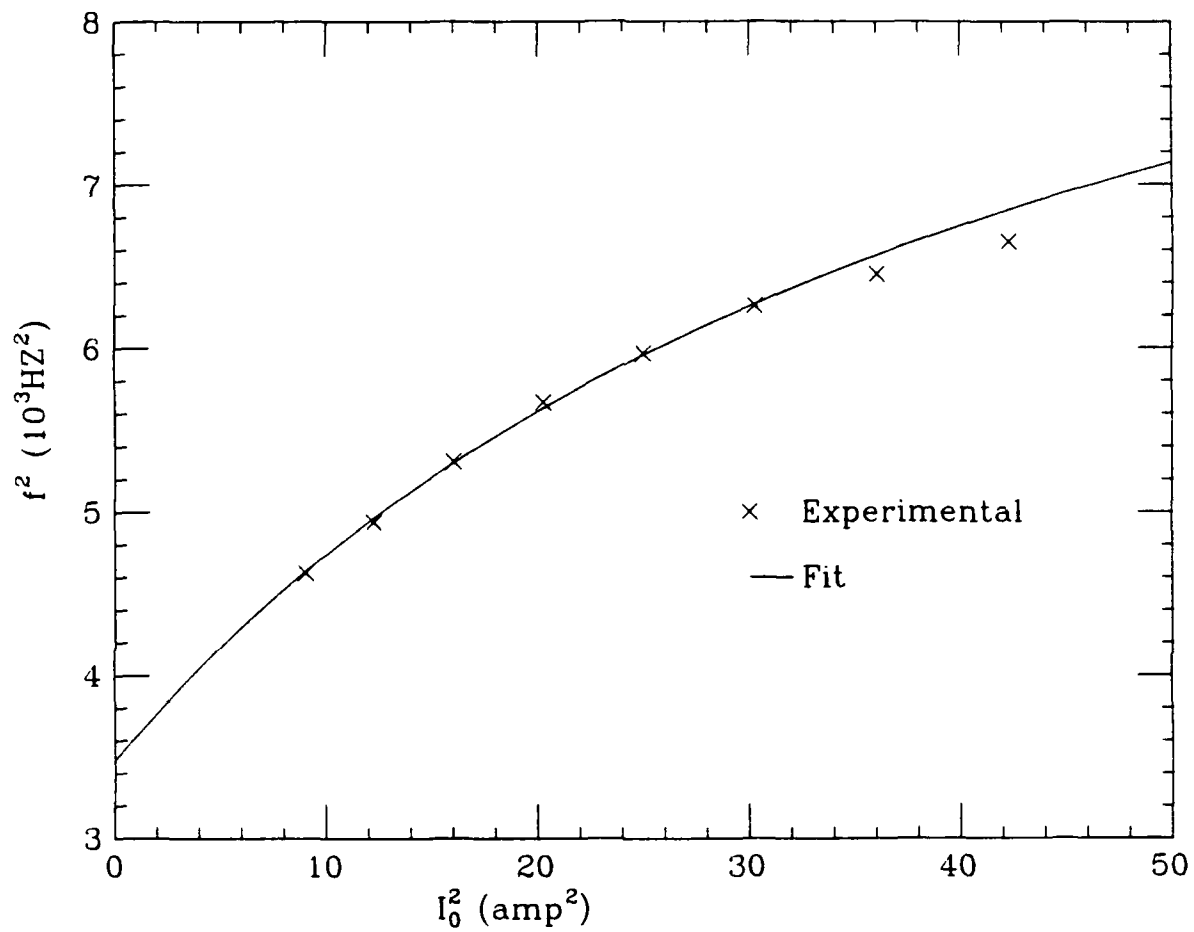


Figure 2.1 Differential mode frequency shift as a function of persistent current.



observed frequency of the common mode of 59.6 Hz is also consistent. The design values of the parameters for  $\gamma$  are

$$\frac{L_1^0}{d} = .79 \text{ H/m},$$

$$L_3 + L_4 = 9 \times 10^{-6} \text{ H},$$

$$m = 1.07 \text{ kg},$$

and 
$$L_o^2 = 1.8 \times 10^{-9} \text{ H}^2.$$

The value for  $L_o$  assumes that the coupling of the transformer in the readout circuit is unity, so in practice we should expect  $L_o^2$  to be somewhat larger. See equation [1.30]. These numbers give a value

$$\gamma = 74 \text{ Hz}^2/\text{A}^2,$$

so again the experiment is quite consistent with calculated results.

Looking back at equation [1.34], the optimum current is related to  $\gamma$  by

$$I_{op}^2 = \frac{f_o^2}{3\gamma} \quad [2.2]$$

so that the experimental numbers give

$$I_{op} = 4.2 \text{ A} .$$

This current corresponds to a field of 525 gauss or not much more than half of the critical field of 1000 gauss for niobium. This is a consequence of a conservative choice of pickup coil parameters. A smaller coil could have been used, thereby increasing  $I_{op}$  with little loss of sensitivity.

In order to balance the system, the response of the differential SQUID to a mechanical excitation of the gradiometer was measured as a function of currents in the tuning loops described in section 1.5. Mechanical motion

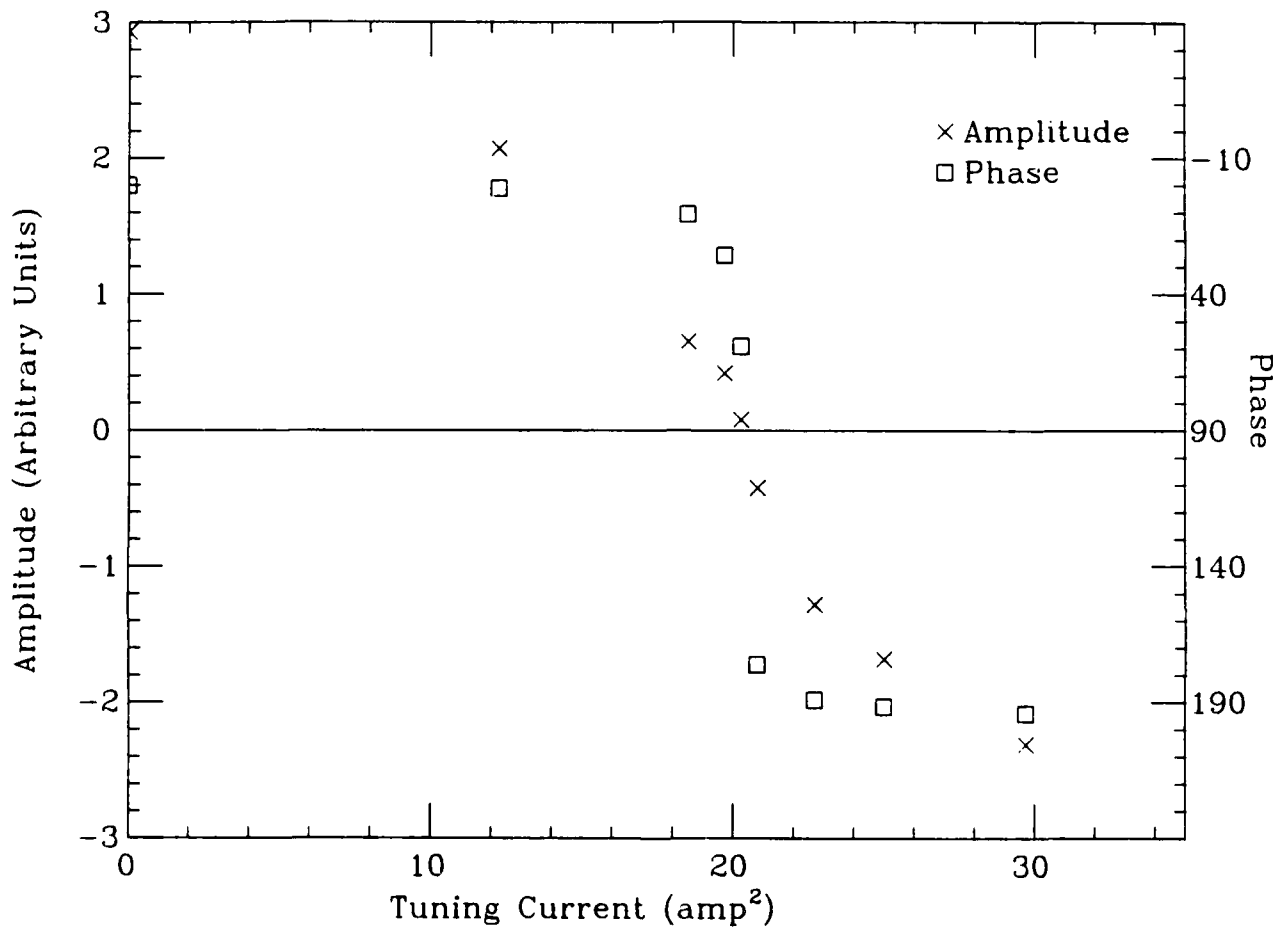


Figure 2.2 Differential error signal as a function of tuning current.

was generated in two ways. The internal PZT actuators described in section 1.4 were driven at 4.0 Hz, and the entire dewar was driven externally at 4.0 Hz using a mechanical shaker. The dewar was hung from the ceiling with latex tubing to provide vibration isolation. This gives a vertical resonant frequency of approximately 1.2 Hz for the dewar so it appears as a free mass when driven at 4 Hz. Figure 2.2 shows the amplitude and phase response of the differential SQUID to a constant drive signal on the PZT as current in one tuning loop is changed. A constant current of 1.0 amp was left in the other loop during the test.

The principle feature of figure 2.2 is that at a specific current the amplitude response passes through zero, and the phase changes by  $180^{\circ}$  through this point. This tuning point is the point at which one normal mode of the coupled proof masses is pure differential motion and the other normal mode is pure common motion. At this point the two proof masses deflect by exactly the same distance under a static load. On either side of the tuning point one proof mass moves more than the other, and there is a differential displacement for a linear acceleration. As the current is moved across the tuning point the stiffer suspension becomes the weaker, and the sign of the response to a common acceleration changes; hence the 180 degree phase shift.

These results prove that the normal mode structure of the instrument is understood, and that the balancing control described in section 1.5 is working. This is essential if we are to make accurate measurements of gravitational gradients.

## 2.2 Scale Factor Calibration and Noise

The most important tests of the gradiometer are the measurement of its scale factor and the detection of an actual gravitational gradient. This section describes such measurements and gives some noise power spectra from which a reasonable assessment of the instrument's present capabilities can be made.

The first calibration makes use of the gradiometer's sensitivity to tilts described by equation [1.14]. If the gradiometer is oriented along the z axis, and is given a tilt of amplitude  $\theta_0$  and frequency  $\omega$  about the x or y axis, a gradient

$$g(t) = \frac{\theta_0^2 \omega^2}{2} \cos 2\omega t . \quad [2.3]$$

results. This is a very attractive situation because the gradient signal can be calculated entirely from measured quantities. It is independent of the baseline of the instrument, and the location of the rotation axis.

The dewar was hung on latex tubing as described in the previous section. The mechanical shaker was attached to the top of the dewar with its driving axis parallel to the gradiometer axis. Since the top of the dewar is about two feet above the center of mass of the hanging dewar, the a.c. force from the shaker applies a torque to the dewar and a small angular motion results. This angular motion is detected with an automatic autocollimator [Klinger 1974] whose beam is reflected from a mirror attached to the section of the cryostat in front of the gradiometer.

Figure 2.3 is a plot of the differential SQUID response at twice the shaker drive frequency versus the autocollimator tilt signal measured at the drive frequency. The SQUID and autocollimator responses were synchronously detected with a PAR 5204 lock-in amplifier. The upper points fit the

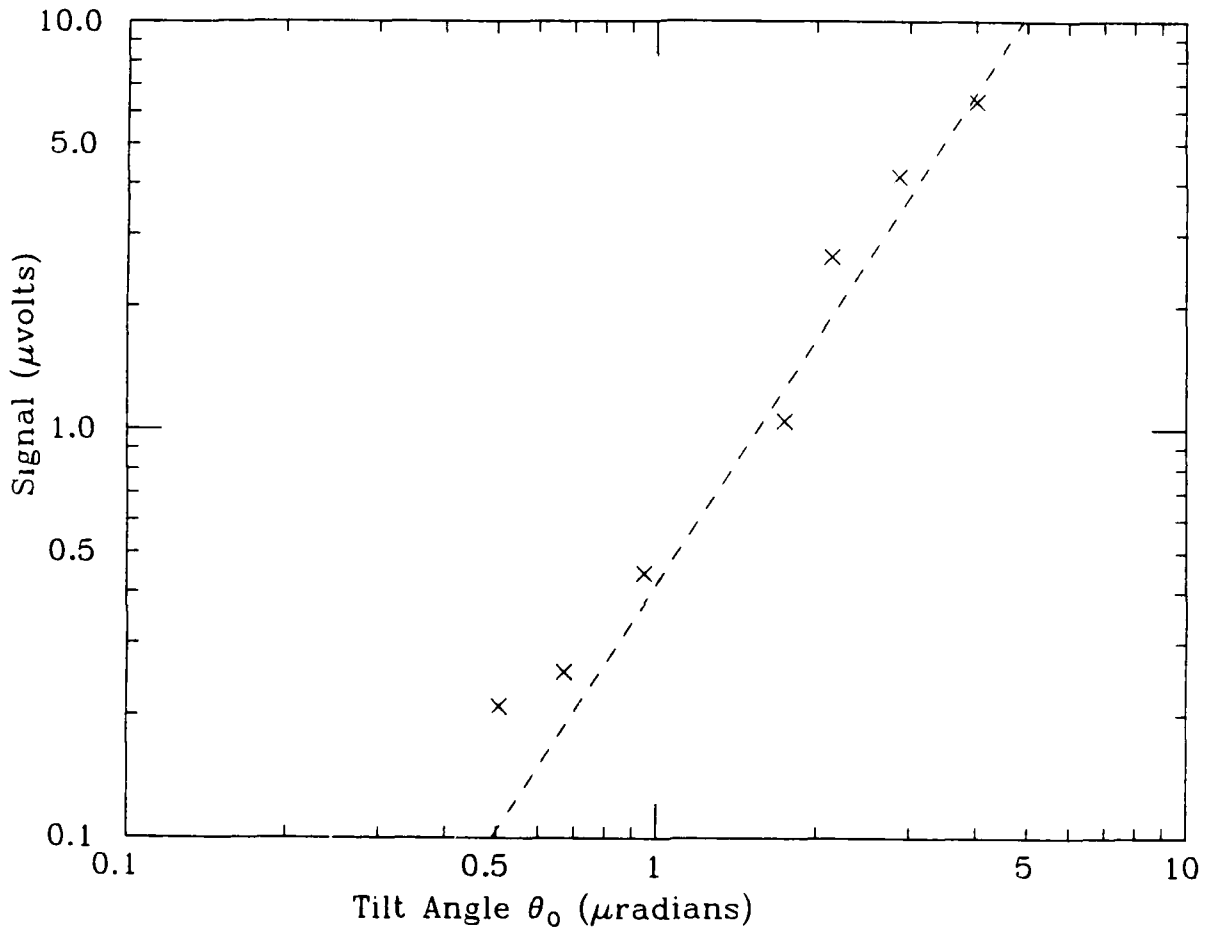


Figure 2.3 Tilt response as a function of tilt amplitude.

expected behavior of a twice frequency signal increasing as the square of the tilt amplitude. This plot gives a scale factor of  $1.2 \pm .15 \mu\text{V}/\text{E}$  with 5.0 A stored in the differential loop and a drive frequency of 4.15 Hz.

Equation [1.33] allows us to predict a scale factor of  $1.46 \mu\text{V}/\text{E}$  using the experimental value of  $\gamma$  from section 2.1, and a baseline of 3.2 cm, giving reasonable agreement with the experimental result.

In order to calibrate the system with a gravitational gradient we have measured the response of the gradiometer to a rotating mass quadrupole. Figure 2.4 shows the layout of this experiment. Two masses are mounted on an aluminum arm a distance  $r$  from the  $z$  axis. This arm rotates in a vertical plane about the  $z$  axis at a frequency  $\omega$ . The gradiometer is positioned with its sensitive axis horizontal, and its center on the  $z$  axis a distance  $R$  from the center of the mass quadrupole. The azimuthal angle is the angle between the  $z$  axis and the gradiometer axis.

To calculate the gravity gradients, note that the displacement vectors between  $M_1$  and  $p_1$  and  $M_2$  and  $p_1$  are

$$\vec{d}_1 = (h \sin \theta - r \cos \omega t) \hat{i} + r \sin \omega t \hat{j} - (R + h \cos \theta) \hat{k} \quad , \quad [2.4a]$$

and

$$\vec{d}_2 = (h \sin \theta + r \cos \omega t) \hat{i} - r \sin \omega t \hat{j} - (R + h \cos \theta) \hat{k} \quad . \quad [2.4b]$$

The gravitational acceleration at  $p_1$  is

$$\vec{a}_1(t) = GM \left\{ \frac{\vec{d}_1}{|\vec{d}_1|^3} + \frac{\vec{d}_2}{|\vec{d}_2|^3} \right\} \quad . \quad [2.5]$$

To find the gradient we project this onto the unit vector in the direction of the gradiometer axis and take the derivative with respect to h. So

$$g(t) = \frac{d}{dh} \left[ \vec{a}_1(t) \cdot (\cos\theta \hat{k} - \sin\theta \hat{i}) \right]. \quad [2.6]$$

Taking the dot product

$$g(t) = GM \frac{d}{dh} \left\{ \frac{-\sin\theta(h \sin\theta + r \cos\omega t) + \cos\theta(R + h \cos\theta)}{[(h \sin\theta + r \cos\omega t)^2 + r^2 \sin^2\omega t + (R + h \cos\theta)^2]^{3/2}} \right. \\ \left. - \frac{\sin\theta(h \sin\theta - r \cos\omega t) + \cos\theta(R + h \cos\theta)}{[(h \sin\theta - r \cos\omega t)^2 + r^2 \sin^2\omega t + (R + h \cos\theta)^2]^{3/2}} \right\} \quad [2.7]$$

The experiment whose description follows is sensitive only to time varying gradients so in taking the derivative we will drop terms with no time dependence. This leaves

$$g(t) = 3 GM \left\{ \frac{\sin^2\theta (h \sin\theta + r \cos\omega t)^2 + \cos^2\theta (R + h \cos\theta)^2}{[(h \sin\theta + r \cos\omega t)^2 + r^2 \sin^2\omega t + (R + h \cos\theta)^2]^{5/2}} \right. \\ \left. + \frac{\sin^2\theta (h \sin\theta - r \cos\omega t)^2 + \cos^2\theta (R + h \cos\theta)^2}{[(h \sin\theta - r \cos\omega t)^2 + r^2 \sin^2\omega t + (R + h \cos\theta)^2]^{5/2}} \right\}. \quad [2.8]$$

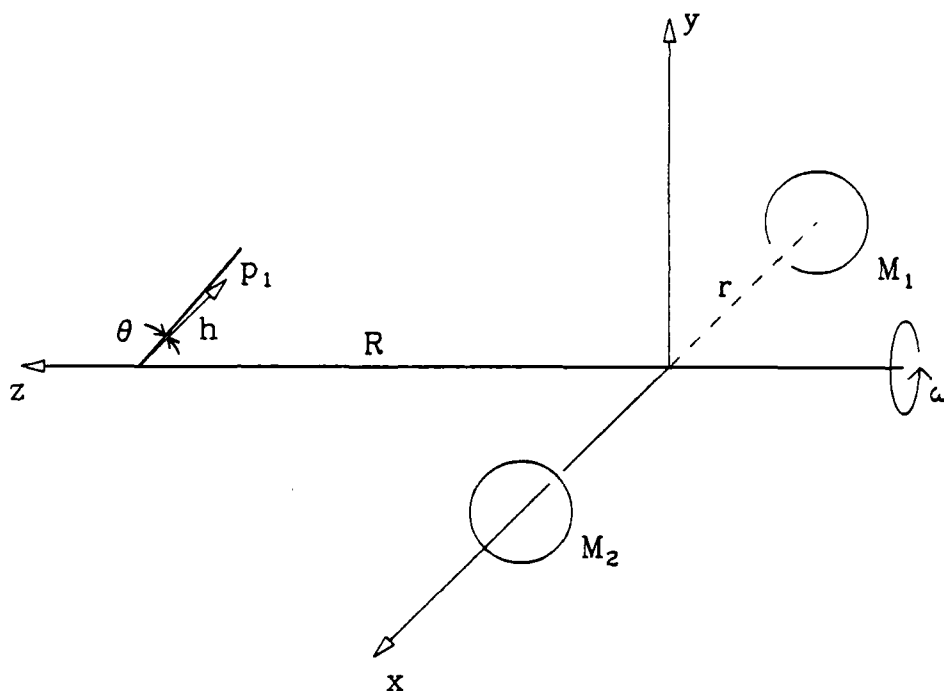


Figure 2.4 Coordinates for the RMQ experiment.



Finally we set  $h = 0$  and again drop constant terms. This leaves

$$g(t) = \frac{3GMr^2 \sin^2 \theta \cos 2\omega t}{[r^2 + R^2]^{5/2}} \quad [2.9]$$

We find that the only time dependent term is at twice the mass quadrupole spin frequency. This is desirable since most of the mechanical noise produced by the rotor is at the spin frequency. The signal also has a clear signature in that rotating the gradiometer about the vertical gives a  $\sin^2$  modulation of the signal. Unfortunately, the dependence on  $R$  is a disadvantage. For  $R > r$  the signal decreases like  $R^{-5}$  so the rotor has to be rather close to the instrument and relative gradient error is five times the relative error in  $R$ . For these reasons the rotating mass quadrupole is not very useful for determining the scale factor of the instrument, but it is useful as a demonstration that the gradiometer is actually able to see a gravitational gradient.

Figure 2.5 is a photograph of the mass quadrupole. The masses consist of four lead bricks mounted with their centers of mass 35.6 cm apart. For this experiment the gradiometer dewar was hung in the corner of an acoustically insulated room from the usual latex tubing. The mass quadrupole was positioned just on the other side of the wall. With this arrangement the dewar could be rotated to change  $\theta$ . The measured values of the parameters in equation [2.9] were

$$M = 43 \text{ kg,}$$

$$R = .58 \text{ m,}$$

$$r = .18 \text{ m,}$$

and  $\omega = 20.1 \text{ rad/sec.}$

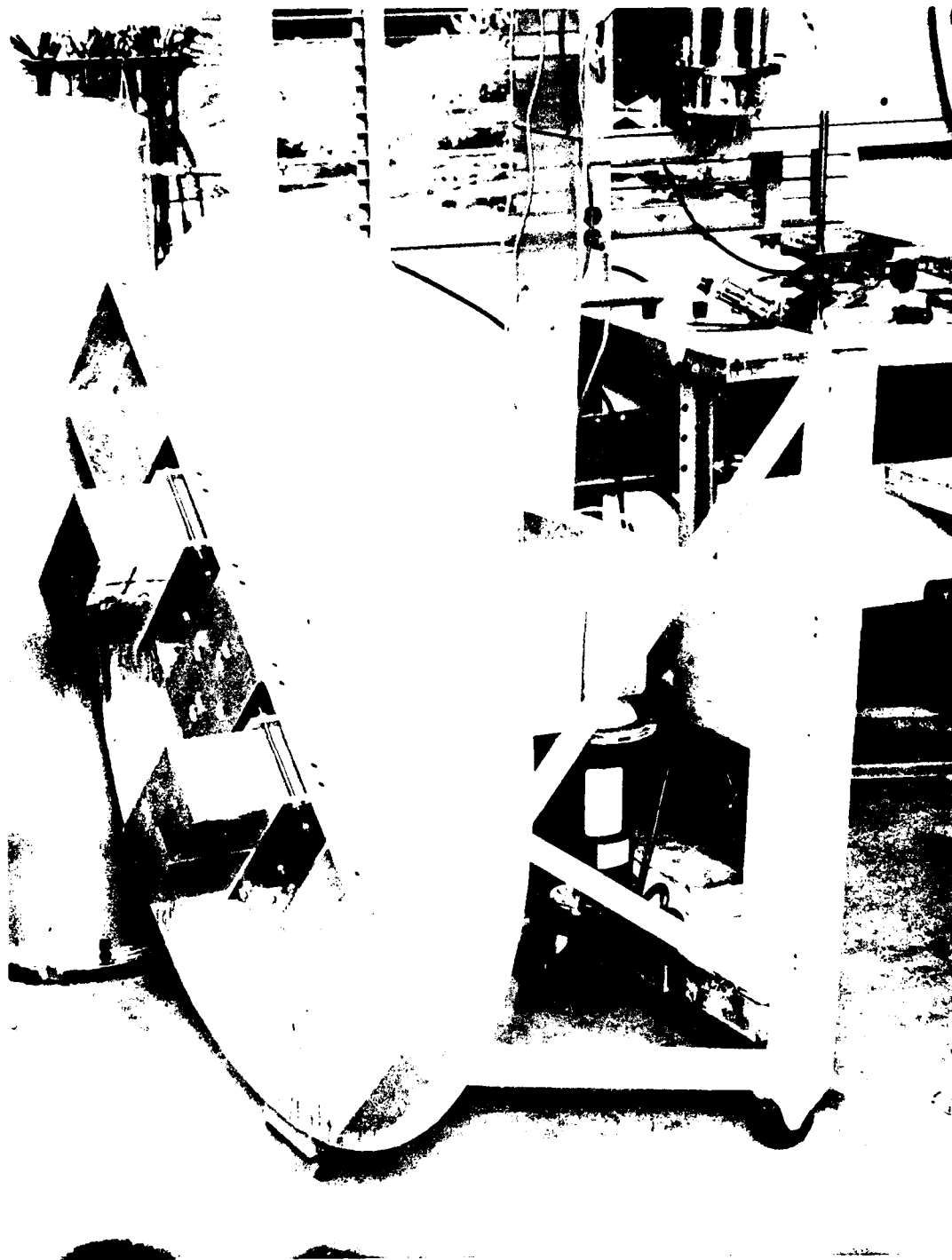


Figure 2.5 The Rotating Mass Quadrupole

From these we calculate

$$\frac{3GMr^2}{[R^2 + r^2]^{5/2}} = 3.4 E.$$

The mass quadrupole was rotated at 3.2 Hz, and the signal at 6.4 Hz was synchronously detected with a lock-in amplifier. The lock-in reference was provided by a photodiode-phototransistor switch on the frame of the mass quadrupole. Figure 2.6 is a plot of the gradiometer signal versus azimuthal angle  $\theta$ . The solid curve is a fit to the data assuming a  $\sin^2\theta$  dependence on azimuthal angle. The data is somewhat noisy because electrical noise from the mass quadrupole drive system causes the SQUID to unlock frequently. When the SQUID unlocks its output changes by a multiple of 20 mV causing the lock-in to overload. In order to collect data a short averaging time had to be used. The time constant of the lock-in amplifier was set at 10 sec for the data in figure 2.6. Using the data from the previous calibration gives

$$\frac{3GMr^2}{[R^2 + r^2]^{5/2}} \approx 2.5 E .$$

This is significantly less than the calculated value, but a 1 cm error in measuring R gives an error of about 10% in the gradient. In addition to this error, finite size effects can also reduce the observed signals. The fact that the response varies like  $\sin^2\theta$  strongly suggests that it is gravitational rather than seismic or acoustic. We also verified that increasing R by 30 cm eliminated the signal with the averaging time used above.

Figure 2.7 shows the gradiometer output noise versus frequency between zero and ten hertz. The large peak at 1.2 Hz is the vertical resonance of the suspension. Above 2.5 Hz the noise floor is at  $3.3E/\sqrt{\text{Hz}}$ , although there are several peaks where the noise is more than  $40E/\sqrt{\text{Hz}}$ . Under the suspension resonance the noise climbs to about  $100E/\sqrt{\text{Hz}}$ . Two intrinsic

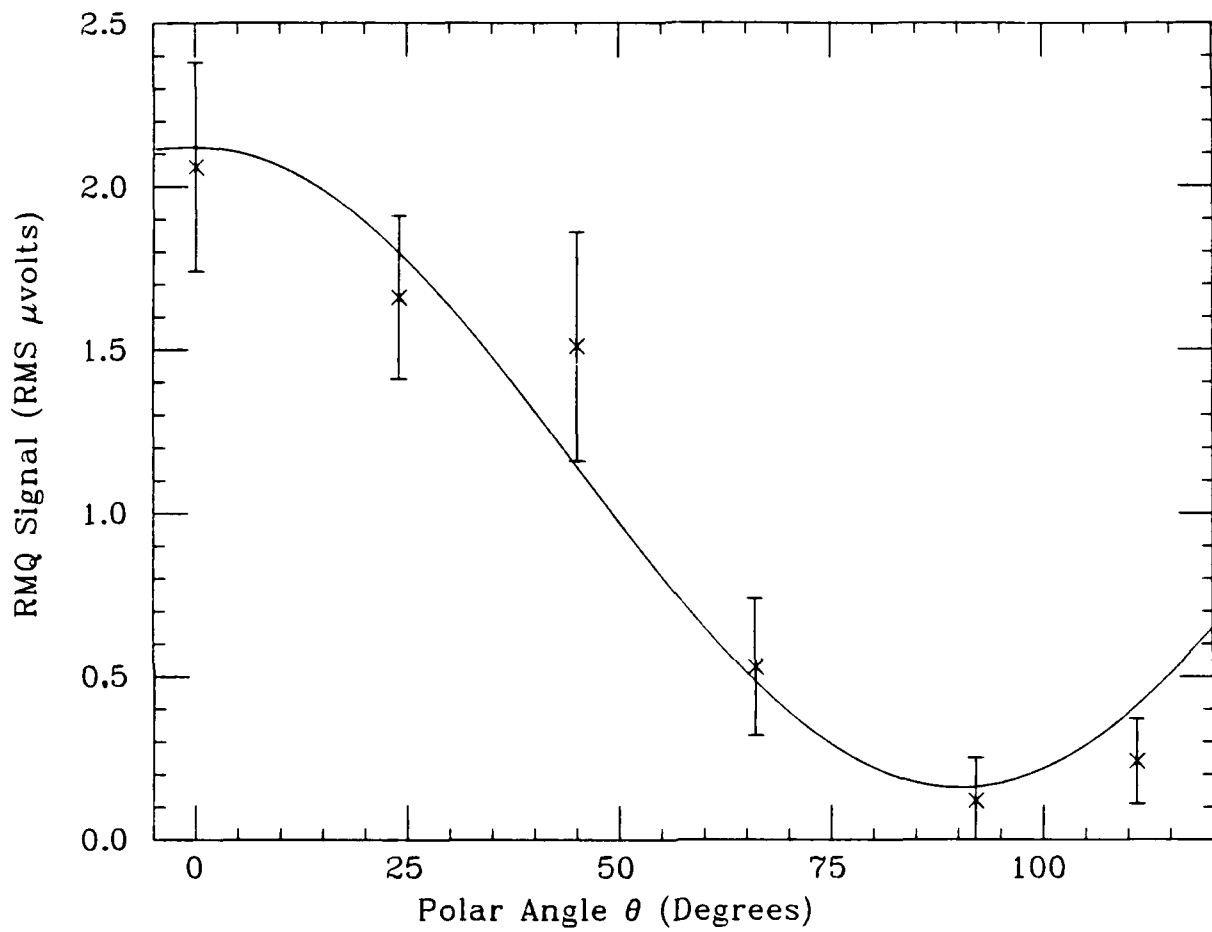


Figure 2.6 Gradiometer signal from the rotating mass quadrupole.

sources of noise are readily identified. The noise performance of the commercial SQUID used in the differential readout was measured separately before we installed it in the readout circuit. Between zero and ten hertz the output noise was  $1.1 \mu\text{V}/\sqrt{\text{Hz}}$  or the equivalent of  $.92 \text{ E}/\sqrt{\text{Hz}}$  with 5.0 A in the readout loop. The measured performance is only 3.6 times this above 2 Hz. So between 2 Hz and 10 Hz the instrument's performance is approaching one of the intrinsic limits of the system.

The other intrinsic noise source is the Brownian noise in the differential mode due to the dissipation in the system. When the system is balanced the differential mode is just a harmonic oscillator subject to a fluctuating force with power spectral density

$$S_f(\omega) = 4KTH \quad . \quad [2.10]$$

according to Nyquist's theorem. Where  $k$  is Boltzman's constant,  $T$  is the temperature, and  $H$  is the mass divided by the energy decay time of the mode. The measured energy decay time of the differential mode with 5.0 A stored was 6.3 seconds. The spectral density of gradient fluctuations corresponding to  $S_f(\omega)$  is given by

$$S_g = \frac{\sqrt{S_f(\omega)}}{Mb} \quad , \quad [2.11]$$

at frequencies well below the resonant frequency of the differential mode.

At  $T = 4.2^\circ \text{ K}$  this gives

$$S_g = 0.18 \text{ E}/\sqrt{\text{Hz}} .$$

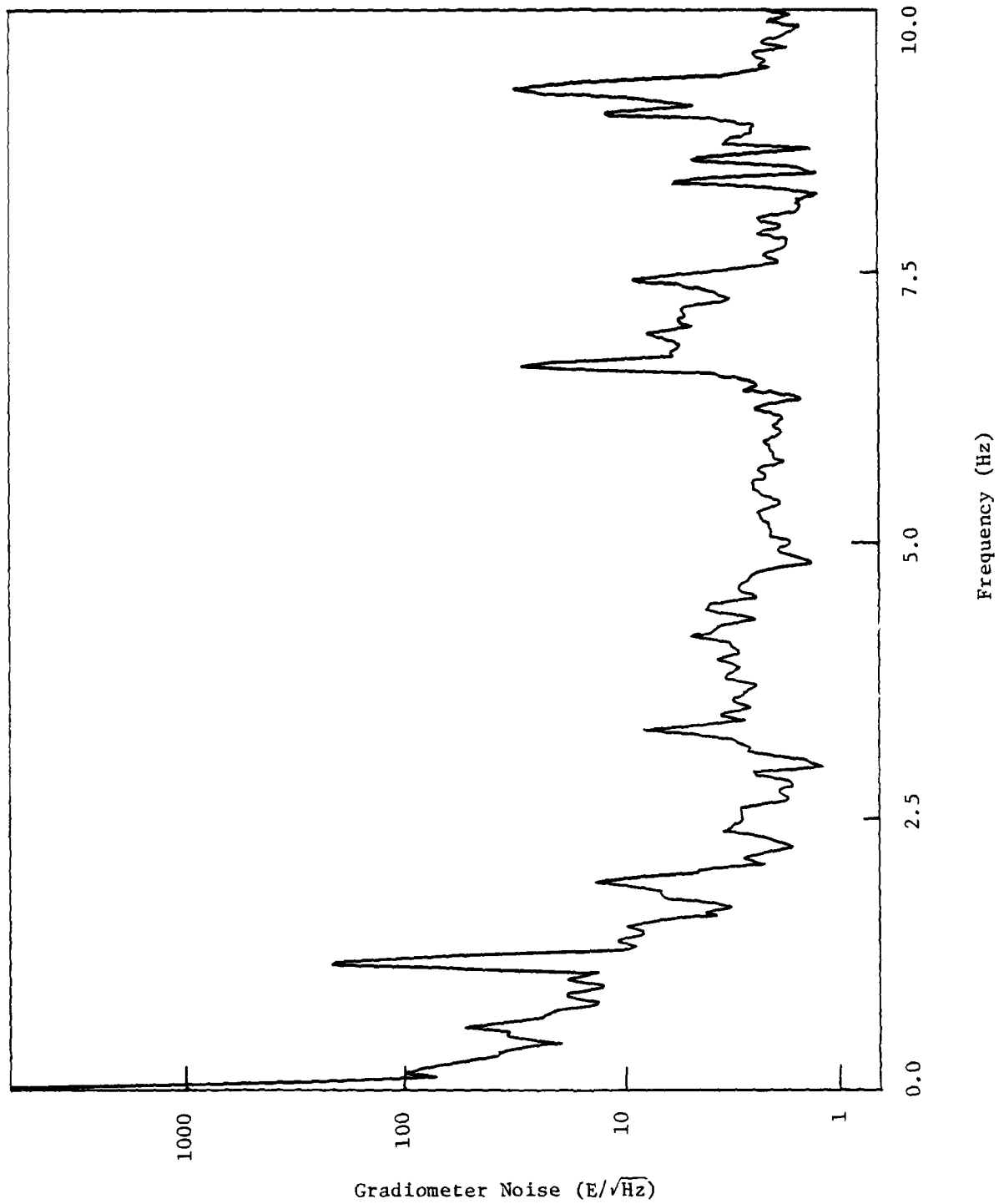


Figure 2.7 Gradiometer Noise from 0 to 10 Hz

This is nearly 20 times less than the observed noise floor of the instrument and is six times less than the limit of the SQUID.

Although the noise performance above 2 Hz is quite close to expectations, the noise amplitude between 0 and 1 Hz remains a serious problem. In order to carry out the inverse square law test we need to measure gradients at the center of a cylindrical shell whose central horizontal gradient is 6 E. To complete a highly sensitive test we would like to measure this to an accuracy like .5%. This requires the ability to detect  $3 \times 10^{-2}$  E, a signal well below the noise level. However, there are several improvements which may reduce the noise at low frequencies. In section 2.4 we will discuss the sensitivity of the instrument to thermal fluctuations. It turns out that this sensitivity is quite high, and the implementation of more stable thermal control in the instrument may improve the low frequency noise performance. We will also complete a feedback loop to stabilize the positions of the proof masses, and this may reduce low frequency noise caused by nonlinearity in the suspension. Such nonlinearity may cause rectification of high frequency signals, which would show up as an increased noise level near zero frequency.

### 2.3 Feedback Damping

During the calibration experiments described in section 2.2, feedback damping was used to greatly reduce the signal at the differential mode frequency. This was essential because excitation of the differential mode would cause the SQUID to unlock frequently if the mode was left undamped.

Figure 2.8 shows the circuit used to condition the feedback signal. It consists of a bandpass filter with adjustable Q and center frequency, a phase shifter to provide 90 degrees of phase shift at the bandpass center frequency, and a voltage to current converter which provides the feedback

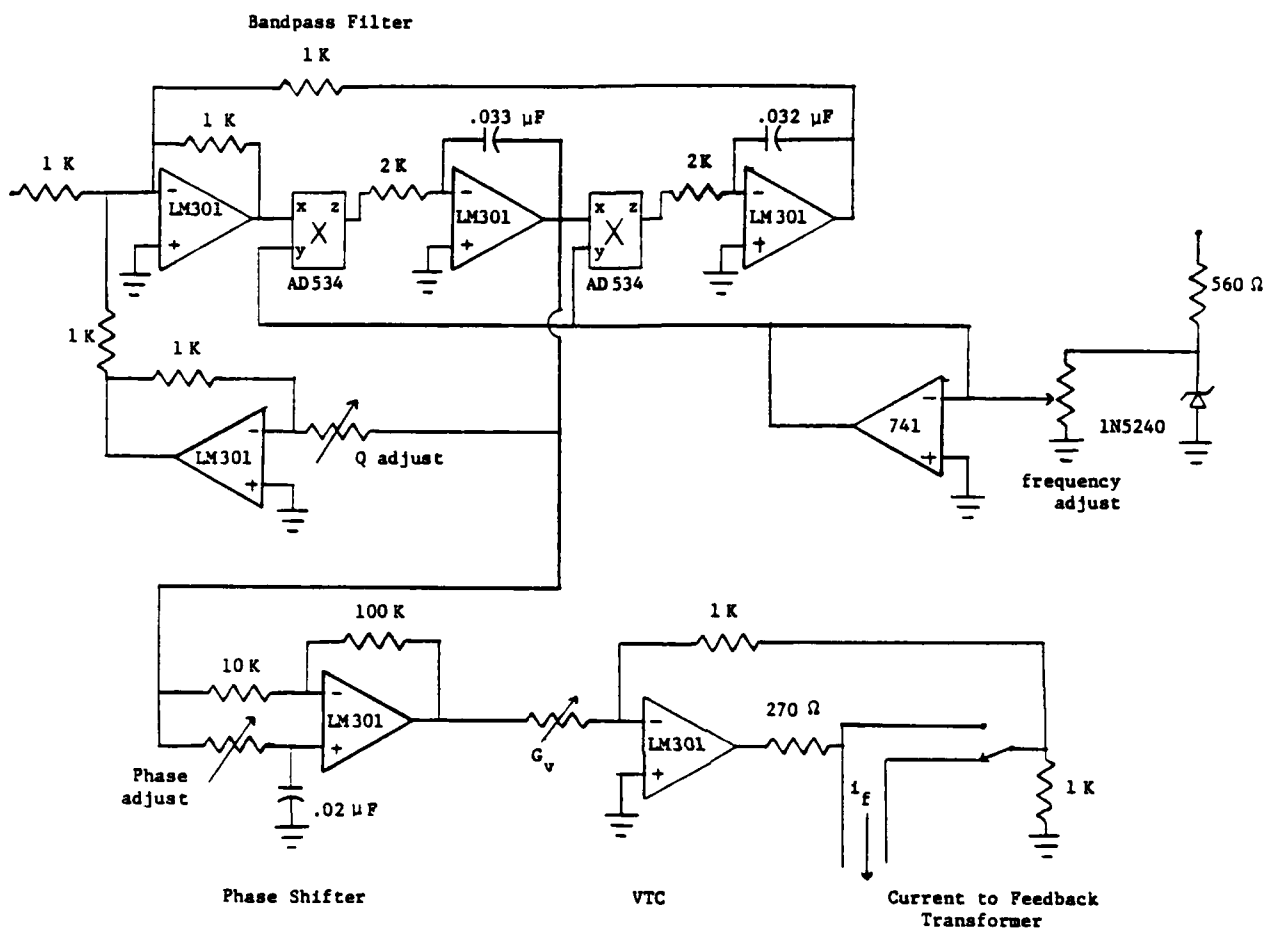


Figure 2.8 Feedback Circuit



current. According to equation [1.62] the minimum  $Q_{\min}$  is approximately

$$Q_{\min} = \left[ 1 - \omega_2/\omega_1 \right]^{-1} . \quad [2.12]$$

$\omega_1$  can be measured directly since it is the normal mode frequency in the absence of damping. We can calculate an expected value for  $\omega_2$  from equation [1.57]. According to [1.56] and [1.57]

$$\omega_2^2 = \omega_0^2 + \frac{D(\omega_1^2 - \omega_0^2)}{(L_1^0 + L_2)(L_3 + L_4)} . \quad [2.13]$$

With 6.0A in the readout loop we had

$$\omega_1 = 505 \text{ rad/sec.}$$

Using the design values for the other parameters

$$D \cong 2700 (\mu\text{H})^2 ,$$

$$(L_1^0 + L_2)(L_3 + L_4) = 4500 (\mu\text{H})^2 ,$$

and

$$\omega_0 = 377 \text{ rad/s} ,$$

we find an expected value for  $\omega_2$  of

$$\omega_2 \cong 458 \text{ rad/s.}$$

According to [2.12] this gives  $Q_{\min} \cong 11$ . Using [1.63] we find the  $Q_{\min}$  should be reached at

$$\frac{R_{\text{eff}}(L_1^0 + L_2)}{D} = \omega_1 + \frac{1}{2} (\omega_1 - \omega_2) , \quad [2.14]$$

or

$$R_{\text{eff}} = 3.1 \times 10^{-3} \Omega .$$

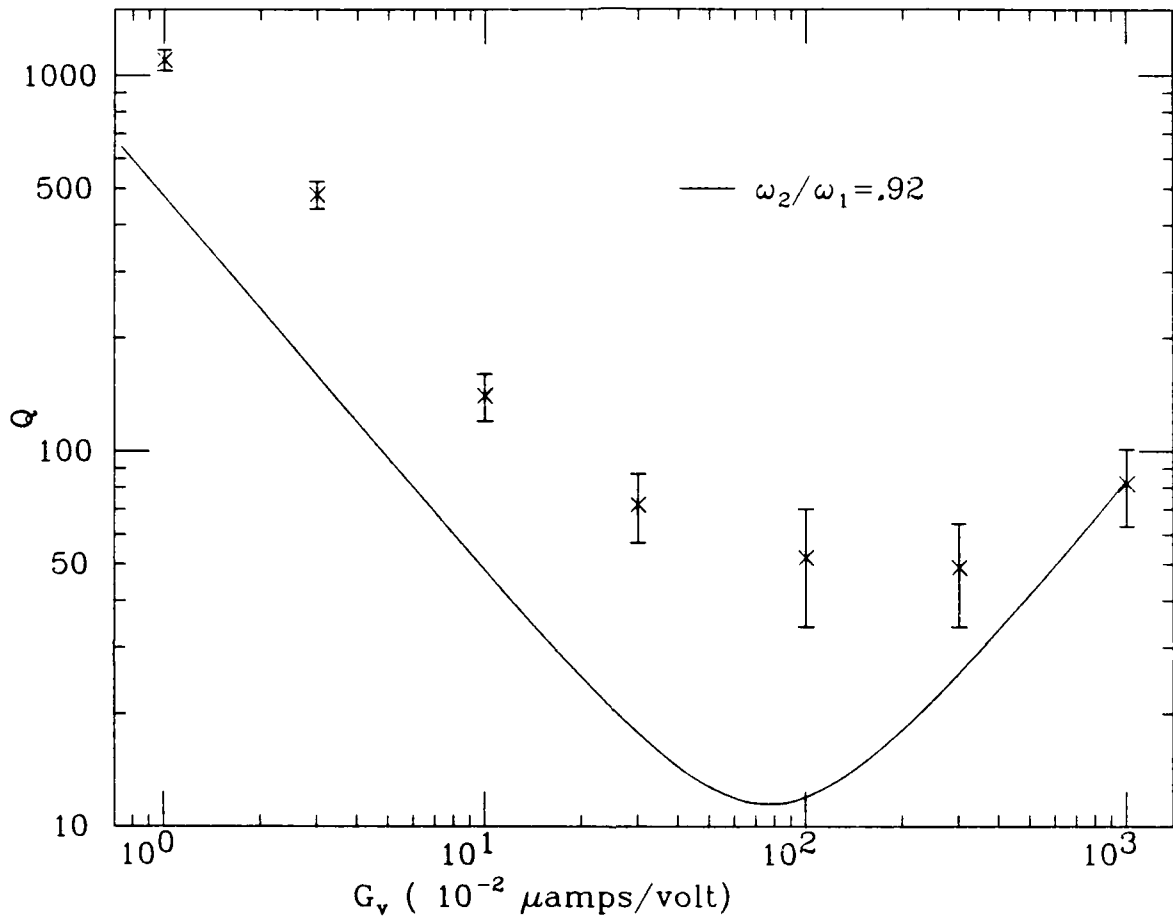


Figure 2.9  $Q$  of the differential mode as a function of feedback gain.

AD-A164 061

DEVELOPMENT OF A SENSITIVE SUPERCONDUCTING  
ACCELEROMETER AND GRAVITY GRADIOMETER(U) STANFORD UNIV  
CA DEPT OF PHYSICS H M FAIRBANK ET AL. SEP 84

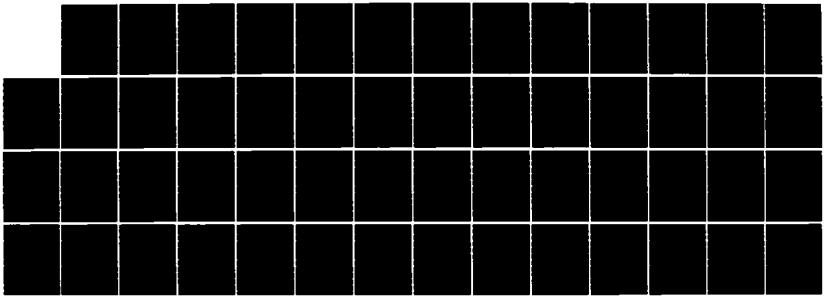
2/2

UNCLASSIFIED

AFOSR-TR-85-1126 AFOSR-80-0067

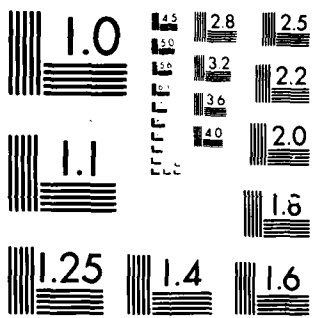
F/G 8/5

NL



END

FILED  
DA  
DTIC



MICROCOPY RESOLUTION TEST CHART  
1010 1000 1000 1000 1000 1000

According to [1.69]

$$R_{eff} = M_f G_v G_s Q_f \omega_f \quad [2.15]$$

where

$$\begin{aligned} M_f &= 10^{-6} \text{ H} \\ G_s &= 1.72 \times 10^5 \text{ V/A} \\ Q_f &= 50 \\ \omega_f &= 500 \text{ rad/sec.} \end{aligned}$$

With these values of the parameters

$$R_{eff} = G_v (4.1 \times 10^3 \text{ V} - \Omega/\text{A}). \quad [2.16]$$

Figure 2.9 shows the measured  $Q$  of the differential mode versus  $G_v$ , the current to voltage scale factor of the final stage of the feedback circuit. As  $G_v$  is changed,  $\omega_f$  must be readjusted so that the bandpass filter is tuned to the observed frequency of the mode. If  $G_v$  is made very large, the frequency falls to 73.8 Hz or 464 rad/sec. This is quite close to the expected value of  $\omega_2$ . The initial  $Q$  of the mode was  $3.2 \times 10^3$ . The minimum  $Q$  obtained was close to 50 rather than 11. This is probably due to the  $Q_f$  of the bandpass filter in the feedback circuit which was left at 50 as  $G_v$  was varied. The value of  $G_v$  which gives a minimum  $Q$  is larger than expected from [2.14] and [2.16], but this could easily be due to a smaller value of  $m_f$  than the design value of 1  $\mu\text{H}$ .

In operation this feedback loop reduced the signal at the resonant frequency by a factor of approximately 30 and greatly improved the stability of the SQUID.

#### 2.4 Thermal Sensitivity

The readout described in section 1.2 is sensitive to changes in the temperature of the gradiometer due to the variation of the penetration depth in niobium with temperature. A magnetic field applied to the surface

of a superconductor will decay exponentially inside the superconductor in a characteristic length  $\lambda$ , the penetration depth. This penetration depth is a function of temperature, and it is part of the gap between the readout coil and the opposite proof mass. So, as it changes with temperature the readout gap varies and a signal is detected. An approximation to the temperature dependence of  $\lambda$  is given by the two-fluid approximation

$$\frac{\lambda(t)}{\lambda_0} = \left[ 1 - \left( \frac{t}{t_c} \right)^4 \right]^{-1/2} \quad [2.17]$$

[Tinkham 1975], where  $\lambda_0 = 440 \text{ \AA}$  and  $t_c = 9.2^\circ \text{ K}$  for niobium. Taking the derivative of  $\lambda(t)$  with respect to temperature gives

$$\frac{d\lambda(t)}{dt} = \frac{2\lambda_0}{t_c} \left( \frac{t}{t_c} \right)^3 \left[ 1 - \left( \frac{t}{t_c} \right)^4 \right]^{-3/2} . \quad [2.18]$$

At  $4.2^\circ \text{ K}$

$$\frac{d\lambda(t)}{dt} = 9.7 \text{ \AA}/^\circ\text{K} . \quad [2.19]$$

Looking back at the introduction we see that a gravity gradient of 1 E produces a  $\Delta x$  of about  $2 \times 10^{-14} \text{ cm}$ , or  $2 \times 10^{-4} \text{ \AA}$ , so we can expect a small change in temperature to produce a large signal. This effect is larger than the length change caused by the coefficient of thermal expansion of the niobium. At  $20^\circ \text{ K}$  this coefficient is

$$\frac{1}{L} \frac{dL}{dt} = 3 \times 10^{-7}/^\circ\text{K}$$

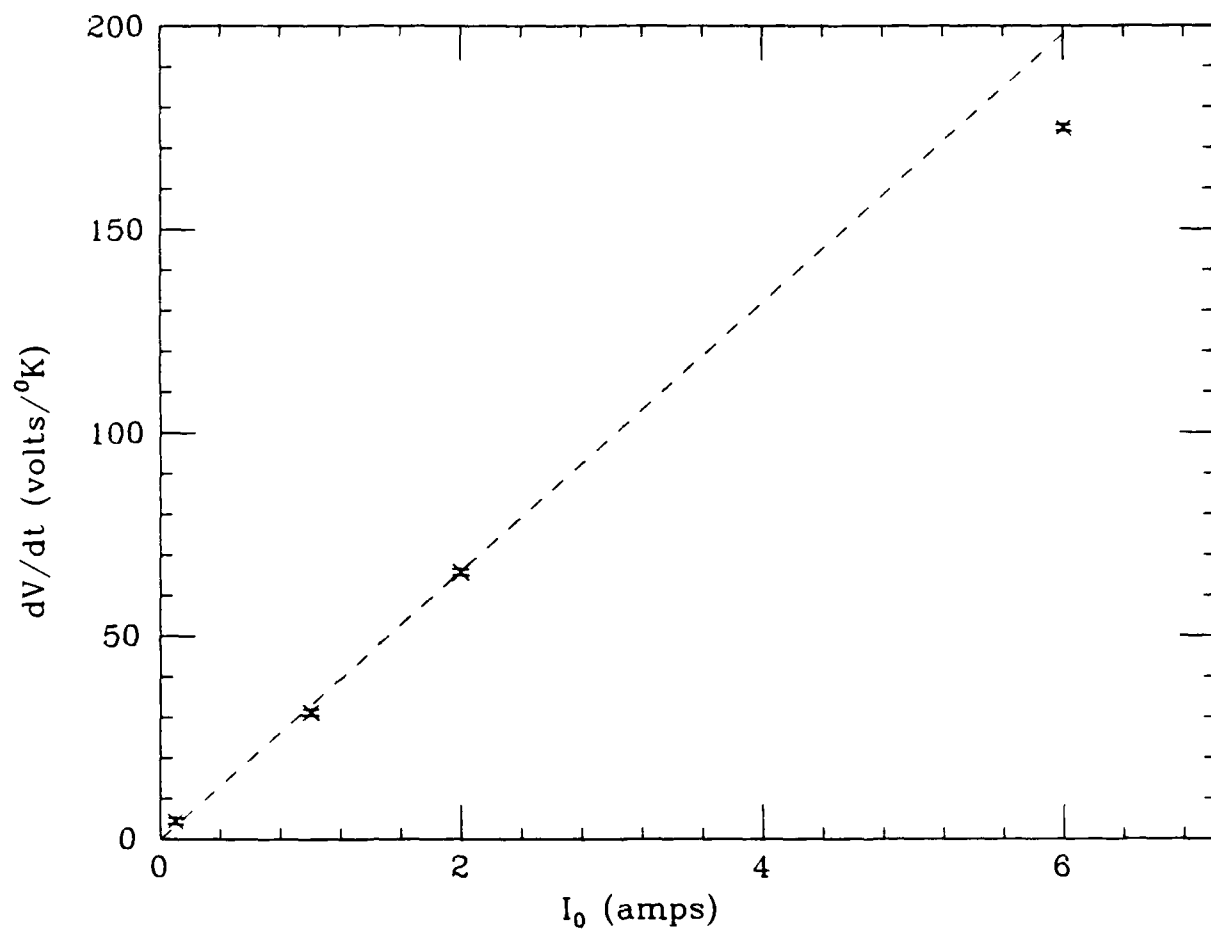


Figure 2.10 Temperature sensitivity as a function of persistent current.

[Corruccini 1961], and it is at least one order of magnitude smaller at 4.2° K. Using the size of the gap between the proof masses for L we have

$$\frac{dL}{dt} < .4 \text{ \AA}/^{\circ}\text{K} .$$

Measurements of the thermal sensitivity of the instrument as a function of stored current in the readout coil and gradiometer temperature have been carried out. Figure 2.10 shows  $dV/dt$  at 4.5° K versus readout current, where V is the output voltage of the differential SQUID.  $dV/dt$  increases linearly with  $I_0$ , and the slope of the fit is

$$31.6 \text{ V}/^{\circ}\text{K-A}.$$

The measurements were made with a thermometer and a temperature controller which stabilized the temperature by heating a coil wrapped around the case of the gradiometer. The thermometer was a carbon-glass resistor model CGR-1 manufactured by Lake Shore Cryotronics. Its conductance was measured with a potentiometric conductance bridge made by S.H.E. Corporation, and the temperature was controlled with a temperature controller also made by S.H.E. The response of the SQUID to temperature changes of a few millidegrees was measured at each current, and no hysteresis was apparent in the response. The slope above is about 9 times larger than would be predicted by considering  $d\lambda/dt$ . With 5A stored the scale factor is 1.2  $\mu\text{V}/\text{E}$  and 1E produces a relative motion of  $1.4 \times 10^{-14}$  cm, so the scale factor for displacement is

$$8.6 \times 10^7 \text{ V/cm}.$$

Using [2.19], and assuming that the magnetic field penetrates the readout coil and the proof mass equally we get

$$8.1 \times 10^8 \text{ V/cm}.$$



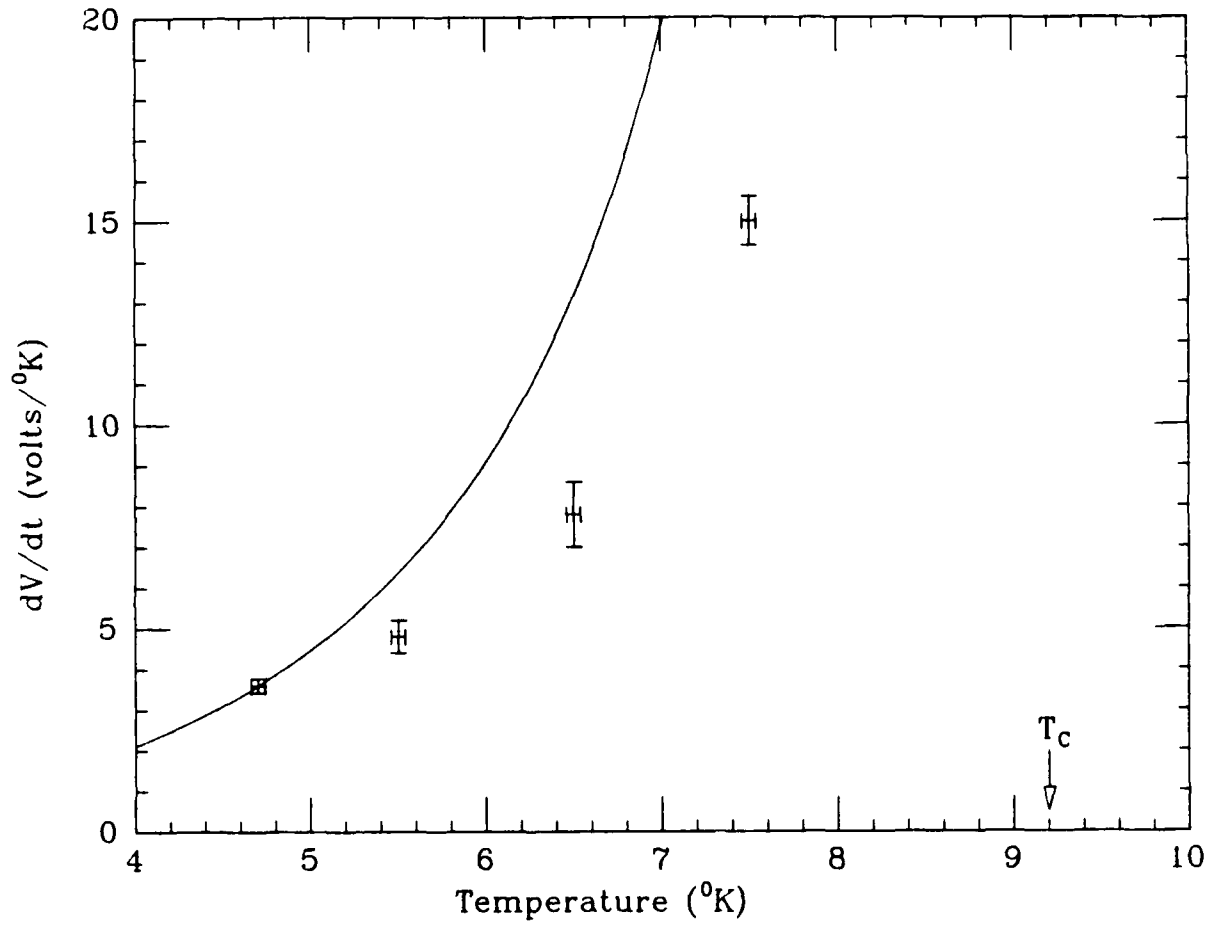


Figure 2.11 Temperature sensitivity as a function of temperature.

Part of this discrepancy could easily be due to penetration depth changes in other parts of the circuit. For instance the inductance of the transformer primary will change with temperature. It is also possible that the effective area of the wire in the readout coil is larger than the area of the proof mass, causing a larger change in inductance with temperature.

Figure 2.11 shows the behavior of the  $dV/dt$  as a function of temperature. The measurement points were taken with 100 mA in the readout loop. The solid curve shows the behavior of  $d\lambda/dt$  as a function of temperature from [2.18]. This curve is normalized to cross the measurement at  $4.7^\circ\text{K}$ . The measured points do not increase as rapidly as [2.18] but the rapid increase in  $dV/dt$  as temperature approaches  $9.2^\circ\text{K}$  does indicate that the temperature dependence is related to the superconductivity of niobium.

This very large temperature sensitivity may explain the excess gradiometer noise below 2 Hz. With 5A stored, the thermal sensitivity is  $158\text{ V}/^\circ\text{K}$  compared with a scale factor of  $1.2\ \mu\text{V}/\text{E}$ , so temperature fluctuations must be kept below  $10^{-8}\ ^\circ\text{K}$  to prevent them from contributing to the observed noise. We currently have a temperature control loop with a stability around  $10^{-6}\ ^\circ\text{K}$ , and the excess low frequency noise is about one hundred times the SQUID noise.

## 2.5 Flux Creep

Early experiments with superconducting gradiometers [Paik 1978] indicated that readouts of the type described here would show drift caused by flux creep if type II superconductors were used in the readout coils. This drift is caused by the motion of trapped flux lines in the magnetic field gradient of the readout coil [Anderson 1962], [Anderson 1964]. Flux is trapped in type II superconductors when  $H_{c1}$  of the material is exceeded.

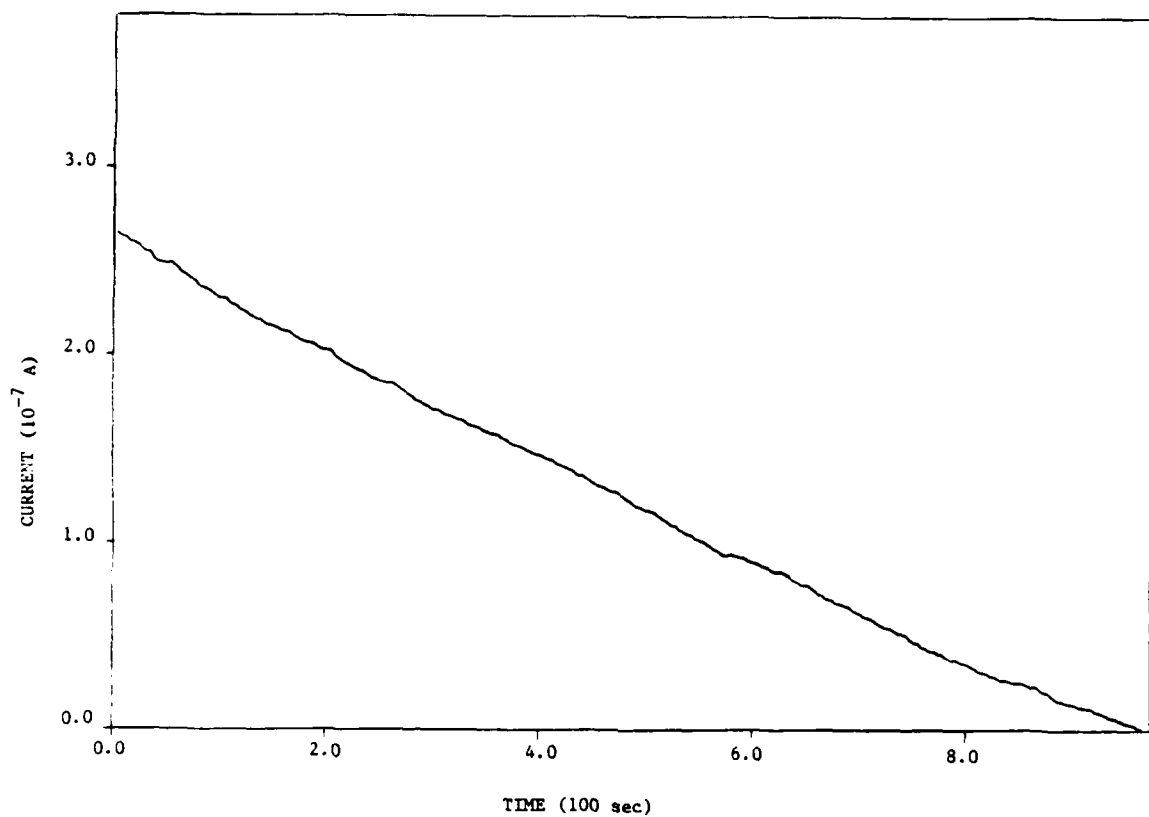


Figure 2.12 Drift in a Niobium-Titanium Loop

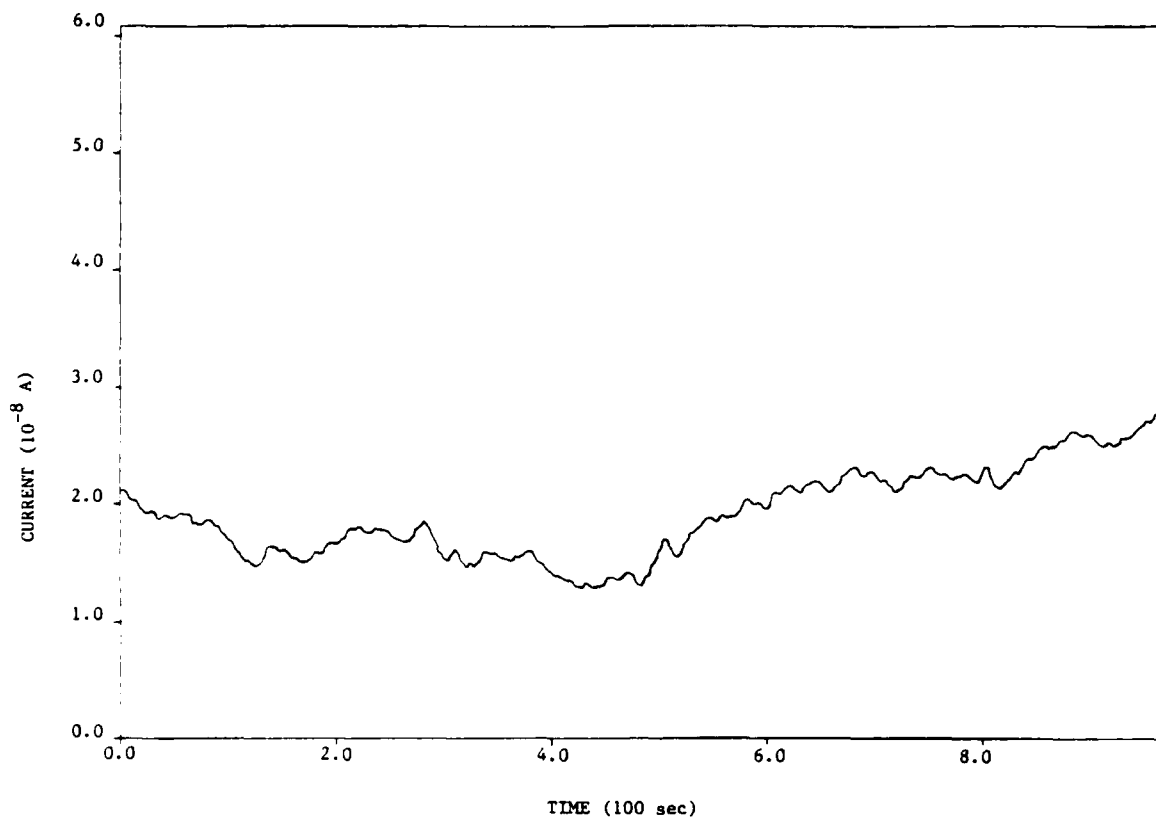


Figure 2.13 Drift in a Niobium Loop

The early readouts were constructed using Nb-Ti wire which has a very low  $H_{c1}$ . These readouts showed a steady drift like that expected from flux creep [Kim 1962]. To eliminate this problem we investigated the stability of pure niobium wire which has  $H_{c1} \approx 1000$  G.

In order to reduce the time required for cooldowns and changes in the experiment we constructed a small probe to operate as a dip stick in a narrow neck storage dewar. The probe is equipped with a small solenoid of the wire sample to be tested, a hall probe to detect the field produced by the persistent current in the sample, and a pickup coil which is wrapped around the wire sample and coupled to a SQUID to detect small changes in the persistent current.

Figure 2.12 shows the drift in the SQUID output with 2.0 A stored in a sample of Nb-Ti wire. Figure 2.13 shows the drift caused by 5.0A stored in a sample of pure niobium wire. The drift in the niobium-titanium is logarithmic as predicted for flux creep by the Anderson-Kim theory. The niobium sample does not show any steady drift, and the stability of the current is at least 25 times better than it is in the niobium-titanium. Because of these results, all of the coils in the gradiometer were built with pure niobium wire of the type tested in figure 2.13.

## 2.7 Magnetic Sensitivity

Since the source for the inverse square law test is a steel cylinder, careful magnetic shielding will be required to prevent the magnetic field of the source from causing a spurious signal. Because of this we have built several layers of magnetic shielding into the cryostat. The instrument itself is the first layer since it is a solid superconductor which shields

the pickup coil, transformers, and signal leads. The inside of the vacuum can is lined with another lead shield, and there is another lead shield and a  $\mu$ -metal shield outside the vacuum can.

This system was tested by applying a magnetic field to the outside of the dewar with a four foot coil and an audio amplifier. Fields up to 2 milli-gauss were applied and measured with a flux gate magnetometer without any reponse from the differential or common mode SQUID. The system can easily be tested to higher fields if necessary with a more powerful amplifier to drive the coil.

## CHAPTER 3

### Evidence for the Inverse Square Law

#### 3.1 Celestial Mechanics

The original and strongest evidence in favor of the inverse square law of gravitation comes from observations of the mechanics of motion in the solar system. The most stringent limits on variations in  $G$  come from the agreement between theory and observation of the precession of the perihelia of several bodies in the solar system and the binary pulsar (PSR 1913 + 16). Additional, but weaker, constraints on possible variations in  $G$  can be derived by comparing determinations of planetary masses made by observing the planet's effect on the orbits of other bodies at different distances from the planet [Mikkelson 1977].

The orbits of bound particles in an inverse square force field are closed ellipses, and small deviations from this force law cause orbital precession such as that caused by corrections due to general relativity. Consequently, any variation of  $G$  with distance would cause a discrepancy between observed rates of precession and those predicted from the interaction of the planets and relativistic effects. Consider the motion of a body of mass  $m$  in a central force field  $F(r)$ , since angular momentum is conserved

$$mr^2 \dot{\theta} = L \quad [3.1]$$

is a constant, and the radial equation of motion becomes [Goldstein 1950]

$$\ddot{r} - L^2/mr^3 = F(r)/m \quad [3.2]$$

For a nearly circular orbit of radius  $a$  we can expand [3.2] in a power series in  $x = r - a$ , so

$$\ddot{x} - \frac{L}{ma^2} \left\{ 1 - \frac{3x}{a} + \dots \right\} = \frac{1}{m} \left\{ F(a) + F'(a)x + \dots \right\} . \quad [3.3]$$

Using [3.2] to cancel the terms which are constant we have

$$\ddot{x} - \left[ \frac{3F(a)}{a} + F'(a) \right] x = 0 , \quad [3.4]$$

to first order in  $x$ . From this we can see that the body oscillates harmonically about the circular orbit with a period

$$T = 2\pi \left\{ \frac{ma}{-[3F(a)+aF'(a)]} \right\}^{\frac{1}{2}} . \quad [3.5]$$

Since  $\dot{\theta}$  is approximately constant, the advance of a planet's perihelion in one orbit is

$$\Delta\theta = T \dot{\theta} = \frac{2\pi L}{a} \left\{ \frac{a}{-[3F(a)+aF'(a)]} \right\}^{\frac{1}{2}} - 2\pi \quad [3.6]$$

Using [3.2] again

$$\Delta\theta = 2\pi \left\{ \left[ 3 + \frac{aF'(a)}{F(a)} \right]^{\frac{1}{2}} - 1 \right\} . \quad [3.7]$$

Now suppose that  $G$  does vary with  $r$ , so that

$$F(r) = -\frac{G(r)M}{r^2} . \quad [3.8]$$

Applying [3.7] we find

$$\Delta\theta = \frac{-\pi a G'(a)}{G(a)} , \quad [3.9]$$



to first order in  $G'(a)/G(a)$ . The most accurate measurements of orbital precession have been done on the orbit of Mercury where the general relativistic effects are largest. The predicted value of  $\Delta\theta$  for Mercury after subtracting out the effects of other planets on its orbit is

$$\Delta\theta_{\text{mer}} = 5.01 \times 10^{-7} \text{ rad/orbit} ,$$

where  $\Delta\theta$  is calculated with the relativistic formula [Marion 1970]

$$\Delta\theta = 6G\pi M_s / [c^2 a(1 - e^2)] ,$$

where  $M_s$  is the solar mass,  $C$  is the speed of light,  $a$  is the semimajor axis of the orbit, and  $e$  is the orbital eccentricity. The measured value of  $\Delta\theta_{\text{mer}}$  is [Shapiro 1976]

$$\Delta\theta_{\text{mer}} = 5.03 \pm .02 \times 10^{-7} \text{ rad/orbit.}$$

The excellent agreement of these numbers places a stringent limit on  $aG'(a)/G(a)$  for  $a = 5.8 \times 10^7$  km, the semimajor axis of Mercury's orbit. Measurements on the orbit of Mars [Laubscher 1971] and the orbit of Icarus [Shapiro 1971] also give good agreement with general relativity. These measurements rule out variations of  $G$  of more than a few parts in  $10^8$  at ranges close to  $10^8$  km. Observations of the binary pulsar PSR 1913 + 16 [Taylor 1976] indicate that  $G$  is constant to parts in  $10^5$  at  $10^6$  km.

A comparison of  $G$  at distances down to about  $10^4$  km with  $G$  at  $10^8$  km can be made by comparing determinations of the masses of the inner three planets made at these two distances. The first mass determination comes from analysis of inner planetary radar ranging data where the distances between the planet and the body whose orbit it perturbs is on the order

of  $10^8$  km [Shapiro 1973]. For Mercury and Venus, the second mass determination comes from observations of the trajectory of Mariner 10. Mariner 10 flew by Venus with a minimum separation of  $10^4$  km [Howard 1974] and came within  $3 \times 10^3$  km of Mercury [Esposito 1976]. The second mass determination for the earth-moon system was made with lunar laser ranging data. This comparison leads to a limit on the change in  $G$  between  $3 \times 10^3$  km and  $3 \times 10^8$  km of  $5 \times 10^{-4}$  [Mikkelson 1977].

In summary, the inverse square law is very well verified at astronomical distances and any proposed violation must be extremely small at these ranges. However, the exponential deviation of equation [I.1] has this property and is not constrained by solar system data if  $\beta^{-1} \ll 10^3$  km. Long has proposed a violation of the form

$$G(r) = G(1 + .002 \ln r), \quad [3.10]$$

[Long 1976] based on laboratory data, but some mechanism must cut such a violation off at distances of 1000 km because it predicts a change in  $G$  of 10% between  $10^3$  km and  $10^8$  km.

### 3.2 G Measurements

At laboratory distance scales measurements of  $G$  provide some slight evidence that  $G$  is constant. Long has reviewed a number of precise laboratory measurements [Long 1974]. A plot of these measurements is shown in figure 3.1. The measurements are consistent at the level of three standard deviations, but Long points out that variations in  $G$  of less than 1% over this distance range are allowed by the data. He fits the dashed line to the data using equation [3.10], and his own measurements at 4.5 cm and 30 cm [Long 1976].

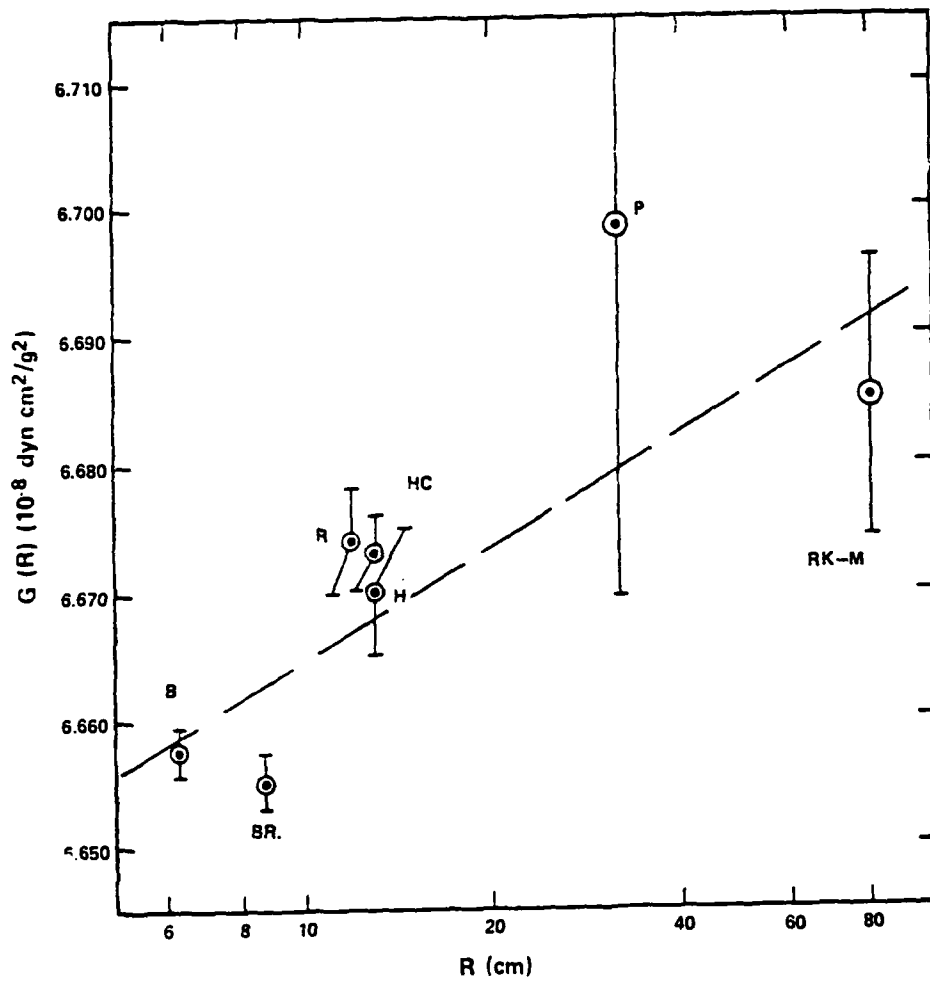


Figure 3.1  $G$  as a Function of Mass Separation [From D.R. Long, Phys. Rev. D 9, 850 (1974)].

Most of the measurements in figure 3.1 were made with torsion balances; the technique pioneered by Cavendish in 1798, although Poynting and Richarz used ordinary balances to detect the change in weight on a test mass from an attracting mass. The most modern measurement of Rose et al. was made by measuring the angular acceleration on a torsion balance mounted on a rotating table subject to a constant torque from masses also mounted on the table. The references for the various points are:

B	[Boys 1895]
BR	[Braun 1896]
P	[Poynting 1891]
RK-M	[Richarz 1898]
H	[Heyl 1930]
HC	[Heyl 1942]
R	[Rose 1969], also see [Beams 1971].

Long's measurement also employed a torsion balance. He used two rings as the attracting masses and positioned the test mass of the torsion balance at the point where the derivative of force with respect to distance is zero for each ring in order to reduce the necessary positioning accuracy. Although the G measurements cannot be construed as verifying Long's measurement, they do leave open the possibility that something very fundamental is going on. Long has pointed out another set of measurements which are consistent with his own. These were made by measuring the frequency shift in a torsion balance as an attracting mass was moved between several locations [Karagioz 1976]. Long has analyzed their data and found a value for  $\lambda$  in the equation

$$G(r) = G [1 + \lambda \ln r] , \quad [3.11]$$

of  $\lambda = (2.01 \pm .61) \times 10^{-3}$

[ Long 1979 ] .

### 3.3 Recent Experiments

Since 1976, when Long first claimed that a violation of the inverse square law exists, some work has been done with the specific purpose of checking his results. The only work to claim an accuracy better than Long's was done at U.C. Irvine [ Spero 1980 ] using a method similar to that described here. The U.C. Irvine group used a torsion balance to measure the horizontal gravitational gradient at the center of a stainless steel cylinder. Their cylinder has a diameter to length ratio of about .1 and is 60 cm long. The gradient was measured by moving the cylinder so that the proof mass of the torsion balance was next to one wall and comparing this to the force on the balance with the proof mass next to the other wall. They used  $\gamma$ -ray transmission studies to measure the homogeneity of their source. They find a value for  $\lambda$  in [3.11] of

$$\lambda = (1 \pm 7) \times 10^{-5} .$$

This would appear at least to rule out Long's logarithmic model for the violation, but Long has argued that such a form might arise from a vacuum polarization effect similar to the effect which produces a logarithmic modification of Coulomb's law at short distances [ Long 1980a ] . Such an effect might be unobservable in a null experiment due to the lack of a polarizing field [ Long 1980b ] .

Several other interesting experiments have been done, but none has sufficient accuracy to rule out Long's result. Panov and Frontov [Panov 1979] used a torsion balance to measure the ratio of G at 3 m to G at .4 m, and the ratio of G at 10 m to G at .4 m. Their results were

$$\frac{G(3m)}{G(.4m)} = 1.003 \pm .006 ,$$

and

$$\frac{G(10m)}{G(.4m)} = .998 \pm .012 .$$

Unfortunately, the stated errors are comparable to the size of the effect predicted by Long. Hirakawa [Hirakawa 1980] has measured the interaction between a gravity wave antenna resonant at 60.5 Hz and a steel bar rotating at 30.3. His analysis of the data confirms Newton's law to  $\pm 3\%$  over the range from 2 to 5 m, but this error is almost ten times the expected effect from Long's work. Taken as a whole, this work indicates that more precise measurements at different ranges will continue to be interesting and challenging for some time.

## CHAPTER 4

### Analysis of the Inverse Square Law Experiment

#### 4.1 Newtonian field of a Cylindrical Shell

In this chapter we will describe the source and some possible signals from our planned experiment. Our source is a large steel cylindrical shell which is designed to fit over the dewar containing the gravity gradiometer. This cylinder was machined from a centrifugal casting of ASTM-27 grade 60-30 normalized steel. Its length is 5.080 m, the inside diameter is 0.4572 m, and the outside diameter is .5588 m. This gives it a mass  $3.24 \times 10^3$  kg or  $7.15 \times 10^3$  lbs. For the moment we will assume that this source is perfectly cylindrical and homogeneous for the purpose of calculating its gravitational field. We will analyze the errors due to deformation and inhomogeneity of this source in a later section.

The acceleration produced by the gravitational field on a test particle positioned at  $\vec{p}(r, \phi, z)$  is given by

$$\vec{a}(r, \phi, z) = \int_{-L/2}^{L/2} \int_0^{2\pi} \int_{R-t}^{R+t} \frac{-G(\vec{p} - \vec{p}')}{|\vec{p} - \vec{p}'|^3} r' dr' d\phi' dz' , \quad [4.1]$$

where  $G$  is the gravitational coupling constant,  $\sigma$  is the density of the cylinder,  $\vec{p}'$  is the integration variable, and  $R$  is the mean diameter of the cylinder. The coordinates are shown in Figure 4.1. It is clear from symmetry considerations that the result for  $\vec{a}$  must be independent of  $\phi$  so we may set  $\phi = 0$  and consider only a test particle in the  $z$ - $x$  plane. Then

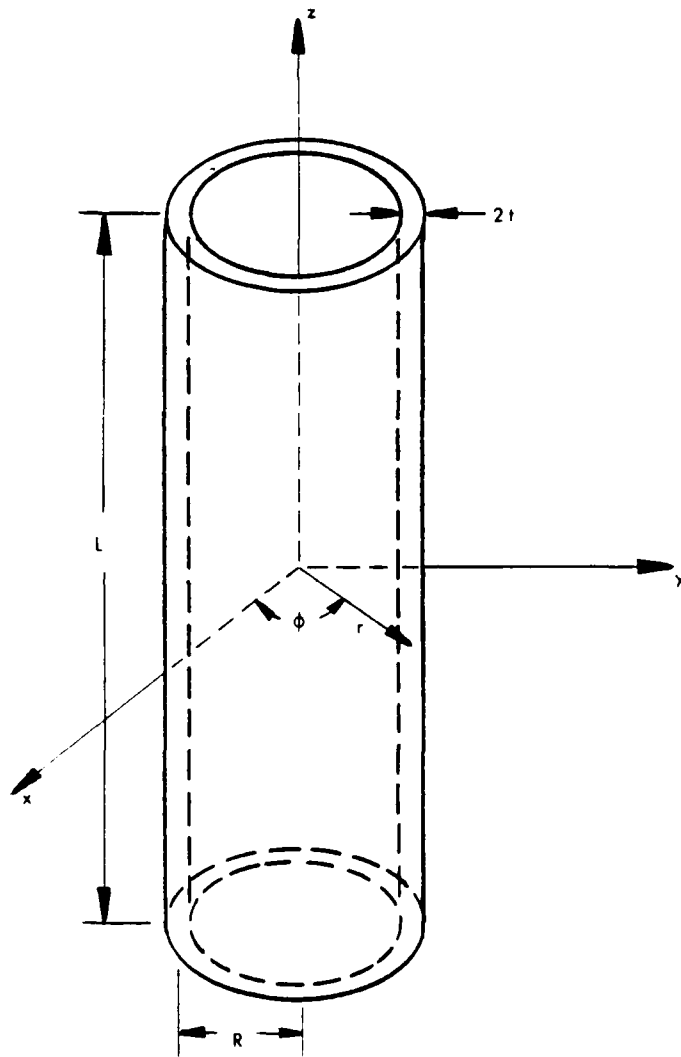


Figure 4.1 Cylinder Coordinates



$$\vec{p} = r\hat{r} + z\hat{z} = r\hat{i} + z\hat{k},$$

and

$$\vec{p}' = r'[\hat{i} \cos \phi' + \hat{j} \sin \phi'] + z' \hat{k}.$$

So

$$\vec{p} - \vec{p}' = (r - r' \cos \phi') \hat{i} - r' \sin \phi' \hat{j} + (z - z') \hat{k}, \quad [4.2]$$

and for  $\vec{a}$  we have

$$\vec{a}(r, z) = -G\sigma \int_{-L/2}^{L/2} \int_0^{2\pi} \int_{R-t}^{R+t} \frac{[(r-r' \cos \phi') \hat{i} - r' \sin \phi' \hat{j} + (z-z') \hat{k}] r' dr' d\phi' dz}{[(z-z')^2 + r^2 + r'^2 - 2rr' \cos \phi']^{3/2}} \quad [4.3]$$

Note that the integral over  $\phi'$  in the  $\hat{j}$  term vanishes, since this term has odd parity.

Let us define the dimensionless variables  $2z/L = \zeta$ ,  $2z'/L = \zeta'$ ,  $r/R = \xi$ ,  $r'/R = \alpha$ ,  $\eta = 2R/L$ , and  $\omega = t/R$ . Then

$$\vec{a}(r, z) = -\frac{G\sigma \eta^2 L}{2} \int_{-1}^1 \int_0^{2\pi} \int_{1-\omega}^{1+\omega} \frac{\alpha [\eta(\xi - \alpha \cos \phi') \hat{i} + (\zeta - \zeta') \hat{k}]}{[(\zeta - \zeta')^2 + \eta^2(\xi^2 + \alpha^2 - 2\xi\alpha \cos \phi')]^{3/2}} d\alpha d\phi' d\zeta'. \quad [4.4]$$

Our experiment will entail measurements of gradients of the cylinder, so we want to calculate  $\partial a_z / \partial z$ , and  $\partial a_r / \partial r$ . We also need to know how these quantities vary with position near the center of the cylinder, in order to determine how accurately the gradiometer needs to be positioned in the cylinder. First we calculate  $\partial a_r / \partial r$  for  $z = 0$ . Then

$$a_r(r,0) = \frac{-G\sigma\eta^2 L}{2} \int_{-1}^1 \int_0^{2\pi} \int_{1-\omega}^{1+\omega} \frac{\alpha \eta (\xi - \alpha \cos \phi') d\alpha d\phi' d\zeta'}{[\zeta'^2 + \eta^2 (\xi^2 + \alpha^2 - 2\xi\alpha \cos \phi')]^{3/2}} . \quad [4.5]$$

Doing the integral over  $\zeta'$ , we have

$$a_r(r,0) = -2G\sigma R \int_0^{2\pi} \int_{1-\omega}^{1+\omega} \frac{\alpha (\xi - \alpha \cos \phi') [1 + \eta^2 (\xi^2 + \alpha^2 - 2\xi\alpha \cos \phi')]^{-1/2}}{[\xi^2 + \alpha^2 - 2\xi\alpha \cos \phi']} d\phi' d\alpha . \quad [4.6]$$

Now since  $\eta^2 = 0.01$  for our source we can expand in a power series in  $\eta^2$ , and then integrate over  $\phi'$  term by term. Then

$$a_r(r,0) = -2G\sigma R \int_0^{2\pi} \int_{1-\omega}^{1+\omega} \frac{\alpha (\xi - \alpha \cos \phi')}{[\xi^2 + \alpha^2 - 2\xi\alpha \cos \phi']} \left[ 1 - \frac{\eta^2}{2} (\xi^2 + \alpha^2 - 2\xi\alpha \cos \phi') + \frac{3}{8} \eta^4 (\xi^2 + \alpha^2 - 2\xi\alpha \cos \phi')^2 - \frac{5}{16} \eta^6 (\xi^2 + \alpha^2 - 2\xi\alpha \cos \phi')^3 + 0(\eta^8) \right] . \quad [4.7]$$

The  $\phi'$  integration over the first term gives zero, so

$$a_r(r,0) = 2G\sigma R \int_{1-\omega}^{1+\omega} \alpha \eta^2 \pi \xi \left[ 1 - \frac{3}{4} \eta^2 (\xi^2 + 2\alpha^2) + \frac{5}{8} \eta^4 [(\xi^2 + \alpha^2)^2 + 2(\xi^2 + \alpha^2)\alpha^2 + 2\alpha^2 \xi^2] - \frac{35}{64} \eta^6 [(\xi^2 + \alpha^2)^3 + 3\alpha^2 (\xi^2 + \alpha^2)^2 + 6\alpha^2 \xi^2 (\xi^2 + \alpha^2) + 3\alpha^4 \xi^2] \right] d\alpha . \quad [4.8]$$

The cylinder mass is given by

$$M = \pi [(R+t)^2 - (R-t)^2] L \sigma = 2R^2 L \pi \sigma \int_{1-\omega}^{1+\omega} \alpha d\alpha . \quad [4.9]$$

Let us define

$$A_n(\omega) = \int_{1-\omega}^{1+\omega} \alpha^n d\alpha = \frac{(1+\omega)^{n+1} - (1-\omega)^{n+1}}{n+1} .$$

[ 4.10]

Then  $M = 2R^2 L \pi \sigma A_1(\omega)$ . Finally we do the integration over  $\alpha$ . We have

$$\begin{aligned} a_r(r, \theta) = & \frac{GM\eta^2}{RL} \xi \left[ 1 - \frac{3\eta^2}{2} \left( \frac{\xi^2}{2} + \frac{A_3(\omega)}{A_1(\omega)} \right) \right. \\ & + \frac{15}{8} \eta^4 \left[ \frac{\xi^4}{3} + 2 \xi^2 \frac{A_3(\omega)}{A_1(\omega)} + \frac{A_5(\omega)}{A_1(\omega)} \right] \\ & \left. - \frac{35}{16} \eta^6 \left[ \frac{\xi^6}{4} + 3 \frac{\xi^4 A_3(\omega)}{A_1(\omega)} + \frac{9}{2} \xi^2 \frac{A_5(\omega)}{A_1(\omega)} + \frac{A_7(\omega)}{A_1(\omega)} \right] + o(\eta^8) \right] \end{aligned}$$

[ 4.11]

But

$$\frac{A_3(\omega)}{A_1(\omega)} = 1 + \omega^2 ,$$

and

$$\frac{A_5(\omega)}{A_1(\omega)} = 1 + \frac{10}{3} \omega^2 + \omega^4 ,$$

and

$$\frac{A_7(\omega)}{A_1(\omega)} = 1 + 7\omega^2 + 7\omega^4 + \omega^6 ,$$

so

$$\begin{aligned}
a_r(r,0) = & \frac{GM}{LR} \eta^2 \xi \left\{ 1 - \frac{3}{2} \eta^2 \left( 1 + \left( \frac{t}{R} \right)^2 + \frac{\xi^2}{2} \right) \right. \\
& + \frac{15}{8} \eta^4 \left[ 1 + \frac{10}{3} \left( \frac{t}{R} \right)^2 + \left( \frac{t}{R} \right)^4 + 2\xi^2 \left( 1 + \left( \frac{t}{R} \right)^2 \right) + \frac{\xi^4}{3} \right] \\
& - \frac{35}{16} \eta^6 \left[ 1 + 7 \left( \frac{t}{R} \right)^2 + 7 \left( \frac{t}{R} \right)^4 + \left( \frac{t}{R} \right)^6 + \frac{9}{2} \xi^2 \left( 1 + \frac{10}{3} \left( \frac{t}{R} \right)^2 \right) \right. \\
& \left. \left. + \left( \frac{t}{R} \right)^4 \right) + 3\xi^4 \left( 1 + \left( \frac{t}{R} \right)^2 \right) + \frac{\xi^6}{4} \right] + o(\eta^8) \left. \right\} .
\end{aligned}$$

[4.12]

Since  $\eta$  is 1/100 and  $\omega$  is 1/20, only the first two terms in this expression give measureable contributions. The solution has two important advantages. The lowest order contribution to  $\partial a_r / \partial r$  is  $GM/R^2 L(2R/L)^2$ . This is quite small since  $2R/L$  is small; consequently any new non-newtonian force makes a proportionally larger contribution to the central gradient. Ideally the newtonian term would be zero, and we would be doing a true null experiment. However, this would require an infinitely long cylinder, so we must settle for a cylinder which attenuates the newtonian gradient by a factor of 100. The second advantage is that the gradient in the central plane of the cylinder is nearly independent of position.

Consider the lowest order term in the force equation [4.12], which is of the form  $\vec{a} = Cr\hat{r}$  where  $C$  is a constant. In the  $x$ - $y$  coordinates this has the form  $\vec{a} = c(x\hat{x} + y\hat{y})$ . Hence  $\partial a_x/\partial x = \partial a_y/\partial y = c$  anywhere in the central plane. The lowest order correction to this is  $-3/4 \eta^2 \xi^2$  which is very small. If we want to measure the central gradient to 0.1% we need only have  $\xi^2 < (.1) 4/3$ , or  $r < (.37)R = 18.8$  cm. This is a very weak centering requirement.

Next we consider variations of  $\partial a_r/\partial r$  with  $z$ . Using equation [4.4] we have

$$g_r(z) = \left. \frac{\partial a_r}{\partial r} \right|_{r=0} = \frac{-G\sigma\eta^2 L}{2R} \int_{-1}^1 \int_0^{2\pi} \int_{1+\omega}^{1-\omega} \alpha\eta \left\{ \frac{1}{[(\zeta - \zeta')^2 + (\alpha\eta)^2]^{3/2}} - \frac{3\eta^2 \alpha^2 \cos^2 \phi'}{[(\zeta - \zeta')^2 + (\alpha\eta)^2]^{5/2}} \right\} d\alpha d\phi' d\zeta' . \quad [4.13]$$

Doing the  $\phi'$  integral

$$g_r(z) = \frac{-G\alpha\pi L}{R} \eta^2 \int_{-1}^1 \int_{1-\omega}^{1+\omega} \alpha\eta \left\{ \frac{1}{[(\zeta - \zeta')^2 + (\alpha\eta)^2]^{3/2}} - \frac{3}{2} \frac{(\alpha\eta)^2}{[(\zeta - \zeta')^2 + (\alpha\eta)^2]^{5/2}} \right\} d\alpha d\zeta' . \quad [4.14]$$

Doing the integral over  $\alpha$

$$g_r(z) = \frac{-G\sigma L\pi}{R} \int_{-1}^1 \left\{ \frac{-1}{[(\zeta - \zeta')^2 / \eta^2 + \alpha^2]^{1/2}} \right\}_{\alpha=1-\omega}^{\alpha=1+\omega} - \frac{3}{2} \left[ \frac{-1}{[(\zeta - \zeta')^2 / \eta^2 + \alpha^2]^{1/2}} + \frac{1}{3\eta^2} \frac{(\zeta - \zeta')^2}{[(\zeta - \zeta')^2 / \eta^2 + \alpha^2]^{3/2}} \right]_{\alpha=1-\omega}^{\alpha=1+\omega} d\zeta'. \quad [4.15]$$

Or

$$g_r(z) = \frac{-G\sigma\pi\eta L}{R} \int_{-1}^1 \left\{ \frac{1}{2} \left( \frac{1}{[(\zeta - \zeta')^2 + \eta^2(1+\omega)^2]^{1/2}} - \frac{1}{[(\zeta - \zeta')^2 + \eta^2(1-\omega)^2]^{1/2}} \right) - \frac{1}{2} \frac{(\zeta - \zeta')^2}{[(\zeta - \zeta')^2 + \eta^2(1+\omega)^2]^{3/2}} + \frac{(\zeta - \zeta')^2}{2[(\zeta - \zeta')^2 + \eta^2(1-\omega)^2]^{3/2}} \right\} d\zeta'$$

$$= -G\sigma\pi \left[ \frac{(1-\zeta)}{[(1-\zeta)^2 + \eta^2(1+\omega)^2]^{1/2}} + \frac{(1+\zeta)}{[(1+\zeta)^2 + \eta^2(1+\omega)^2]^{1/2}} - \frac{(1-\zeta)}{[(1-\zeta)^2 + \eta^2(1+\omega)^2]^{1/2}} - \frac{(1+\zeta)}{[(1+\zeta)^2 + \eta^2(1-\omega)^2]^{1/2}} \right]. \quad [4.16]$$

To the lowest order in  $\omega$  thus can be rewritten as

$$g_r(z) = \frac{1}{2} \frac{GM}{LR^2} \eta^2 \left\{ \frac{(1+\zeta)}{[(1+\zeta)^2 + \eta^2]^{3/2}} + \frac{(1-\zeta)}{[(1-\zeta)^2 + \eta^2]^{3/2}} \right\}. \quad [4.17]$$

This function is shown in figure 4.2. It is evidently quite flat near the center of the cylinder and falls off rapidly outside the end. To determine how accurately the gradiometer needs to be positioned vertically to measure the central gradient we expand  $\partial a_r / \partial r|_{r=0}$  in  $\zeta$  for small  $\zeta$  using [4.16]. This gives

$$g_r(z) \cong \frac{GM}{LR^2} \eta^2 \left\{ 1 + 3 \zeta^2 + \sigma(\zeta^4) + \sigma(\zeta^2 \eta^2) + \sigma(\eta^2) \right\} .$$

[4.18]

So the gradient error produced by a vertical positioning error is second order in the vertical displacement of the gradiometer from the center of the cylinder. Symmetry requires that the error be some even power of  $\zeta$ . An error of less than 1 part in  $10^3$  requires that the gradiometer be within 4.6 cm of the center. This is more severe than the radial positioning requirement but still is easily obtainable.

There is one further positioning error which needs consideration. Newtonian gravitation obeys Poisson's equation so that if  $\phi$  is the gravitational potential, then in vacuum

$$\nabla^2 \phi = \frac{\partial^2 \phi}{\partial x^2} + \frac{\partial^2 \phi}{\partial y^2} + \frac{\partial^2 \phi}{\partial z^2} = 0 .$$

[4.19]

For a perfect cylinder, symmetry requires that

$$\frac{\partial^2 \phi}{\partial r^2} = \frac{\partial^2 \phi}{\partial x^2} = \frac{\partial^2 \phi}{\partial y^2} ,$$

[4.20]

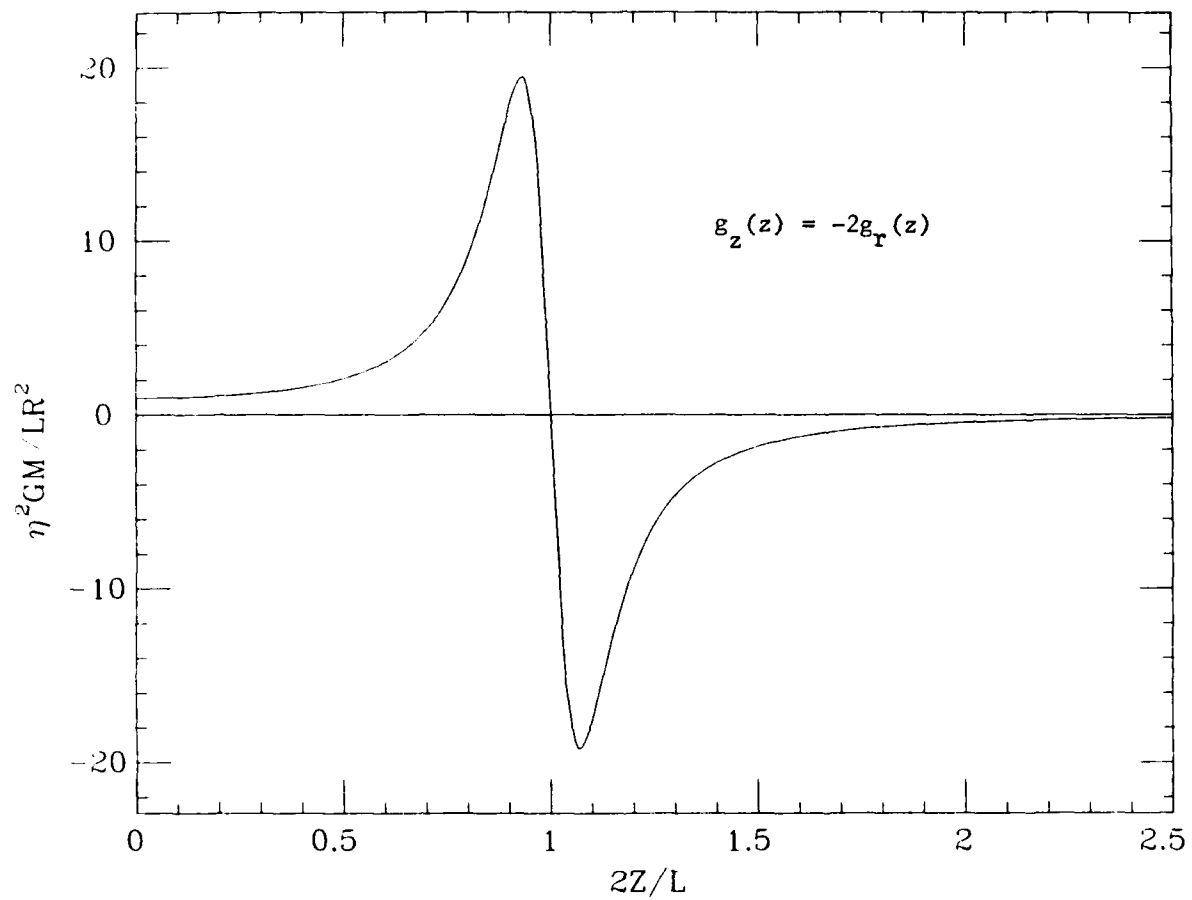


Figure 4.2  $g_r(z)$  as a Function of  $2Z/L$



so

$$\frac{\partial^2 \phi}{\partial z^2} = -2 \frac{\partial^2 \phi}{\partial r^2} .$$

[4.21]

This means that as the gradiometer is tilted away from horizontal up to vertical its output will change by a factor of -2, hence a degree of leveling accuracy is needed. To determine this we need to evaluate the gradient signal at the center of the cylinder as a function of angle between the gradiometer sensitive axis and the horizontal direction. If we project the acceleration onto this direction, we have

$$a_{\theta} = \vec{a} \cdot \hat{n} ,$$

where

$$\hat{n} = \hat{i} \cos \theta + \hat{k} \sin \theta .$$

The differential of  $a_{\theta}$  is

$$da_{\theta} = \left[ \frac{\partial a_{\theta}}{\partial x} , \frac{\partial a_{\theta}}{\partial z} \right] ,$$

and the directional derivative of  $a_{\theta}$  along the  $\hat{n}$  direction is then given by

$$g_{\theta} = \frac{\partial a_{\theta}}{\partial x} \cos \theta + \frac{\partial a_{\theta}}{\partial z} \sin \theta ,$$

[4.22]

see for example [Buck 1965]. But

$$\begin{aligned}\frac{\partial a_\theta}{\partial x} &= \frac{\partial}{\partial x} \left[ a_x \cos \theta + a_z \sin \theta \right] \\ &= \frac{\partial a_x}{\partial x} \cos \theta + \frac{\partial a_z}{\partial x} \sin \theta ,\end{aligned}$$

and

$$\begin{aligned}\frac{\partial a_\theta}{\partial z} &= \frac{\partial}{\partial z} \left[ a_x \cos \theta + a_z \sin \theta \right] \\ &= \frac{\partial a_x}{\partial z} \cos \theta + \frac{\partial a_z}{\partial z} \sin \theta .\end{aligned}$$

Evaluating these quantities at the center of the cylinder, we have

$$\frac{\partial a_x}{\partial z} = \frac{\partial a_z}{\partial x} = 0 ,$$

since  $a_x \equiv 0$  along the  $z$  axis and  $a_z \equiv 0$  in the central plane of the cylinder. Using equation [4.22],

$$\begin{aligned}g_\theta &= \frac{\partial a_x}{\partial x} \cos^2 \theta + \frac{\partial a_z}{\partial z} \sin^2 \theta \\ &= \frac{\partial a_x}{\partial x} \left[ \cos^2 \theta - 2 \sin^2 \theta \right] \\ &= \frac{\partial a_x}{\partial x} \left[ 1 - 3 \sin^2 \theta \right] .\end{aligned}\tag{4.23}$$

These results can also be obtained by considering a similarity transformation on the tensor  $\Gamma$  which rotates the spatial coordinates with respect to the cylinder axis [Goldstein 1959].

In order to have  $3 \sin^2 \theta \leq 10^{-3}$  we need  $\theta \leq 1^\circ$ . This seems a rather severe constraint. Fortunately  $g_\theta$  at  $\theta = 0$  is a maximum, so that by measuring  $g$  at three values of  $\theta$  which we separate by a known  $\Delta\theta$ ;  $\partial a_x / \partial x = g_x$  can readily be found by interpolation.

To summarize, the radial gradient at the center of the cylinder  $g_r$  is

$$g_r = \frac{GM}{LR^2} \left( \frac{2R}{L} \right)^2 \left[ 1 + \left( \frac{2R}{L} \right)^2 \right]^{-3/2}, \quad [4.24]$$

and the axial gradient  $g_z$  is

$$g_z = \frac{-2GM}{LR^2} \left( \frac{2R}{L} \right)^2 \left[ 1 + \left( \frac{2R}{L} \right)^2 \right]^{-3/2}, \quad [4.25]$$

from [4.21]. These gradients have the important characteristic that they change slowly as the gradiometer is moved away from the cylinder center. Careful attention needs to be given to the orientation of the gradiometer axis with respect to the cylinder axis, however.

The orientation error as well as errors due to perturbations of the cylinder discussed in sec. 4.3 can be eliminated by planning the experiment to measure  $g_x$ ,  $g_y$  and  $g_z$ . The gradiometer mount described in Chapter 1 allows the instrument to be supported in two positions which orient the gradiometer axis vertically and horizontally. Two positioning holes in the mount ensure that the axis tilts by  $90^\circ$  between these positions. Equation [4.19] says that the sum of  $g_x$ ,  $g_y$  and  $g_z$  is zero if the inverse square law is correct. This remains true in the presence of distortions of the cylinder and orientation errors.

However, we will see in sec. 4.4 that the finite size of the gradiometer puts a limit on the accuracy with which equation [4.19] can be

verified.

#### 4.2 Gradients produced by a Yukawa Potential and the Logarithmic Potential

As discussed previously several authors have proposed a violation of the inverse square law which has the form of an exponentially damped force. In this section we will consider the gradient in our cylindrical source which such a force law would produce. This force results from a potential of the form

$$\phi_y(r) = \frac{-\alpha G M e^{-\beta r}}{r} \quad [4.26]$$

The two parameters  $\alpha$  and  $\beta$  determine the magnitude and range of the potential. Since  $\phi_y$  is exponentially cut off for  $r \gg 1/\beta$ , we can only expect mass at a range of  $\beta^{-1}$  to produce significant variations from the inverse square law. The force from [4.26] is

$$\vec{a}_y(r) = \frac{-\alpha G M}{r^3} (1 + \beta r) e^{-\beta r} \vec{r} \quad [4.27]$$

Using this we can write an equation for the force on a test particle in the field of a cylindrical shell,

$$\vec{a}(r, z) = -\alpha G \sigma \int_{-L/2}^{L/2} \int_0^{2\pi} \int_{R-t}^{R+t} \frac{r' [(r-r' \cos \phi') \hat{i} + (z-z') \hat{k}]}{p^3} (1 + \beta p) e^{-\beta p} dz' d\phi' dr', \quad [4.28]$$

where

$$p = \left[ (z-z')^2 + r^2 + r'^2 - 2rr' \cos \phi' \right]^{1/2}.$$

We would like to compare the gradients  $y_r = \left. \frac{\partial (\vec{a} \cdot \hat{x})}{\partial r} \right|_{r=0}$  and  $y_z = \left. \frac{\partial (\vec{a} \cdot \hat{z})}{\partial z} \right|_{r=0}$  with the results for the Newtonian gradients, so we first calculate

$$y_r(z) = \alpha\pi G\sigma \int_{-L/2}^{L/2} \int_{R-t}^{R+t} \frac{r'}{q} \left[ \frac{3r'^2(1+\beta q)}{q^2} + (\beta^2 r'^{-2} - 2) - 2\beta q \right] e^{-\beta q} dr' dz' ,$$

[4.29]

where  $q = [(z-z')^2 + r'^2]^{1/2}$ . To lowest order in  $t/R$  we can assume that  $r'$  in the integrand takes the constant value  $R$ , then

$$y_r(z) = \frac{2t\alpha\pi G\sigma}{R} \int_{-1}^1 \left( \frac{4R^2}{L^2} \right) \frac{1}{s^3} \left[ \frac{3\eta^2}{s^2} \left( 1 + \frac{\beta R s}{\eta} \right) + (\beta^2 R^2 - 2) - \frac{2\beta R s}{\eta} \right] e^{-\frac{\beta R s}{\eta}} d\zeta' ,$$

[4.30]

where  $s = [(\zeta - \zeta')^2 + \eta^2]^{1/2}$ . Using  $M = (2t)(2\pi R)L$ ,

$$y_r(z) = \frac{\alpha G M}{2LR^2} \int_{-1}^1 \frac{\eta^2}{s^3} \left[ \frac{3\eta^2}{s^2} \left( 1 + \frac{\beta R s}{\eta} \right) + (\beta^2 R^2 - 2) - \frac{2\beta R s}{\eta} \right] e^{-\frac{\beta R s}{\eta}} d\zeta' .$$

[4.31]

Figure 4.3 shows  $y_r(0)$  calculated numerically as a function of the  $\beta R$ . When the range  $\beta^{-1}$  is comparable to the cylinder radius there is an enhancement of the gradient of almost 50 compared with what a Newtonian force law with the same coupling constant would produce. As  $\beta$  becomes small the exponential force law looks Newtonian and we recover the result of section 4.1. As  $\beta^{-1}$  becomes much less than  $R$  the force along the cylinder axis decays exponentially to zero.

Figure 4.4 shows the variation of  $y_r$  with  $z$  for three values of  $\beta R$ . As expected if  $\beta R$  is small, the signal looks approximately like that of figure 4.2, the Newtonian limit. As  $\beta R$  becomes about 1 the signal is large and independent of position as long as the gradiometer is inside of the cylinder. As the instrument leaves the cylinder the signal falls

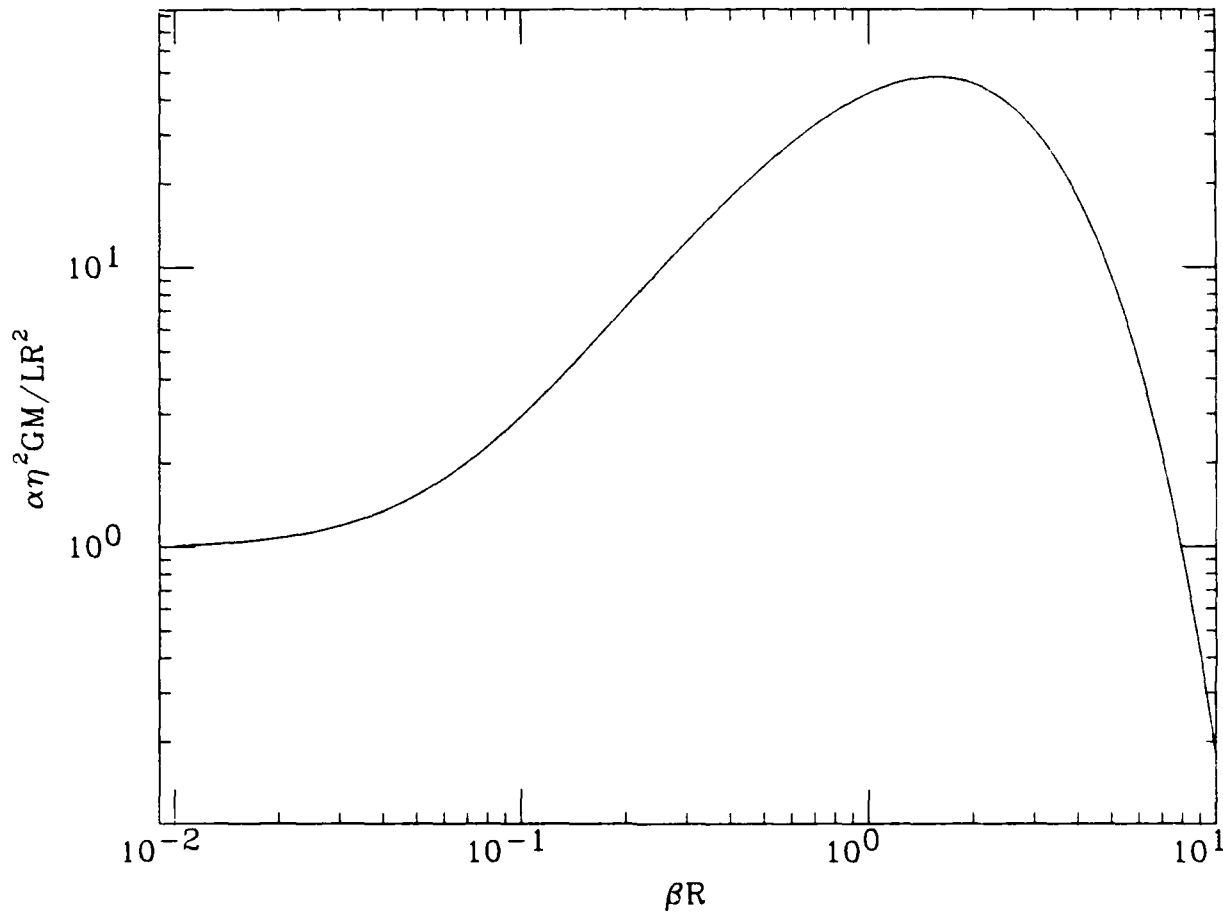


Figure 4.3  $y_r(0)$  as a Function of  $\beta R$ .

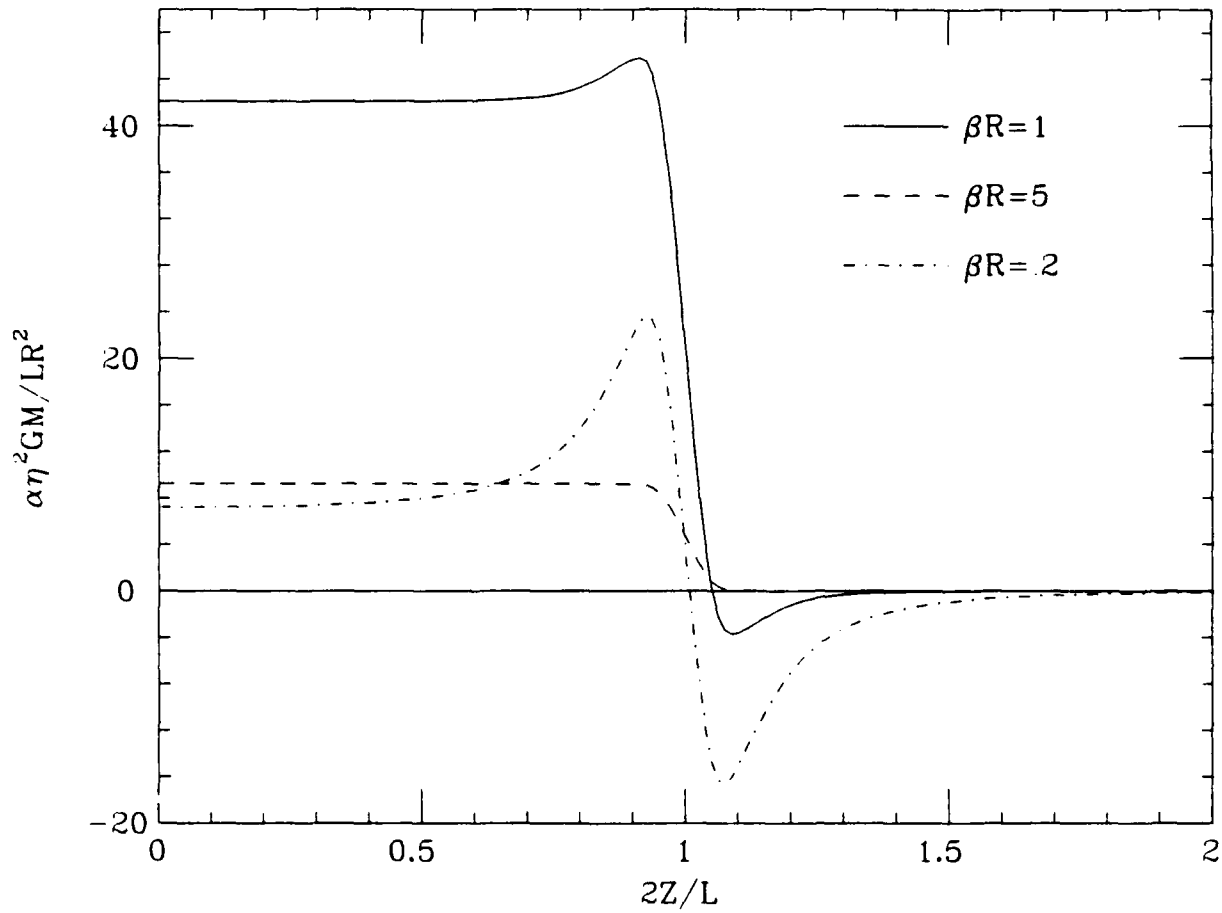


Figure 4.4  $y_r(z)$  as a function of  $z$ .

rapidly to zero due to the exponential factor. The signal for  $\beta R = 5$  is similar, but the signal inside the cylinder is much smaller, since the walls are now beyond the range of the force,  $\beta^{-1}$ .

If the gradiometer is oriented along the cylinder axis, we can calculate the gradient  $y_z(z)$  in a manner similar to that used to obtain equation [4.29]. Using [4.26],

$$a_z(r, z) = -\alpha G \sigma \int_{-L/2}^{L/2} \int_0^{2\pi} \int_{R-t}^{R+t} \frac{r'(z-z')}{p^3} (1 + \beta p) e^{-\beta p} dr' d\phi' dz'. \quad [4.32]$$

Since we are interested here in forces along the  $z$  axis we can set  $r = 0$  and do the integral over  $\phi'$ . To lowest order in  $t/R$  we can also take  $r' \approx R$  and do the integration over  $r'$ . Then

$$a_z(0, z) = \frac{-\alpha GM}{L} \int_{-L/2}^{L/2} \frac{(z-z')}{p^3} (1 + \beta p) e^{-\beta p} dz'. \quad [4.33]$$

So the gradient is

$$y_z(z) = \frac{\partial a_z(0, z)}{\partial z} = 2\alpha\eta^2 \frac{GM}{LR^2} \int_{-1}^1 \frac{e^{-\beta R s/\eta}}{2s^3} \left[ \frac{3(\zeta - \zeta')^2}{s^2} \left(1 + \frac{\beta R s}{\eta}\right) + \frac{\beta^2 R^2}{\eta^2} (\zeta - \zeta')^2 - \left(1 + \frac{\beta R s}{\eta}\right) \right] d\zeta'. \quad [4.34]$$

A numerical calculation of  $y_z(0)$  as a function of  $\beta R$  is shown in figure 4.5. As in figure 4.3 as  $\beta R$  becomes large  $y_z(0)$  goes to zero exponentially. In this case however, the fall off starts at  $\beta R \approx .1$ . This reflects the fact that  $\eta = .1$ . As soon as the range  $\beta^{-1}$  is small enough that the missing mass at the ends of the cylinder is invisible, each proof mass sees exactly the



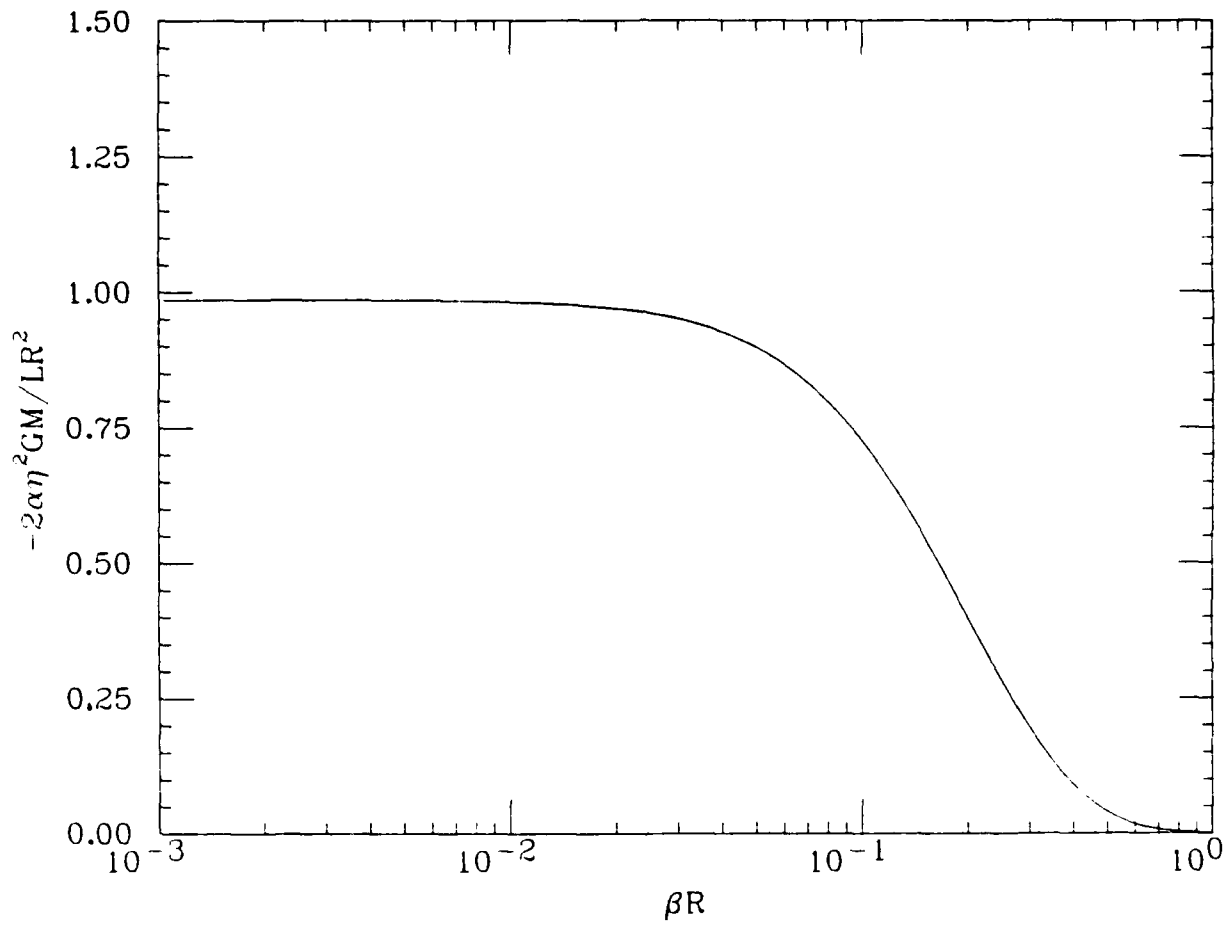


Figure 4.5  $y_2(0)$  as a function of  $\beta R$ .

same mass configuration and there is no gradient. As  $\beta^{-1}$  becomes small we again recover the Newtonian limit which from section 4.1 is  $\frac{-2\alpha\eta^2}{(1+\eta^2)^{3/2}} \frac{GM}{R^2L}$ .  $y_z(0)$  is quite different from  $y_r(0)$  in that there is no large enhancement of the gradient between these two limits. Consequently, the experiment must be done with the gradiometer horizontal to see a deviation from the inverse square law.

Unlike the Newtonian potential, the Yukawa potential does not obey Poisson's equation, and there is no simple relationship between  $y_z(0)$  and  $y_r(0)$  from all values of  $\beta$ . Suppose that a potential of the form [4.26] does exist with the optimum range for this experiment. This is the case for  $\beta R \cong 1.5$  or  $\beta^{-1} \cong 16.7$  cm. From figure 4.3

$$y_x(o) = y_y(o) = 48 \eta^2 \alpha \frac{GM}{LR^2} . \quad [4.35]$$

From figure 4.5  $y_z(0)$  is nil in this case so the sum of the gradients

$$y_x(o) + y_y(o) + y_z(o) = 96 \alpha \eta^2 \frac{GM}{LR^2} \approx \frac{\alpha GM}{LR^2} . \quad [4.36]$$

An alternative to the Yukawa potential has been proposed by D. Long [Long 1974]. It is a logarithmic potential of the form

$$V(r) = -\alpha \frac{GM}{r} \ln \left( r/r_o \right) , \quad [4.37]$$

where  $r_o$  is a range which Long takes to be 1 cm. Using this potential

$$\vec{a}(r) = -\vec{\nabla}V(r) = \alpha GM \left[ -\frac{1}{r^3} - \frac{\ln(r/r_o)}{r^3} \right] \vec{r} . \quad [4.38]$$

The first term has exactly the form of the Newtonian force scaled by a factor of  $\alpha$ . Since  $\alpha$  is presumably small, (Long gives  $\alpha = 2 \times 10^{-3}$ ) we ignore this term in what follows. As before, we would like to calculate the gradients which result in a cylinder. So we write the acceleration on a test particle in the cylinder

$$\vec{a}(r, z) = -\alpha G \sigma \int_{-L/2}^{L/2} \int_0^{2\pi} \int_{R-t}^{R+t} \frac{r' [(r-r'\cos\phi'\hat{i} + (z-z')\hat{k}) \cdot \hat{k}] \ln(p/r_0)}{p^3} dr' d\phi' dz'. \quad [4.39]$$

For comparison with figures 4.3 and 4.5, let us first calculate  $L_x(z) =$

$\left. \frac{\partial a_r}{\partial r} \right|_{r=0}$ . Taking the derivative first

$$L_r(z) = -\alpha G \sigma \int_{-L/2}^{L/2} \int_0^{2\pi} \int_{R-t}^{R+t} r' \left\{ \frac{\ln(p/r_0)}{p^3} + \frac{(r-r'\cos\phi')^2}{p^5} - \frac{3(r-r'\cos\phi')^2}{p^5} \ln(p/r_0) \right\} dr' d\phi' dz'. \quad [4.40]$$

Setting  $r = 0$  and doing the integration over  $\phi'$ ,

$$L_r(z) = -2\alpha G \sigma \pi \int_{-L/2}^{L/2} \int_{R-t}^{R+t} r' \left\{ \frac{\ln(q/r_0)}{q^3} + \frac{1}{2} \frac{r'^2}{q^5} - \frac{3}{2} \frac{r'^2 \ln(q/r_0)}{q^5} \right\} dr' dz',$$

or

$$L_r(z) = -4 \alpha G \sigma \pi R t \int_{-L/2}^{L/2} \left\{ \frac{\ln(q/r_0)}{q^3} + \frac{R^2}{2q^5} - \frac{3}{2} \frac{R^2 \ln(q/r_0)}{q^5} \right\} dz',$$

[4.41]

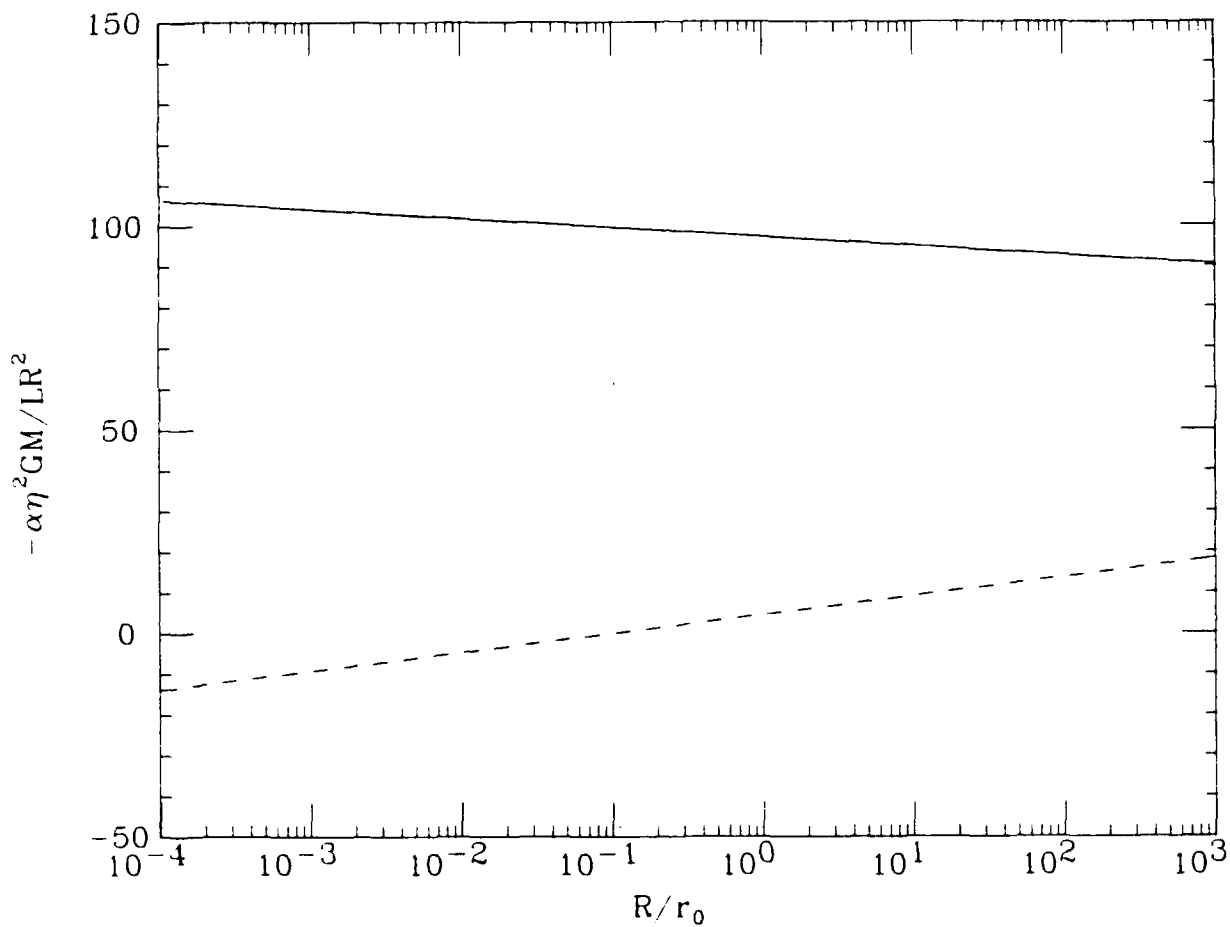


Figure 4.6  $L_2(0)$  and  $L_r(0)$  as a function of  $R/r_0$ .

to lowest order in  $R/t$ . Making the usual change of variable  $\zeta' = 2z'/L$

we find

$$L_r(z) = -\alpha\eta^2 \frac{GM}{LR^2} \int_{-1}^1 \left\{ \frac{\ln(sR/\eta r_o)}{s^3} + \frac{\eta^2}{2s^5} - 3 \frac{\eta^2}{s^5} \ln(sR/\eta r_o) \right\} d\zeta' \quad [4.42]$$

Similarly we can calculate  $L_z(z)$  to be

$$L_z(z) = -\alpha\eta^2 \frac{GM}{LR^2} \int_{-1}^1 \left[ \ln(sR/\eta r_o) + (\zeta - \zeta')^2/s^2 \right] d\zeta'. \quad [4.43]$$

A numerical calculation of  $L_r(0)$  and  $L_z(0)$  is shown in figure 4.6 for a wide range of  $R/r_o$ . The solid curve is  $L_r(0)$ , and the dashed curve is  $L_z(0)$ . As for the Yukawa potential,  $L_r(0)$  is much greater than  $g_r(0)$  if  $\alpha \approx 1$ . And again  $L_z(0) \ll L_r(0)$ . In this case however, there is no Newtonian limit and  $L_r(0)$  is only very weakly dependent on the choice of range  $r_o$ . Using Long's choice of  $\alpha$  and  $r_o$  [Long 1976] we find that  $L_r(0)/g_r(0) = -.185$ , a very large effect. This result has effectively been ruled out by the experiment of Newman [Spero 1980]. However, Long has recently suggested that a logarithmic modification of the inverse square law might not be observable inside of a cylinder [Long 1980b].

#### 4.3 Gradient Errors due to Cylinder Perturbations

Among the principal sources of error in a measurement of the cylinder's gravity gradients are perturbations of the cylinder's density and shape. In this section we will model these perturbations in order to identify initial tolerances and develop strategies for making the measurement in an imperfect cylinder.

Let us suppose that the deviations of the cylinder from perfect shape and homogeneity can be represented by writing the cylinder density as

$$\sigma(\zeta, \phi) = \sum_{i=0}^{\infty} \sum_{j=0}^{\infty} P_i(\zeta) \left[ a_{ij} \sin j\phi + b_{ij} \cos j\phi \right], \quad [4.44]$$

where  $b_{0,0} = 1$  and  $\sigma$  is the mean density of the cylinder. The  $P_i$ 's are the Legendre polynomials defined as  $P_0 = 1$  and

$$P_i(\zeta) = \frac{1}{2^i i!} \frac{d^i}{d\zeta^i} (\zeta^2 - 1)^i. \quad [4.45]$$

It is shown in many standard texts on linear analysis that the Legendre polynomials form an orthogonal basis for the set of piecewise continuous functions on the interval  $-1$  to  $1$ . See for example [Kreider 1966]. They have the additional property that  $P_i$  is even if  $i$  is even and odd if  $i$  is odd.

Equation [4.44] ignores radial variations in density since such variations change only in the higher order terms in  $t/R$ , and these terms are very small as is shown by [4.12]. Now using [4.13] and substituting the new expression for  $\sigma$ , we have

$$g_r(z) = \frac{-\eta^2 GM}{2\pi\sigma RL^2} \int_{-1}^1 \int_0^{2\pi} \sigma(\zeta', \phi') \left\{ \frac{1}{\left[ (\zeta - \zeta')^2 + \eta^2 \right]^{3/2}} - \frac{3\eta^2 (1 + \cos 2\phi')}{2 \left[ (\zeta - \zeta')^2 + \eta^2 \right]^{5/2}} \right\} d\phi' d\zeta', \quad [4.46]$$

and substituting [4.44]

$$g_r(z) = \frac{-\eta^2 GM}{2\pi LR^2} \int_{-1}^1 \sum_{i=0}^{\infty} P_i(\zeta') \int_0^{2\pi} \sum_{j=0}^{\infty} (a_{ij} \sin j\phi + b_{ij} \cos j\phi) \left[ \frac{1}{\left[ (\zeta - \zeta')^2 + \eta^2 \right]^{3/2}} - \frac{3\eta^2 (1 + \cos 2\phi')}{2 \left[ (\zeta - \zeta')^2 + \eta^2 \right]^{5/2}} \right] d\phi' d\zeta'. \quad [4.47]$$

Since we are primarily interested in gradients at the center of the cylinder we will take  $z = 0$  and define the error terms

$$E_{ij} = -\eta^2 \frac{GM}{LR^2} \int_{-1}^1 P_i(\zeta') \int_0^{2\pi} (a_{ij} \sin j\phi + b_{ij} \cos j\phi) \left[ \frac{1}{[\zeta'^2 + \eta^2]^{3/2}} - \frac{3\eta^2 (1 + \cos 2\phi')}{2[\zeta'^2 + \eta^2]^{5/2}} \right] d\phi' d\zeta' \quad [4.48]$$

Since the  $\sin(j\phi')$  and  $\cos(j\phi')$  functions are a mutually orthogonal set, the only nonzero  $E_{ij}$ 's are those with  $j=0$  and  $j=2$ . Also, since the function of  $\zeta'$  in brackets is even, and the  $P_i$  is odd if  $i$  is odd, only  $E_{ij}$ 's with even  $i$  are nonzero. Using these simplifications

$$E_{2i0} = -\eta^2 b_{2i0} \frac{GM}{LR^2} \int_{-1}^1 P_{2i}(\zeta') \left\{ \frac{1}{[\zeta'^2 + \eta^2]^{3/2}} - \frac{3\eta^2}{2[\zeta'^2 + \eta^2]^{5/2}} \right\} a_{\zeta'} \quad [4.49]$$

and

$$E_{2i2} = \eta^2 b_{2i2} \frac{GM}{LR^2} \int_{-1}^1 P_{2i}(\zeta') \left\{ \frac{3\eta^2}{4[\zeta'^2 + \eta^2]^{5/2}} \right\} d\zeta' \quad [4.50]$$

are the only nonzero  $E_{ij}$ 's.

First we calculate some of the  $E_{2i0}$ 's.  $P_2(x) = \frac{1}{2}(3x^2 - 1)$  so

$$E_{20} = \frac{-\eta^2 b_{20} GM}{4LR^2} \int_{-1}^1 \frac{(3\zeta'^2 - 1)(2\zeta'^2 - \eta^2) d\zeta'}{[\zeta'^2 + \eta^2]^{5/2}} \quad [4.51]$$

All of these integrals can be evaluated explicitly giving

$$E_{20} = \frac{-\eta^2 b_{20}^{GM}}{2LR^2} \left\{ 6 \left[ \ln(1 + \sqrt{1+\eta^2}) - \ln \eta - \frac{1}{3(1+\eta^2)^{3/2}} \right. \right. \\ \left. \left. - \frac{1}{(1+\eta^2)^{1/2}} \right] - (2+3\eta^2) \left[ \frac{1}{3\eta^2(1+\eta^2)^{3/2}} \right] + \eta^2 \left[ \frac{1}{(1+\eta^2)^{1/2}} - \frac{1}{3(1+\eta^2)^{3/2}} \right] \right\}.$$

Putting in the value  $\eta = .1$  gives

$$E_{20} = -5.02 \eta^2 \frac{GMb_{20}}{LR^2}. \quad [4.53]$$

A similar calculation gives

$$E_{40} = 7.83 \eta^2 \frac{GMb_{40}}{LR^2}. \quad [4.54]$$

Next let us calculate some of the error terms of the form  $E_{2i2}$ .

Consider  $E_{22}$ , from [4.50]

$$E_{02} = \frac{3\eta^4 b_{02}^{GM}}{4LR^2} \int_{-1}^1 \frac{1}{[\zeta^2 + \eta^2]^{5/2}} d\zeta'.$$

So

$$E_{02} = \frac{3}{2} \eta^4 b_{02} \frac{GM}{LR^2} \frac{1}{\eta^4} \left\{ \frac{1}{[1+\eta^2]^{1/2}} - \frac{1}{3} \frac{1}{[1+\eta^2]^{3/2}} \right\} \\ = b_{02} \frac{GM}{LR^2}, \quad [4.55]$$

to lowest order in  $\eta^2$ . In general the lowest order contribution to  $E_{2i2}$  in  $\eta^2$  is given by

$$E_{2i2} = \eta^2 b_{2i2} \frac{GM}{LR^2} \int_{-1}^1 P_{2i}^{(0)} \frac{3}{4} \left\{ \frac{\eta^2}{[\zeta^2 + \eta^2]^{5/2}} \right\} d\zeta'. \quad [4.56]$$



Cylinder Error Coefficients

$2n$	$E_{2n0} [n^2 b_{20}^2 \text{ GM/LR}^2]$ ,	$E_{2n2} [b_{2n2}^2 \text{ GM/LR}^2]$
2	- 5.02	- .492
4	7.83	.358
6	- 9.53	- .284
8	10.4	.234
10	-10.6	- .196
12	10.5	.167
14	-10.0	- .141
16	9.42	

Table 4.1

$$P_{2n}(0) = \frac{(-1)^{3n} (2n!)}{2^{2n} (n!)^2} , \quad [4.57]$$

so

$$E_{2n2} = \frac{(-1)^{3n} (2n!)}{2^{2n} (n!)^2} \frac{GM}{LR^2} b_{2n2} , \quad [4.58]$$

to lowest order in  $\eta^2$ . The first eight nonzero  $E_{2n2}$  and  $E_{2n0}$  are listed in Table 4.1.

With these results we can examine the effects of various errors. The error coefficients of the form  $E_{2n2}$  are considerably larger than the  $E_{2n0}$ , but as the gradiometer is rotated in the center plane of the cylinder the gradients produced by the  $E_{2n2}$  errors have a  $\cos 2\phi$  dependence. Consequently if one averages two gradient measurements made with the cylinder rotated by  $90^\circ$  with respect to the gradiometer axis the result is zero. Actually this result is apparent from equation [4.19]. If the gradiometer is oriented along the  $z$ -axis (the cylinder symmetry axis), a mass distribution with  $\cos 2\phi$  dependence cannot produce any gradient since there is no net mass, and all the mass is equidistant from the gradiometer. So from [4.19] any two gradients measured along orthogonal directions in a plane perpendicular to the  $z$ -axis must be equal and opposite. This provides a simple way of eliminating all errors of this type. We simply measure horizontal gradients along the  $x$  and  $y$  directions and average them. Any difference in these measurements would indicate the presence of a  $\phi$  dependence in the cylinder mass or density.

Similarly, any of the  $E_{2n0}$  errors can be identified by comparing the gradient along the  $z$  axis with the sum of the  $x$  and  $y$  gradients. In short, if all three gradients are measured, [4.19] insures that their sum is zero

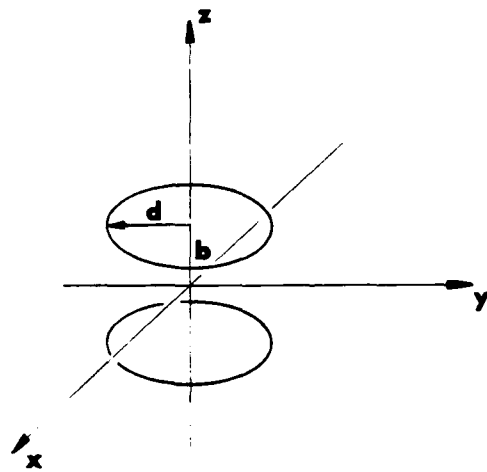
regardless of flaws in the cylinder. The cylindrical geometry is still crucial, however, because it relieves the experimenter from the need to precisely position the gradiometer inside of the cylinder.

#### 4.4 Finite Size Effects

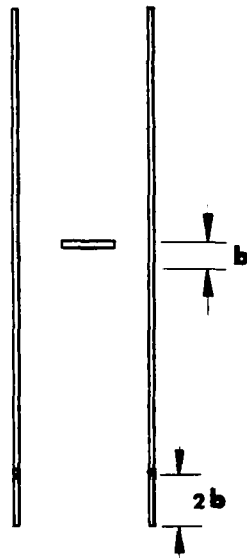
Since the preceding calculations give the gradients at points, they are strictly valid only for infinitesimally small gradiometers. In this section we will consider the errors which result from measuring gradients with a finite size instrument. Basically, we need to know how [4.19] is modified by the finite size of the gradiometer.

An indication that finite size effects are small was given in section 4.1. For example, we found that the radial gradient changes by less than .1% if the gradiometer is moved along the z-axis 4.6 cm from the cylinder center. So if the gradiometer proof masses have a diameter less than 4.6 cm we would guess that the error from its finite size will be less than .1%. The actual diameter of the proof masses is 4.3 cm.

Suppose the gradiometer is oriented along the z-axis at the center of the cylinder as in 4.7a. To calculate the force on the upper proof mass we can imagine splitting the cylinder into two parts as in 4.7b. Since the upper proof mass is at the center of the upper cylinder piece, symmetry implies that only the lower part of the cylinder applies a net force on this part of the gradiometer. Since the gradiometer is far away compared to the length and thickness of this piece we will calculate its gravitational field in the vicinity of the gradiometer using the approximation that it is a very thin ring of material with a mass per radian of  $bM/L\pi$ . Then the z-component of acceleration in the center of the upper cylinder is



(a)



(b)

Figure 4.7 (a) Gradiometer with its Axis Vertical  
 (b) Cylinder Split into Two Parts

$$a_z(r) = \frac{-GMb}{2\pi} \int_0^{2\pi} \frac{d\phi}{\left[ (L/2)^2 + r^2 + R^2 - 2rR\cos\phi \right]^{3/2}}. \quad [4.59]$$

Since the gradiometer is small compared with R we expand the denominator in

$\zeta = r/R$ , so

$$a_z(r) = \frac{-GMb}{2\pi R^2} \int_0^{2\pi} \frac{d\phi}{\left[ (L/2R)^2 + 1 + \zeta^2 \right]^{3/2}} \left[ 1 + \frac{3\zeta\cos\phi}{\left[ 1 + \zeta^2 + 1/\eta^2 \right]} + \frac{15\zeta^2\cos^2\phi}{2\left[ 1 + \zeta^2 + 1/\eta^2 \right]^2} + \dots \right]. \quad [4.60]$$

Integration over  $\phi$  gives

$$a_z(r) = \frac{-GMb}{R^3 \left[ 1 + \zeta^2 + 1/\eta^2 \right]^{3/2}} \left\{ 1 + \frac{15\zeta^2}{4 \left[ 1 + \zeta^2 + 1/\eta^2 \right]^2} + \dots \right\}. \quad [4.61]$$

To evaluate the lowest order finite size correction we integrate this acceleration over a disk of diameter d with mass per unit area s, so

$$F_z = \frac{-GMbs}{R} \int_0^{d/R} \int_0^{2\pi} \left\{ \frac{1}{\left[ 1 + \zeta^2 + 1/\eta^2 \right]^{3/2}} + \frac{15\zeta^2}{2 \left[ 1 + \zeta^2 + 1/\eta^2 \right]^2} \right\} \zeta d\zeta d\phi. \quad [4.62]$$

After carrying out the integration and expanding the result in  $\eta = 2R/L$  one finds that

$$F_z = \frac{-2GMbm}{LR^2} \left\{ \frac{\eta^2}{(1+\eta^2)^{3/2}} - \frac{3\eta^4(d/R)^2}{2 \left[ 1 + \eta^2 \right]^{5/2}} + \sigma(\eta^6) \right\}, \quad [4.63]$$

where m is the mass of the disk. Since the gradiometer is symmetric about the origin, the result for the lower disk is  $-F_z$  and the gradient  $y_z$  is given by

$$g_z = \frac{2F_z}{26m} = \frac{-2GM}{LR^2} \frac{\eta^2}{(1+\eta^2)^{3/2}} \left\{ 1 - \frac{3\eta^2(d/z)^2}{2[1+\eta^2]} + \sigma(\eta^4) \right\} . \quad [4.64]$$

The leading term is exactly the result of section 4.1, and the lowest order correction is

$$g'_z = \frac{3GM}{LR^2} \frac{\eta^4}{[1+\eta^2]^{5/2}} \left( \frac{d}{R} \right)^2 . \quad [4.65]$$

The ratio

$$g'_z/g_z = -\frac{3}{2} \eta^2 \left( \frac{d}{R} \right)^2 = -4.44 \times 10^{-4} \quad [4.66]$$

to lowest order in  $\eta^2$ , for a proof mass with a radius of 4.3 cm. Fortunately this is quite a small correction and does not interfere with a .1% measurement of the cylinder gradients.

Next we must consider the finite size corrections when the gradiometer axis is perpendicular to the cylinder axis. Looking back at equation [4.5] if we leave  $\zeta \neq 0$  and work out  $a_r(r,z)$  we find that the first two terms of equation [4.12] become

$$a_r(r,z) = \frac{1}{2} \frac{GM}{LR} \eta^2 \frac{r}{R} \left[ \frac{1}{(1+\frac{2z}{L})^2} + \frac{1}{(1-\frac{2z}{L})^2} \right] \left\{ 1 - \frac{3}{2} \eta^2 \left[ \frac{1}{(1+\frac{2z}{L})^4} - \frac{1}{(1-\frac{2z}{L})^4} \right] \left( 1 + \left( \frac{r}{R} \right)^2 + \frac{r^2}{2R^2} \right) + \sigma(\eta^4) \right\} . \quad [4.67]$$

From this we can see that the lowest order finite size correction in  $\eta^2$  and  $(2d/L)^2$  comes from a term of the form

$$a'_r(r,z) = \frac{3GM}{LR^2} \eta^2 r \left( \frac{2z}{L} \right)^2 \quad [4.68]$$

To calculate the gradient correction we need to integrate  $a'_r$  over a disk whose axis is along the x axis and whose center is a distance b from the origin and whose mass per unit area is again s. Then

$$F_x = \frac{3GM}{LR^2} \eta^2 bs \int_{-d}^d \left(\frac{2z}{L}\right)^2 \sqrt{d^2 - z^2} dz . \quad [4.69]$$

This gives a gradient correction of

$$g'_x = \frac{3}{2} \frac{GM}{LR^2} \eta^2 \left(\frac{2d}{L}\right)^2 = \frac{3}{2} \frac{GM}{LR^2} \eta^4 \left(\frac{d}{R}\right)^2 . \quad [4.70]$$

This is just half the value of  $g'_z$  to lowest order is  $\eta^2$ . Since  $g_z/g_x = -2$ ,

$$\frac{g'_x}{g_x} = \frac{g'_y}{g_y} = 4.44 \times 10^{-4} . \quad [4.71]$$

From this we can see that [4.19] now does not hold exactly. Summing the finite errors we have

$$g'_x + g'_y + g'_z = 6 \frac{GM}{LR^2} \eta^4 \left(\frac{d}{R}\right)^2 \quad [4.72]$$

This effect puts a lower limit on the value of  $\alpha$  which can be detected in equation [4.36]. Taking the ratio we find that the minimum detectable  $\alpha$  is given roughly by

$$\alpha_{\min} = 6\eta^4 \left(\frac{d}{R}\right)^2 = 1.8 \times 10^{-5} . \quad [4.73]$$

It is interesting to consider briefly the finite size effect that would be produced by some flaw in the cylinder. Suppose for instance, that a cubic centimeter of cylinder material is missing in the wall about one meter from the geometrical center. It is easy to calculate that to the lowest order in  $b$ , the baseline, this flaw produces a  $\nabla^2\phi$  of  $3 \times 10^{-6} E$ , an effect far too small to observe in this experiment.

#### 4.5 Experimental Procedure

Since the d.c. output of the gradiometer is determined by the surroundings, the signal from the cylindrical source must be modulated to distinguish it from the rest of the gradients due to other objects. The cylindrical geometry is convenient for this purpose since the cylinder can be raised and lowered over the cryostat containing the gradiometer.

Figure 4.8 is a rough sketch of the apparatus we will use for moving the cylinder. In order to support the dewar near floor level we will excavate a hole ten to twelve feet deep in the floor of end station II at the high energy physics laboratory. A pedestal will be mounted in the center of the hole to support the dewar. The cylinder will be raised and lowered with a motorized hoist. In the low position the gradiometer will be at the center of the cylinder, and in the high position the gradiometer will be about 10 meters from the center of the cylinder. To measure the central gradients, the cylinder should be removed to infinity leaving everything else fixed. Since the roof of the end station prevents this, a correction has to be made for the gradient produced by the cylinder in the high position. Looking back at [4.17] we can calculate that the cylinder produces a gradient on the high position which is 3.5% of the gradient in the low position if it is moved two cylinder lengths away ( $2z/L = 4$ ). The signal changes sign as the cylinder is moved away, so the difference between the



gradient measured with the cylinder down and the cylinder up has to be reduced by 3.5% to obtain the correct central gradient. This procedure works for measuring the horizontal or vertical gradient, and it only needs to be carried out with an accuracy of a few percent to obtain the central gradient to an accuracy of .1%.

By raising and lowering the cylinder, the signal frequency can be moved away from d.c. and averaging can be used to obtain a very narrow bandwidth. With the current noise level of  $100E/\sqrt{\text{Hz}}$ , a bandwidth of  $10^{-8}$  Hz is necessary to obtain the desired noise level of  $10^{-2} E$ , so some reduction in the noise level is still necessary to make this procedure practical.

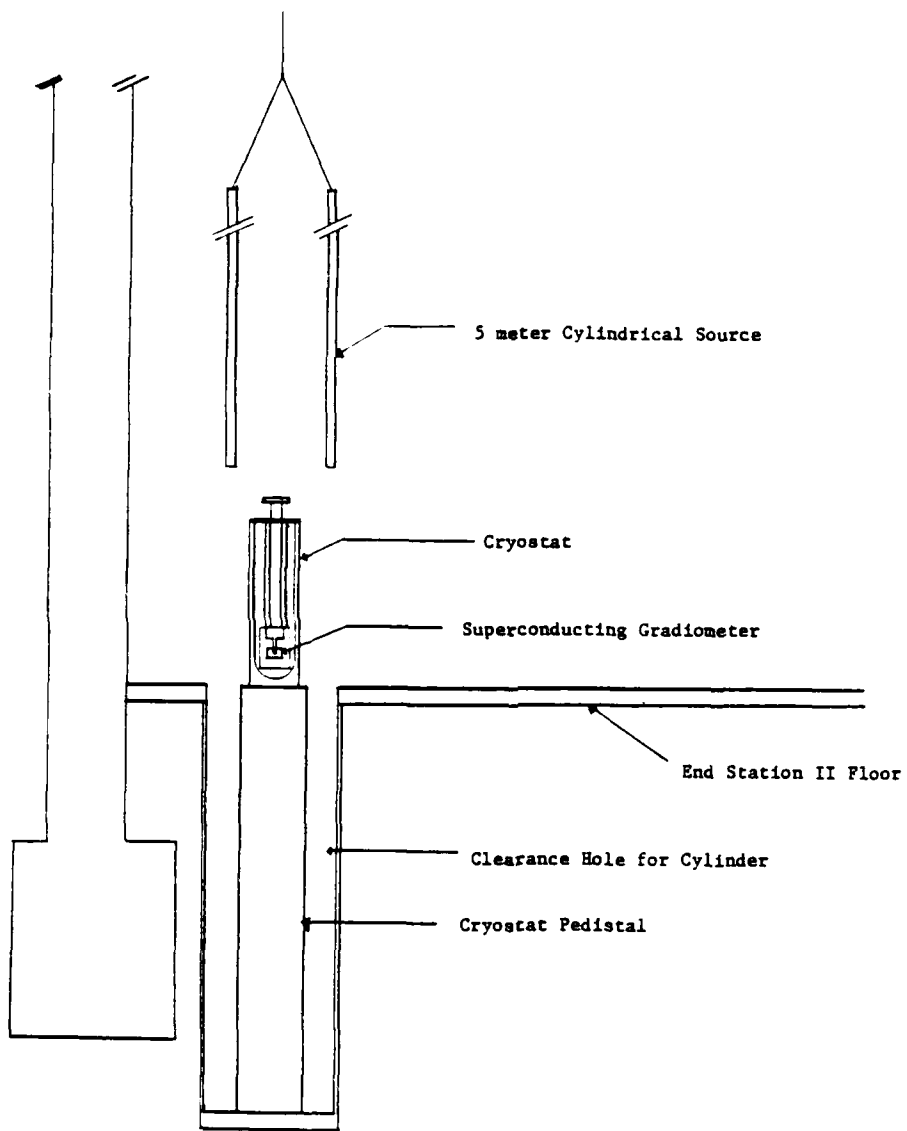


Figure 4.8 Cylinder Moving Apparatus

## CHAPTER 5

### Conclusions

We have developed a superconducting instrument for the measurement of force gradients. This instrument uses a variety of properties of superconductors to achieve very high displacement sensitivity. The measurements described in Chapter 2 demonstrate that the performance of the instrument is very close to the expected behavior, although the problem of excess low frequency noise remains to be solved. This problem is not a consequence of the techniques used in building the instrument, but rather of the desire to have an instrument which can measure vertical and horizontal gradients. An instrument could be designed for horizontal use only with higher compliance along the sensitive axis. This would reduce the gradient equivalence of a temperature change. However, as discussed in Chapter 2, there are steps which can be taken to improve this instrument. The most attractive of these steps would be to operate the instrument in a helium bath cooled below the  $\lambda$  point.

This instrument will be incorporated into an experiment to check the inverse square law of gravitation. The possibility of an inverse square law violation is briefly discussed in Chapter 3. In spite of considerable effort by many groups to verify the inverse square law, the possibility of a large violation with a range between 100 m and  $10^3$  km or less than 1 cm remains. Our experiment is optimized to detect a small violation with a range near 17 cm, but the use of superconducting technology for sensitive detectors may well contribute to a variety of experiments.

#### REFERENCES

- Anderson 1962 P.W. Anderson, *Phys. Rev. Lett.* 9, 309 (1962).
- Anderson 1964 P.W. Anderson and Y.B. Kim, *Rev. Mod. Phys.* 36, 39 (1964).
- Beams 1971 J.W. Beams, *Physics Today*, May 1971, p. 34.
- Bell 1977 Bell Aerospace Report, No. 6324-927001, 1977.
- Boys 1895 C.V. Boys, *Philos. Trans. R. Soc. Lond. A*, part 1, 1(1895).
- Braun 1896 K. Braun, *Denkschriften A. Akademie der Wissenschaften Wien, Mathematisch-Naturwissenschaftliche U.* 64, 187 (1896).
- Buck 1965 R.C. Buck, *Advanced Calculus*, McGraw Hill Book Co., New York (1965).
- Corruccini 1961 R.C. Corruccini and J.J. Gniewek, *Thermal Expansion of Technical Solids at Low Temperatures*, NBS Monograph 29, Washington, D.C. (1961).
- Esposito 1976 P.B. Esposito, J.D. Anderson and A.T.Y. Ng, *Proceedings of the 19th Primary Meeting of COSPAR*, Philadelphia (June 1976).
- Forward 1973 R.L. Forward, "Moving Base Rotating Gravity Gradiometer Development," Hughes Research Lab Report No. 461, 1973.
- Fujii 1971 V. Fujii, *Nature (London) Phys. Sci.* 234, 5 (1971).
- Goldstein 1950 H. Goldstein, *Classical Mechanics*, Addison-Wesley Pub. Corp., Reading, Mass., 1950.
- Heyl 1930 P. Heyl, *J. Res. Natl. Bur. Stand. (U.S.)* 5, 1234 (1930).
- Heyl 1942 P. Heyl and P. Chrzanowski, *J. Res. Natl. Bur. Stand. (U.S.)* 29, 1 (1942).
- Hirakawa 1980 H. Hirakawa, K. Tsubono, and K. Oide, *Nature* 283, No. 5743, 184 (1980).
- Howard 1974 H.T. Howard, G.L. Tyler, G. Fjeldbo, A.J. Kliore, G.S. Lecy, D.L. Bruun, R. Dickinson, R.E. Edelson, W.L. Martin, R.B. Postal, B. Seidel, T.T. Sesplaukis, D.L. Shirley, C.J. Stelzried, D.N. Sweetman, A.I. Zugielbaum, P.B. Esposito, J.D. Anderson, I.I. Shapiro, and R.D. Reasenber, *Science* 183, 1247 (1974).

- Karagioz 1976 O.V. Karagioz, V.P. Izmaglow, N.I. Agafonev, E.G. Kocherym, and Yv. A. Taronov, Phys. of the Solid Earth, 12, No. 5, 351 (1976).
- Kim 1962 Y.B. Kim, C.F. Hempstead, and A.R. Strand, Phys. Rev. Lett. 9, 306 (1962).
- Klinger 1974 D.L. Klinger, thesis, unpublished, Stanford University, Stanford, CA (1974).
- Kreider 1966 D.C. Kreider, R.G. Kuller, D.R. Ostberg, and F.W. Perkins, An Introduction to Linear Analysis, Addison-Wesley Pub. Co., Reading (1966).
- Landau 1959 L.D. Landau and E.M. Lifshitz, Theory of Elasticity, Pergamon Press, New York (1959).
- Laubscher 1971 R.E. Laubscher, Astron. and Astrophys. 13, 426 (1971).
- Long 1974 D.R. Long, Phys. Rev. D 9, 850 (1974).
- Long 1976 D.R. Long, Nature 260, 417 (1976).
- Long 1979 D.R. Long, private communication.
- Long 1980a D.R. Long, Il Nuovo Cimento 55B, 252 (1980).
- Long 1980b D.R. Long, to be published.
- Marion 1970 J.B. Marion, Classical Dynamics of Particles and Systems, Academic Press, New York (1970).
- Mikkelson k977 D.R. Mikkelson and M.J. Newman, Phys. Rev. D 16, 191 (1977).
- O'Hanlon 1972 J. O'Hanlon, Phys. Rev. Lett. 29, 137 (1972).
- Panov 1979 V.I. Panov and V.N. Frantov, Zh. Eksp. Tear. Fiz. 77, 1701 (1979).
- Paik 1979 H.J. Paik, E.R. Mapoles, and K.Y. Wang, Superconducting Gravity Gradiometers, Future Trends in Superconducting Electronics, (Charlottesville, 1978) p. 166.
- Paik 1979 H.J. Paik, Phys. Rev. D 19, 2320 (1979).
- Poynting 1891 J.H. Poynting, Philos. Trans. R. Soc. Lond. A 182, 565 (1891).
- Richarz 1898 F. Richarz and O. Kriger-Menzel, Nature 55, 296 (1898).

- Rose 1969 R.D. Rose, H.M. Parker, R.A. Lowry, A.R. Kuhlthau,  
and J.W. Beams, Phys. Rev. Lett. 23, 655 (1969).
- Shapiro 1971 I.I. Shapiro, W.B. Smith, M.E. Ash, and S. Herrick,  
Astron. J. 76, 588 (1971).
- Shapiro 1973 I.I. Shapiro and R.D. Reasonberg, JPL Tech. Report  
32-1550, V. 4, 453 (JPL, Pasadena, CA, 1973),  
unpublished.
- Shapiro 1976 I.I. Shapiro, C.B. Counselman III, and R.W. King,  
Phys. Rev. Lett. 36, 555 (1976).
- Taylor 1976 J.H. Taylor, R.A. Hulse, L.A. Fowler, G.E. Gullahorn,  
and J.M. Rankin, Astrophys. J. Lett. 206, L53 (1976).
- Tinkham 1975 M. Tinkham, Intro. to Superconductivity, McGraw-Hill  
Book Co., New York (1975).
- Trageser 1975 M.B. Targeser, "Feasibility Model Gravity Gradiometer  
Test Results," Report No. P-179, C.S. Draper Lab, Cam-  
bridge, Mass., 1975.
- Wagoner 1970 R.V. Wagoner, Phys. Rev. D 1, 3209 (1970).
- Wang 1979 K.Y. Wang, thesis, unpublished, Stanford University,  
Stanford, CA (1979).

**END**

**FILMED**

**3-86**

**DTIC**